UNIVERSITÄT
DUISBURG
ESSEN

Offen im Denken

Electrocaloric Effect & Electrical Energy Storage in Ferroelectric Relaxor Polymers & their Nanocomposites

Faculty of Engineering

University of Duisburg-Essen

Institute for Materials Science

for the academic degree of

Doktor-Ingenieur (Dr.-Ing.)

Dissertation by

Yusra Hambal, M. Sc. (Hons.)

Referees

Prof. Dr. rer. nat. habil. Doru C. Lupascu

Prof. Dr.-Ing. Annika Raatz

Date of Examination: May 23rd, 2022

DOI: 10.17185/duepublico/77258
URN: urn:nbn:de:hbz:465-20230404-074922-5

Acknowledgement

Pursuing this PhD has been a real delightful experience for me, which would not have been possible without the valuable guidance and support of many *people*.

First and foremost, I would like to thank Prof. Dr. Doru C. Lupascu for trusting my abilities and giving me the opportunity to be a part of his group. I am deeply grateful for his valuable support, guidance, and time for the fruitful discussions. I am highly grateful to PD Dr. Vladimir V. Shvartsman for his constant support, guidance, patience, and time for in-depth and insightful discussions. I am indebted to Karl-Heinz Menze for his immense and persistent technical support with the quasi-adiabatic calorimeter, and for helping me to understand the technical details. They played their respective roles very well to broaden my horizon, and I learned many new things from them.

I gratefully acknowledge the valuable input that I received from Prof. Dr. Qiming Zhang, Penn State University, USA. I would like to thank Prof. Dr. Annika Raatz for being the second examiner. I am grateful to Prof. Dr. Natalie Stranghöner, and Prof. Dr. Jörg Schröder for being part of the examination committee.

I am truly grateful to Stefan Nawrath, Merlin Schmuck, Karl-Heinz Menze, and Andreas Schmidt for the smooth technical assistance and availability of the resources, especially during the pandemic. I am thankful to Prof. Epple for providing his SEM facility and to Merlin Schmuck and Tobias Bochmann for the SEM images. Many thanks go to Daniil Lewin for his expertise in polarization data extraction.

I am sincerely thankful to Xin Chen for his warm and friendly support during my visit to Penn State University. It was my utmost pleasure to supervise Chieng Huo Huat and PD Dr. Ivo Michiels. I had really enjoyed working with them, and acknowledge their respective contributions to this work.

I am grateful to Gustave with whom I shared my office before the pandemic, for being a quiet person, enabling me to work without interruptions. I enjoyed the time that I spent with Sobhan during my last days. The witty remarks of Dr. Keck, Merlin and Felix were always a source of joy to me during all these years. I value the support that I received from the ferro group.

I would like to thank all my colleagues for introducing me to diverse cultures and interests. I will cherish the time that we spent together in La Clusaz.

Last but not the least, I highly acknowledge the immense support that I received from Marc and deeply appreciate our insightful discussions. I would like to thank my families, especially my sisters, and friends for their love and support.

Abstract

The demand for effective cooling and energy storage technologies is growing continuously. The climatic changes, miniaturization, and digitalization have redefined the technological development in the cooling and energy storage industries. The global focus is on the environmental-friendly, efficient, sustainable, and scalable cooling technologies. Owing to all these factors, green alternatives to the traditional air-conditioning and refrigeration are gaining momentum. One of such green alternatives is the electrocaloric effect (ECE). The electrocaloric effect is observed in dielectric materials as they undergo an adiabatic temperature change or an isothermal entropy change under an externally applied/removed electric field. Dielectric materials are capable to store the electrical energy as well. Therefore, they are particularly interesting for the new cooling and energy storage technologies.

In this work, a ferroelectric relaxor polymer, namely, Poly(vinylidene fluoride – trifluoroethylene – chlorofluoroethylene) (P(VDF–TrFE–CFE) is investigated for the electrocaloric effect through the direct and the indirect methods. The electrical energy storage properties of different compositions of P(VDF–TrFE–CFE) and their nanocomposites with inorganic 0D nanofillers are studied.

Initially, the relaxor properties in six different compositions of P(VDF–TrFE–CFE) are studied. Out of these six compositions, the three compositions, 51.3/48.7/6.2, 59.8/40.2/7.3, and 70/30/8.1, are analyzed for the first time. The field induced phase transition results in a double hysteresis loop in a few compositions. Through the direct electrocaloric measurements, it is observed that the electric field induced phase transition results in a higher electrocaloric temperature change. The indirect electrocaloric measurements are conducted with and without compensating the leakage current. It is shown that the indirect method can lead to erroneous results due to the leakage current. The results obtained through the indirect measurements conducted with the leakage current compensation are comparable to the direct measurements. The electrical energy storage properties of the neat terpolymers and their nanocomposites are compared. It is observed that the stored and discharged energy densities of the nanocomposites are superior to the neat terpolymers.

Keywords: Electrocaloric effect, direct method, indirect method, ferroelectric polymer, relaxor, double hysteresis loop, electrical energy storage, nanocomposite

Kurzfassung

Der Bedarf an effektiven Kühl- und Energiespeicherverfahren steigt kontinuierlich an. Die klimatischen Veränderungen, die Miniaturisierung und die Digitalisierung haben einen Wandel in der Entwicklung von Kühl- und Energiespeichertechnologien hervorgerufen. Der globale Fokus liegt auf umweltfreundlichen, effizienten, nachhaltigen und skalierbaren Kühltechnologien. Aufgrund dieser Faktoren gewinnen die umweltfreundlichen Alternativen zu den herkömmlichen Klimaanlagen und Kühlsystemen an Bedeutung. Eine dieser grünen Alternativen ist der elektrokalorische Effekt (ECE). Dieser wird bei dielektrischen Materialien beobachtet, wenn sie unter einem von außen angelegten/entfernten elektrischen Feld eine adiabatische Temperaturänderung oder eine isotherme Entropieänderung erfahren. Dielektrische Materialien können auch elektrische Energie speichern und sind daher für neue Kühl- und Energiespeichertechnologien besonders interessant.

In dieser Arbeit wird ein ferroelektrisches Relaxor-Polymer, nämlich Poly(vinylidenfluorid-Trifluorethylen-Chlorfluorethylen) (P(VDF-TrFE-CFE)), mit direkten und indirekten Methoden auf den elektrokalorischen Effekt untersucht. Darüber hinaus werden die elektrischen Energiespeichereigenschaften verschiedener Zusammensetzungen von P(VDF-TrFE-CFE) und dessen Nanokomposite mit anorganischem 0D-Nanofüllstoff untersucht.

Zunächst werden die Relaxoreigenschaften in sechs verschiedenen Zusammensetzungen von P(VDF-TrFE-CFE) untersucht. Von diesen sechs Zusammensetzungen werden drei (51.3/48.7/6.2, 59.8/40.2/7.3 und 70/30/8.1) zum ersten Mal analysiert. Der feldinduzierte Phasenübergang führt in einigen Zusammensetzungen zu einer doppelten Hystereseschleife. Durch die direkten elektrokalorischen Messungen zeigt sich, dass der durch das elektrische Feld induzierte Phasenübergang zu einer höheren elektrokalorischen Temperaturänderung führt. Die indirekten elektrokalorischen Messungen werden mit und ohne Kompensation des Leckstroms durchgeführt. Dabei wird festgestellt, dass die indirekte Methode aufgrund des Leckstroms zu fehlerhaften Ergebnissen führen kann. Die Ergebnisse der indirekten Messungen mit der Kompensation des Leckstroms sind mit denen der direkten Messungen vergleichbar. Die elektrischen Energiespeichereigenschaften der reinen Terpolymere werden mit denen ihrer Nanocomposites verglichen. Es zeigt sich, dass die gespeicherten und entladenen Energiedichten der Nanokomposite besser sind als die der reinen Terpolymere.

Schlüsselwörter: Elektrokalorischer Effekt, direkte Methode, indirekte Methode, ferroelektrisches Polymer, Relaxor, doppelte Hystereseschleife, elektrische Energiespeicherung, Nanokomposit

Table of Contents

Symbols & Abbreviations

AFE	Antiferroelectric
AFM	Atomic force microscopy
Ar	Argon
Å	Ångström
BDS	Breakdown strength
BNNs	Boron nitride nanosheets
BOPP	Biaxially oriented polypropylene
BSE	Backscattered electrons
BTO	Barium titanate
BZT	Zirconium doped barium titanate
C	Capacitance
CFE	Chlorofluoroethylene
CNTs	Carbon nanotubes
c_p	Specific heat capacity
d	Interchain spacing
d	Diameter of particle
DHL	Double hysteresis loop
DLCC	Dynamic Leakage Current Compensation
DMF	Dimethyl formamide
DQ_{EC}	Electrocaloric generated heat
DSC	Differential scanning calorimetry
$\vec{E}$	Electrical field
E_a	Activation energy
ECE	Electrocaloric effect
E_{cr}	Critical field
E_{max}	Maximum applied electric field
E_{off}	Electric field off
E_{on}	Electric field on
f	Frequency
f_0	Attempt frequency
FE	Ferroelectric
g	Gravitational acceleration
k	Boltzmann constant
K	Loss factor
L	Inductance
LGD	Landau-Ginzburg-Devonshire
MLCC	Multi-layered ceramics capacitor

NF	Nanofiber
NP	Nanoparticle
NW	Nanowire
P	Power density
P(VDF)	Polyvinylidene fluoride
P(VDF–HFP)	Poly(vinylidene fluoride – hexafluoropropylene)
P(VDF–TrFE)	Poly(vinylidene fluoride – trifluoroethylene)
P(VDF–TrFE–CFE)	Poly(vinylidene fluoride – trifluoroethylene – chlorofluoroethylene)
P(VDF–TrFE–CTFE)	Poly(vinylidene fluoride – trifluoroethylene – chlorotrifluoroethylene)
P(VDF–TrFE–HFP)	Poly(vinylidene fluoride – trifluoroethylene – hexafluoropropylene)
PET	Polyethylene terephthalate
P_{max}	Maximum polarization
PNR	Polar nano region
P_{rem}	Remnant polarization
PTFE	Polytetrafluoroethylene
PVD	Physical vapor deposition
PZT	Lead zirconium titanate
QP	Quasi-quadruple point
RC	Refrigerant capacity
SE	Secondary electrons
SEM	Scanning electron microscopy
SHL	Single hysteresis loop
SRO	Strontium ruthenate
SThM	Scanning Thermal Microscopy
t	Time
T_0	Curie-Weiss temperature
$tan\ \delta$	Dielectric loss tangent
T_B	Burns temperature
T_{bath}	Bath temperature
T_c	Curie transition temperature
T_f	Freezing temperature
T_g	Glass transition temperature
TrFE	Trifluoroethylene
$U_{discharged}$	Discharged energy density
U_{loss}	Lost energy
U_{stored}	Stored energy density
VDF	Vinylidenefluoride
XRD	X-Ray diffraction
σ	mechanical stress
γ	Degree of Dielectric Relaxation

Δh_{EC}	Enthalpy change generated by the ECE
$\Delta h_{measured}$	Specific enthalpy change
ΔS_{EC}	Electrocaloric entropy change
ΔT_{EC}	Electrocaloric temperature change
ε″	Imaginary part of permittivity
ε'	Dielectric constant
ε_0	Permittivity of free space
ε_r	Relative permittivity
η	Charge-discharge efficiency
θ	Curie constant
θ	Angle of incidence
ρ	Density
ρ_f	Density of fluid
ρ_p	Density of particle
τ	Thermal relaxation time constant
ω	Frequency
v	Sedimentation velocity of spherical particle

1 Introduction

The cooling industry is rapidly growing around the world. Cooling systems have always been crucial in energy production, chemical industries, and in other industrial sectors. As an outcome of miniaturization, e-mobility and digitalization, the cooling demands in microelectronic devices and gadgets, batteries, and in data centers are on the rise. The cold chain logistics, which is the temperature-controlled transport of commodities such as agricultural, food, and pharmaceutical products from one part of the world to the other, has increased the cooling demands due to globalization. The rise in the global temperature has boosted the energy demands for cooling in buildings, and is expected to increase further due to the climatic changes. [1] The cooling demand ingests over 50% of the total (peak) electricity consumption for the urban areas, in both developed and developing countries. All these factors pave way for the environmental-friendly alternative cooling technologies, such as thermoelectric, thermoacoustic, and caloric cooling. Among these alternatives, caloric cooling has gained reputation owing to its flexibility to utilize either pressure (barocaloric), magnetic field (magnetocaloric), mechanical stress (elastocaloric), or electric field (electrocaloric) to induce the temperature change. [2–9]

An electrocaloric cycle works by heating and cooling dielectric materials by applying and removing an electric field. [2, 3] Ferroelectric materials (ceramics, polymers) are particularly interesting for the electrocaloric effect (ECE), which is a temperature rise under adiabatic conditions or an increase in entropy under isothermal conditions, when an electric field is applied. [2, 4, 10–12] Ferroelectric polymers such as polyvinylidene fluoride (P(VDF)) based copolymer and terpolymer systems have gained special attention in recent years. Large values of electrocaloric temperature change (> 10 K) have been reported in these polymers through direct measurements. [13–16] In other reports, a negative electrocaloric effect (decrement in temperature upon the application of electric field) has been observed in P(VDF) based copolymers through indirect electrocaloric measurements, and is not confirmed through any direct measurement. [17–19] The study of the electrocaloric effect through indirect measurements in different materials is seeing an upward trend (Figure 1) as it is a cost-effective and fast method, and does not require specially designed equipments which are rather expensive and have long measurement duration. [20, 21]

The focus of this work is to study the electrocaloric effect in Poly(vinylidene fluoride – trifluoroethylene – chlorofluoroethylene) (P(VDF–TrFE–CFE) free-standing thick films through direct

and indirect measurement methods, and analysis of indirect measurement. Furthermore, the study of energy storage properties of P(VDF–TrFE–CFE) nanocomposites with inorganic filler is focused.

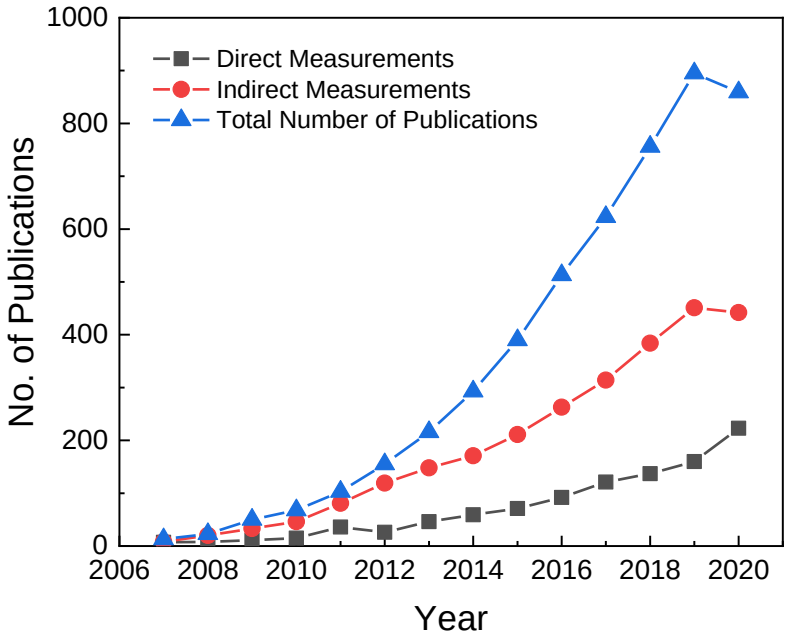

Figure 1 Number of publications on the topic of the electrocaloric effect and its direct and indirect measurement. According to [22]

This work is divided into five main chapters; each chapter is then subdivided into multiple sections. Chapter 2 provides the details of the topics that are relevant within the context of this work. There are three main sections that cover the following topics; namely, materials, electrocalorics, and electrical energy storage. In the beginning, this chapter gives a general introduction to the major ferroelectric polymers and the origin of ferroelectricity in them. The main material, that is fluoropolymer Polyvinylidiene fluoride (P(VDF)), is then discussed along with its different polymorphs and two copolymers, namely Poly(vinylidene fluoride – trifluoroethylene) (P(VDF–TrFE)) and Poly(vinylidene fluoride – trifluoroethylene – chlorofluoroethylene) (P(VDF–TrFE–CFE)). The second section of chapter 2 is dedicated to the electrocalorics. In section 2.2, the electrocaloric effect is discussed. The direct and indirect measurement methods for the electrocaloric effect are discussed in detail. The last section of chapter 2 focuses on the electrical energy storage properties of the dielectric polymers. The measurement methods of electrical energy storage are discussed.

The electrical storage properties of the fluoropolymer Poly(vinylidene fluoride – trifluoroethylene – chlorofluoroethylene) and its nanocomposites with inorganic ceramic nanofiller are described.

Chapter 3 is dedicated to the experimental details and describes the material synthesis and the characterization methods that are used within this work. The chapter begins with the list of compositions of Poly(vinylidene fluoride – trifluoroethylene – chlorofluoroethylene) that have been investigated in this work. The next part covers the preparation steps of the free-standing polymer and the polymer nanocomposite films. The precursors, parameters and stepwise synthesis of zirconium doped barium titanate nanoparticles via the hydrothermal route is described, which is used as the nanofiller to prepare the free-standing polymer nanocomposite films. The (material) structural characterization techniques, such as X-Ray diffraction (XRD) and scanning electron microscopy (SEM), which are used to characterize the synthesized nanoparticles and the polymer films, are discussed. The measurement methods, the employed apparatus and the parameters for the characterization of the functional properties (dielectric, ferroelectric, electrocaloric, and energy storage properties) of the polymer and the nanocomposite films are described in detail in Chapter 3.

Chapter 4 focuses on the results achieved in this work and their discussion. Chapter 4 has been subdivided into four sections; namely, comparison of ferroelectric and relaxor properties, study of different compositions of P(VDF–TrFE–CFE), study of the electrocaloric effect in P(VDF–TrFE–CFE), and study of P(VDF–TrFE–CFE) nanocomposites. The first section of Chapter 4, comparison of ferroelectric and relaxor properties, deals with the analysis of the ferroelectric copolymer P(VDF–TrFE) and the relaxor terpolymer P(VDF–TrFE–CFE) compositions. Their structural, thermophysical, dielectric, electromechanical, ferroelectric and relaxor properties are investigated and compared. The second section of Chapter 4 presents the study of six different compositions of P(VDF–TrFE–CFE) with special focus on their relaxor properties and electric field induced transition. The third section of Chapter 4 aims at the investigation of the electrocaloric effect in P(VDF–TrFE–CFE) through direct and indirect methods. The electrocaloric effect in different compositions of P(VDF–TrFE–CFE) has been directly measured using an in-house built quasi-adiabatic calorimeter. The indirect measurement of the electrocaloric effect has been conducted as well, and compared with the direct measurements. The last section of Chapter 4 focuses on the P(VDF–TrFE–CFE) nanocomposites containing zirconium doped barium titanate nanoparticles and its electrocaloric and electrical energy storage characteristics. The dielectric properties, polarization behavior, and electrical energy

properties of polymer nanocomposites of three different compositions of P(VDF–TrFE–CFE) with varying nanoparticle content have been examined.

In Chapter 5, the main results and findings of the presented work are highlighted as concluding remarks. Finally, the possible future aspects of the project are mentioned.

2 Background

Ferroelectric materials have significant importance from the perspective of industrial and commercial applications. With the discovery of ferroelectricity in the 1921 in the single-crystal material (Rochelle salt), the quest for the study of ferroelectricity in different materials has been ongoing. In 1940, the phenomenon of ferroelectricity was observed in the polycrystalline barium titanate (BTO) ceramic, followed by many other inorganic and organic material systems, such as lithium niobate, lithium tantalate, lead-based oxides, polyamides, fluorinated polymers etc. [23] In recent years, the focus of ferroelectric material research has shifted towards lead-free systems, owing to the toxic effect of lead on human health and the environment.

Ferroelectric materials are a sub-group of the dielectric materials which show switchable spontaneous polarization. The switching of polarization occurs under an applied electric field. The polarization loop of typical ferroelectrics is shown in Figure 2. Initially, the polarization is gradually increased as the domains start to be oriented in the direction of an applied electric field. At a certain magnitude of the applied electric field, all the domains have the same orientation (in the direction of electric field) or a relevant projection thereon and exhibit saturation polarization, obtained by drawing a straight line as depicted in Figure 2. The further increase in the polarization with the electric field is due to the induced polarization and can be distinguished from the spontaneous polarization. As the electric field is reduced to zero, the polarization shows a remnant effect due to the potential barrier which hinders the reorientation of the domains. The polarization decreases further and reaches its minimum at the coercive electric field in opposite field direction.

The ferroelectric property is a function of the crystal structure of the material. For example, barium titanate shows ferroelectricity in its tetragonal phase, but its cubic phase is paraelectric which is characterized by the absence of the spontaneous polarization. The ferroelectric to paraelectric phase transition temperature is given by the Curie temperature. It is related to the dielectric constant by equation 1. [23, 24]

$$\varepsilon_r = \frac{\theta}{T - T_0} \tag{1}$$

For a second order phase transition, θ is the Curie constant, ε_r is the relative permittivity or the dielectric constant, and T_0 is the Curie-Weiss temperature. For first order phase transition, there

must be a further differentiation between the Curie point (extrapolated from Curie-Weiss law (1)) and the Curie-temperature (actual phase transition).

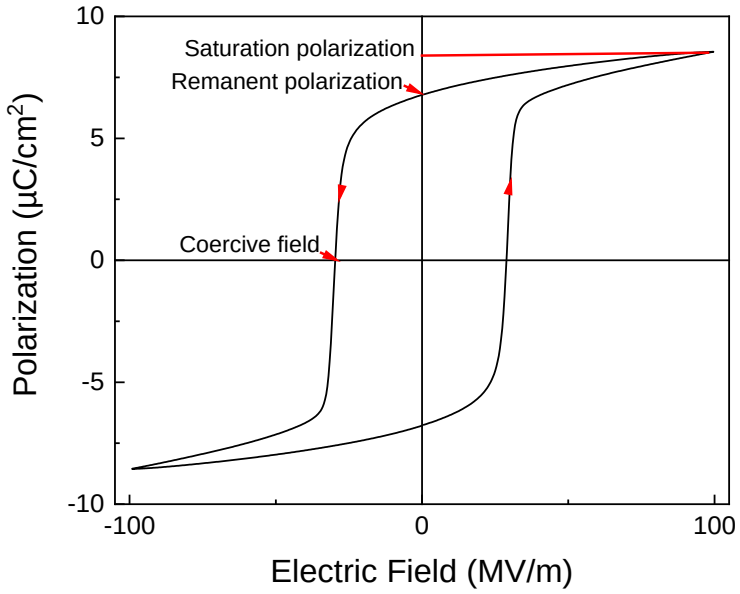

Figure 2 Typical polarization hysteresis curve for ferroelectric materials.

Parallel to the pure ferroelectric materials, relaxor ferroelectric materials have been also reported since the 1960s. [23] Relaxors show a different behavior compared to the pure ferroelectric materials. The relaxor characteristics in ceramic materials and single crystals are described by the presence of polar regions of nanoscale size which are called polar nano regions (*PNRs*) or nanodomains or polar clusters. These polar nano regions are formed due to a local charge disorder in the system, which is induced by chemical disorder in the system. When an electric field is applied, these polar nano regions orient themselves in the direction of the applied electric field. Upon the removal of the applied electric field, the PNRs reorient themselves randomly giving rise to a small remnant polarization. The dielectric permittivity curves of relaxors have a broad peak which shifts towards higher temperatures with increasing frequency. This peak represents the slowing down of PNR dynamics. [25, 26]

When relaxors are discussed, there are another two terms that come into play to describe their states, i.e. ergodic, and non-ergodic states. The term “ergodic” is borrowed from statistical mechanics where it is used to describe the energy surfaces. An ergodic process is defined in statistical mechanics when under defined conditions, the time average is equal to the ensemble

average. The concept of ergodicity can be better explained by imagining a flipping coin. The time average, which is the average of 4×10^{24} times subsequent flips of a coin, equals the ensemble average, which is the average of 4×10^{24} number of coins, each thrown once. This system becomes non-ergodic when the initial state of the 4×10^{24} coins is not random anymore. The terms “ergodic” and “non-ergodic” for relaxors were first proposed by Viehland et al. [27] Contrary to statistical mechanics, the term “ergodic” is also used for relaxors when the time average and the ensemble average will not lead to the same state with a probability of 100%, and the system will exhibit a quasi-ergodicity or varying degrees of non-ergodicity, as explained by Dittmer et al. [25] Relaxors are disordered systems with a freezing temperature. Figure 3 depicts that polar units of nanoscopic size, known as polar nanoregions (*PNRs*) form at the Burns temperature *(T_B).* Below the Burns temperature, the polar nanoregions are present within a non-polar matrix. Since the PNRs are highly dynamic and not correlated, the relaxor remains in an ergodic state. [25] The Burns temperature of inorganic relaxors is significantly higher than the freezing temperature, while for organic relaxors, the presence of the Burns temperature has not been reported yet.

In the vicinity of the freezing temperature *(T_f)*, the PNRs begin to interact with each other, therefore the ergodicity is broken and the relaxor shows glass-like behavior. As the interactions of PNRs reach their maximum, a configuration with random polarization directions is obtained. However, a high enough electric field can induce a ferroelectric transition in an ergodic as well as in a non-ergodic relaxor state. [25–28]

The freezing temperature can be determined from the dielectric spectra measured as a function of frequency and temperature by using the Vogel-Fulcher equation (Equation 2). [28]

$$f_0 = f \exp\left(\frac{E_a}{k(T_m(f) - T_f)}\right) \tag{2}$$

Where, $f = 1/\tau$, τ is the relaxation time, $T_m(f)$ is the corresponding temperature of the maximum of the dielectric permittivity, T_f is the freezing temperature, E_a is the activation energy, f_0 is the attempt frequency, and k is the Boltzmann constant.

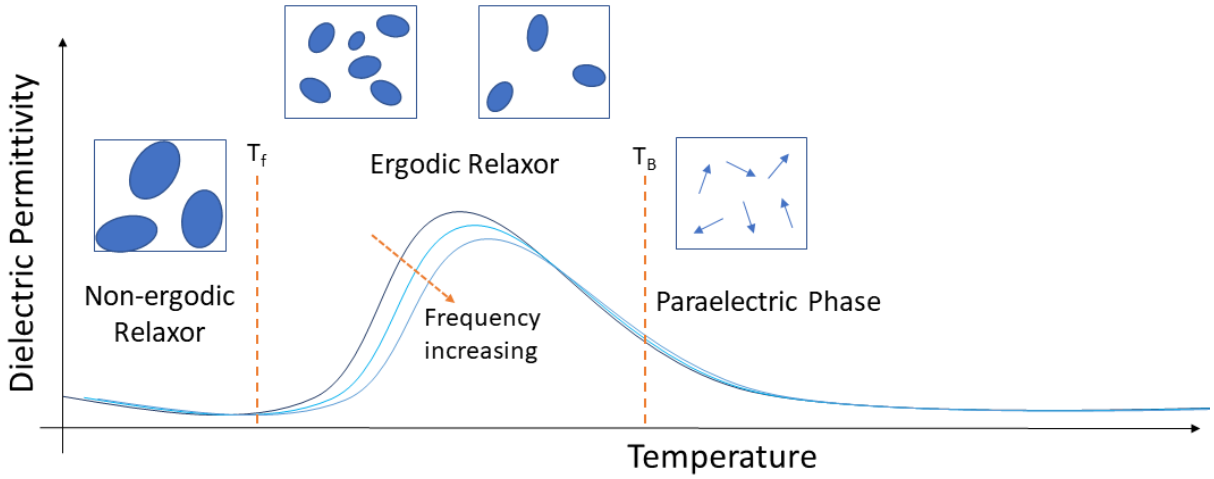

Figure 3 Evolution of different relaxor phases with temperature.

2.1 Ferroelectric Polymers

There are several known ferroelectric polymers; such as fluoropolymers, polyamides, cyanopolymers, polyureas, polythioureas, and liquid crystals. The ferroelectricity in polymers arises due to the electronegativity difference between the constituent atoms. The difference in electronegativity results in permanent dipoles, which flip their direction under an applied external electric field. Polyamide, which is commercially known as nylon, exhibits ferroelectricity. The amide group (NH–CO) in nylon possesses a dipole moment of 3.7×10^{-30} C·m. Broadly speaking, the odd-numbered nylons (nylons with odd number of carbon atoms in each segment e.g. nylon-7) are ferroelectric, because of a polar crystalline phase with parallel bonds. The even-numbered nylons, such as nylon-12 and nylon-6, have nonpolar crystalline structures with antiparallel bonds. The dipoles are cancelled due to the antiparallel bonds, and the even-numbered nylons do not exhibit ferroelectricity. These properties are significantly influenced by the processing conditions. The most widely studied ferroelectric polymers for the electrocaloric effect are Polyvinylidiene fluoride (P(VDF) based copolymers and terpolymers. [29, 30]

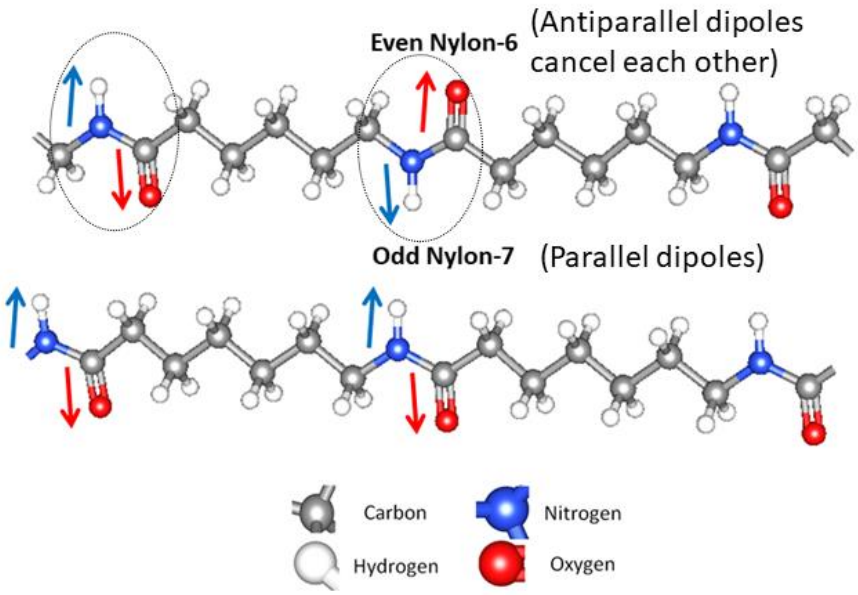

Figure 4 Ball stick structure of non-ferroelectric even nylon-6 and ferroelectric odd nylon-7.

2.1.1 Polyvinylidiene Fluoride (P(VDF))

Polyvinylidiene fluoride (P(VDF)) (Figure 5) was first synthesized in 1940. After the discovery of piezoelectricity in P(VDF) in 1969, P(VDF) was intensively studied for other properties and ferroelectricity in PVDF was reported in 1971. Ever since the first synthesis, the commercial applications of P(VDF) have rapidly grown. [29]

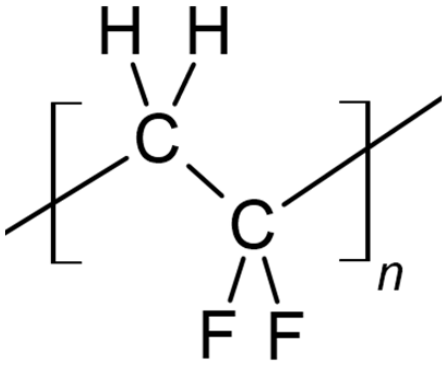

Figure 5 Schematic of molecular structure of Polyvinylidiene fluoride P(VDF).

Owing to the outstanding mechanical and physical properties, VDF based seals, gaskets, linings, wire insulation and cable jackets are widely available in the market. The piezoelectric, pyroelectric and ferroelectric properties of P(VDF) have broadened its application spectrum. Different copolymers and blends of P(VDF) have been introduced in the advanced functionalities. The prospective sophisticated applications of P(VDF) based systems include the mechanical, tactile, acoustic and temperature sensing, transistor, ferroelectric memory, printed flexible electronics and energy storage. [31–37]

Polyvinylidiene fluoride (P(VDF)) has the chemical formula $[–CH_2–CF_2–]_n$ (Figure 5). A monomer unit consists of two atoms, each of carbon, hydrogen, and fluorine. Fluorine is the leading electronegative element in the periodic table, with an electronegativity value of 4.0 on the Pauling Scale. While carbon and hydrogen have the electronegative values of 2.5 and 2.2, respectively. The huge difference between the electronegativity values of fluorine, hydrogen, and carbon results in a permanent dipole. The ferroelectricity in P(VDF) arises due to the permanent dipole on the $–CH_2–CF_2–$ monomer unit. The value of the dipole moment of the $[–CH_2–CF_2–]$ monomer unit varies between 3.4×10^{-30} C·m – 7×10^{-30} C·m. The value of the dipole moment depends on the chain conformation, which is defined as the arrangement of the carbon atoms along the chain. The chain

can be bent and twisted and its conformation is dictated by the interactions between the monomers causing the steric hindrance and the degree(s) of freedom for rotation about the σ bonds, resulting in polymorphism. Depending on the packing mode of the molecular chain, P(VDF) has polar as well as non-polar polymorphic crystalline phases. [29, 38–40]

2.1.2 Polymorphism in Polyvinylidiene Fluoride

The conformation of the P(VDF) chain is widely explained in terms of the torsional angle also known as the dihedral angle between the carbon atoms. The dihedral angle is a measure of torsion around the C−C−C−C bond along the backbone chain on two different planes. The trans conformation (T or t) has a dihedral angle of 180°, while the conformation having a dihedral angle of ±60° represents a gauche conformation, shown in Figure 6. To be precise, +60° refers to gauche$^+$ (G^+ or g^+) while −60° refers to gauche$^-$ (G^- or g^-). [29, 41, 42]

There are three well-known types of chain conformations of P(VDF), namely, TG^+TG^-, all trans- and $TTTG^+TTTG^-$, where *t* and *g* stand for trans (perpendicular) and gauche (adjacent), respectively (Table 1). PVDF has four known crystalline phases, namely, α, β, γ and δ. Both α and δ crystalline phases of PVDF have TG^+TG^- conformations. In both phases, the fluorine atoms possess the perpendicular and the adjacent positions to the carbon atom. In the α phase, the dipoles cancel each other owing to the TG^+TG^- conformation (Figure 6); hence the net dipole moment is zero. Therefore, the α phase is non-polar. When an electric field is applied, the α phase is transformed into the δ phase which is polar. This involves the rotation of every second chain segment by 180° about its axis, so that the transverse components of the dipole moments are in the same direction. It was proposed that the dipole reversal involves the propagation of a twist wave along the chains or small intramolecular rearrangements. [29, 42]

The most interesting electroactive phase of P(VDF) is the β phase owing to the largest dipole moment ~ 7×10^{-30} C·m. It has an (all) trans- chain conformation where all the fluorine atoms are oriented perpendicular to the carbon chain axis. When an electric field is applied, the dipoles orient themselves in the direction of electric field. In the polar γ phase, the chain has a $TTTG^+TTTG^-$ conformation. The dipole moment perpendicular to the chain direction is 4×10^{-30} C·m, while parallel to the chain direction, its value is 3.4×10^{-30} C·m. [29, 42]

Table 1 The structure & properties of different polymorphs of P(VDF). [29, 42]

Phase	Chain Conformation	Dipole Moment	State
α	TG^+TG^-	4×10^{-30} C·m (perpendicular) 3.4×10^{-30} C·m (parallel)	Non-polar
β	All trans-	7×10^{-30} C·m	Polar
γ	$TTTG^+TTTG^-$	4×10^{-30} C·m (perpendicular) 3.4×10^{-30} C·m (parallel)	Polar

In the early reports on P(VDF), it was presented that the axes of the crystalline regions of P(VDF) oriented themselves on the application of an electric field, and the molecular orientation occurred in a 60° increment. It was also reported that there was a 180° increment in the molecular reorientations under an applied field. Based on these models, a conclusion was presented that the 60° increment is more energetically favorable as compared to the 180° increments. Furthermore, the minimum in the (interchain) potential barrier was found out to be at 30°, describing the ease of the reorientation of the chain. This minimum in the potential energy facilitates the kink formation in the middle of the chain and propagation of the kink along the chain to produce a 60° chain rotation. In another work, it was assumed that the polarization switching in a domain is caused by the unhindered kink formation and propagation. Later, the theory was extended, and it was suggested that only those nuclei of domain can propagate along the chain, whose size was greater than a critical size. It was estimated that ~6 chain segments were involved to form a critical nucleus under an electric field of 100 MV/m at room temperature for the β-P(VDF). [29]

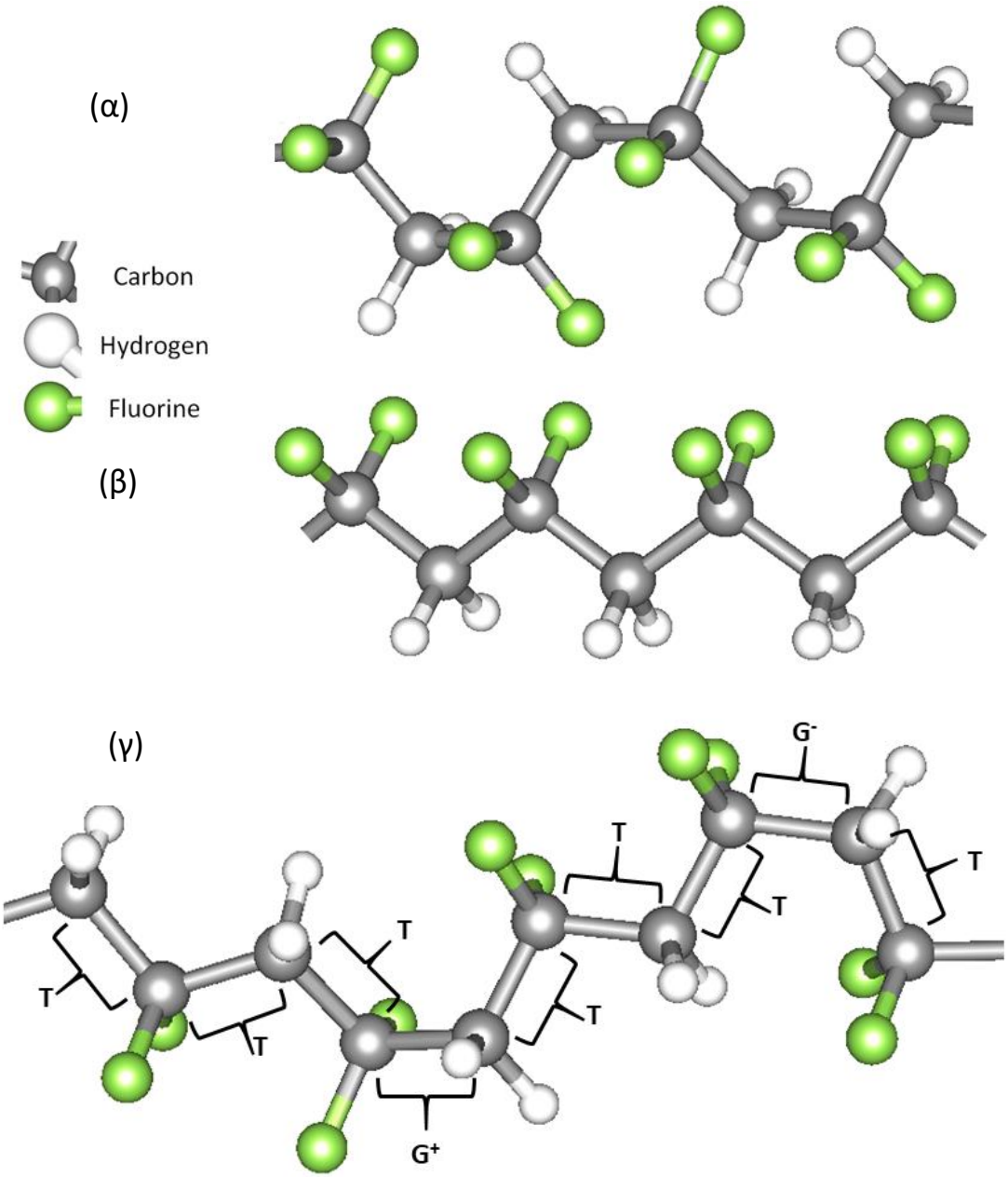

Figure 6 Ball stick structures of different chain confirmations of P(VDF), *TG* (α), *all-trans* (β), *TTTG⁺TTTG⁻* (γ).

The processing plays a key role in obtaining the respective crystalline phase of P(VDF). The formation of the crystalline phase is governed by the kinetics as well as the thermodynamics of the processing parameters. The crystallization of P(VDF) is strongly influenced by the temperature and cooling rate of the melt, cooling atmosphere and duration, solvent type, and its interaction with polymer. [43] Generally, the α phase can be readily achieved by slowly crystallizing the P(VDF) melt. When the α phase is poled, the δ phase can be obtained. The most desired crystalline phase is the β phase on account of its excellent electroactive properties which arise from the large dipole moment. The crystallization of the β phase in P(VDF) can be challenging, as the polarity of solvent is also a determining factor besides several other processing parameters. [44–47] This can be tackled by copolymerizing P(VDF) with other monomers. [29]

2.1.3 Copolymerization of Polyvinylidiene Fluoride

Although P(VDF) homopolymer shows a typical ferroelectric loop, an experimental evidence of the ferroelectric–paraelectric transition is not available. It has been suggested by theoretical studies that the Curie temperature of P(VDF) is above its melting temperature. [29, 48] In order to tune the Curie temperature, P(VDF) homopolymer is copolymerized with other monomers. The copolymerization of P(VDF) is performed with other polymers such as trifluoroethylene (TrFE), hexafluoropropylene (HFP), chlorotrifluoroethylene (CTFE), and chlorofluoroethylene (CFE). Some copolymers of P(VDF) are enlisted below, and their structures are shown in Figure 7. [40, 49–51]

- Poly(vinylidene fluoride – trifluoroethylene) (P(VDF–TrFE))
- Poly(vinylidene fluoride – hexafluoropropylene) (P(VDF–HFP))
- Poly(vinylidene fluoride – trifluoroethylene – chlorotrifluoroethylene) (P(VDF–TrFE–CTFE))
- Poly(vinylidene fluoride – trifluoroethylene – chlorofluoroethylene) (P(VDF–TrFE–CFE))
- Poly(vinylidene fluoride – trifluoroethylene – hexafluoropropylene) (P(VDF–TrFE–HFP))

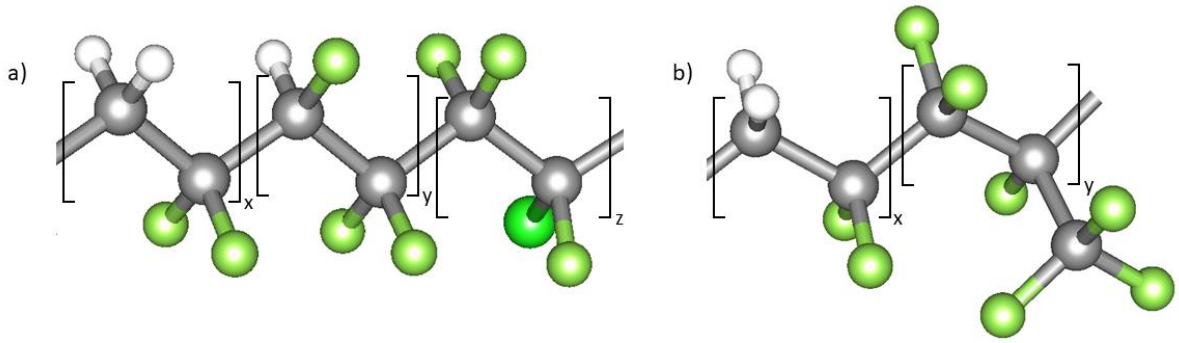

Figure 7 Ball stick structures of terpolymer and copolymer of P(VDF), (a) Poly(vinylidene fluoride – trifluoroethylene – chlorotrifluoroethylene) P(VDF–TrFE–CTFE), (b) Poly(vinylidene fluoride – hexafluoropropylene) P(VDF–HFP).

The copolymer Poly(vinylidene fluoride–trifluoroethylene) (P(VDF–TrFE)) and the terpolymer Poly (vinylidiene fluoride–trifluoroethylene–chlorofluoroethylene) (P(VDF–TrFE–CFE)) are discussed in this work.

2.1.4 Poly (vinylidiene fluoride–trifluoroethylene) Copolymer

Poly(vinylidene fluoride-trifluoroethylene) P(VDF–TrFE) (Figure 8) was first synthesized in 1979. It is a special copolymer of P(VDF), since it always crystallizes in the β-crystalline phase, which is a polar, and ferroelectric phase. The incorporation of bulky TrFE groups into P(VDF) chains weakens the intermolecular interaction between the chains and thermodynamic destabilization results in an all trans confirmation. The Curie temperature of the resulting copolymer P(VDF–TrFE) depends on the content of each monomer and varies from 55 to 128 °C with the VDF content varying from 55 to 88 mol %. P(VDF–TrFE) has larger remnant polarization than P(VDF), which consequently results in lower discharged energy density. The dielectric constant of P(VDF–TrFE) is higher (~18) than that of P(VDF) which is merely 6–12. P(VDF–TrFE) is one of the most studied copolymers, as its electrical properties can be tuned by using a high energy irradiation or addition of other monomer units. [29, 40]

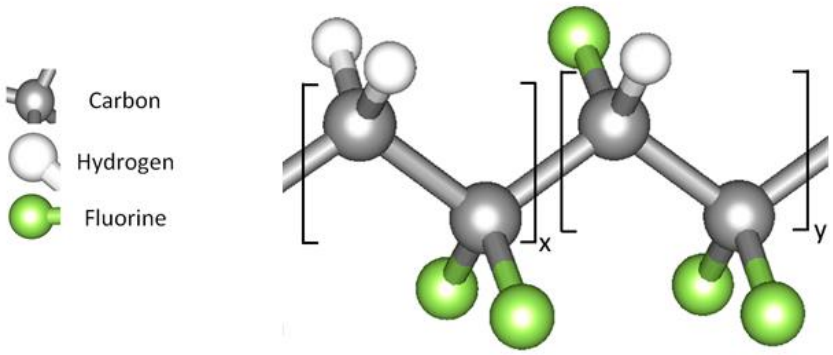

Figure 8 Ball stick structure of Poly(vinylidene fluoride-trifluoroethylene) P(VDF–TrFE).

2.1.5 Poly (vinylidiene fluoride–trifluoroethylene–chlorofluoroethylene) Terpolymer

In order to minimize the remnant polarization and hysteresis losses in P(VDF-TrFE) copolymers and to shift their transition temperature towards room temperature (relaxor properties), various techniques have been implemented, which includes electron beam and γ-beam irradiation, mechanical stretching, and defect modification. The term defect modification refers to the incorporation of another bulky monomer such as chloro-fluoroethylene (CFE), hexafluoropropylene (HFP), or chlorotrifluoroethylene (CTFE) into P(VDF-TrFE). [52–56]

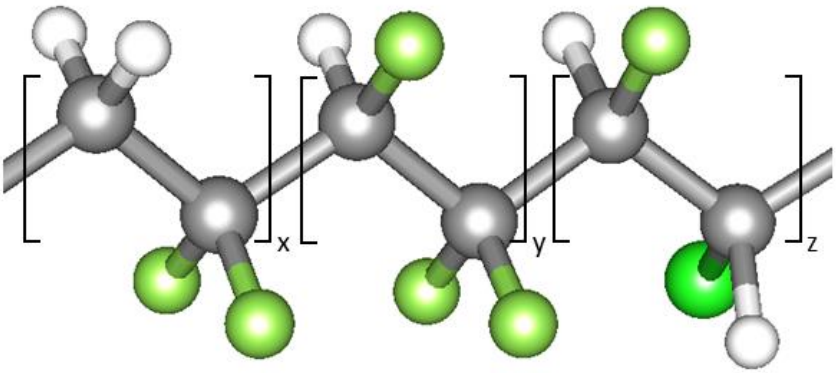

Figure 9 Ball stick structure of Poly (vinylidiene fluoride–trifluoroethylene–chlorofluoroethylene) P(VDF-TrFE-CFE).

According to the previous reports, terpolymers P(VDF-TrFE-CFE) (Figure 9) having a VDF/TrFE molar ratio ≤ 75/25 and a molar amount of CFE > 4 mol% show relaxor behavior with a broad and frequency-dependent peak maximum of the dielectric permittivity. [52, 53, 57] Both single hysteresis loops (SHL), which are typical for relaxors, as well as double hysteresis loops (DHL) have been

reported in P(VDF-TrFE-CFE), which are shown in Figure 10. [54, 58, 59] The presence of double hysteresis loops was attributed to the electric field-induced phase transition. However, the origin of double hysteresis behavior in P(VDF) based relaxors is not well-understood yet. [60] It was reported that both SHL and DHL behavior can be observed in the same polymer composition depending on the synthesis conditions. [55] Owing to a small remnant polarization and slim hysteresis, P(VDF_x-$TrFE_{1-x}$-CFE_y) terpolymers are attractive for energy storage applications. [55, 61] A large electrocaloric effect has been also reported in these materials. [62–64] P(VDF-TrFE-CFE) relaxors are characterized by a slim hysteresis loops, broad dielectric spectrum which has a frequency dispersion and high electrostrictive strain compared to the pure ferroelectric compositions. [40, 65]

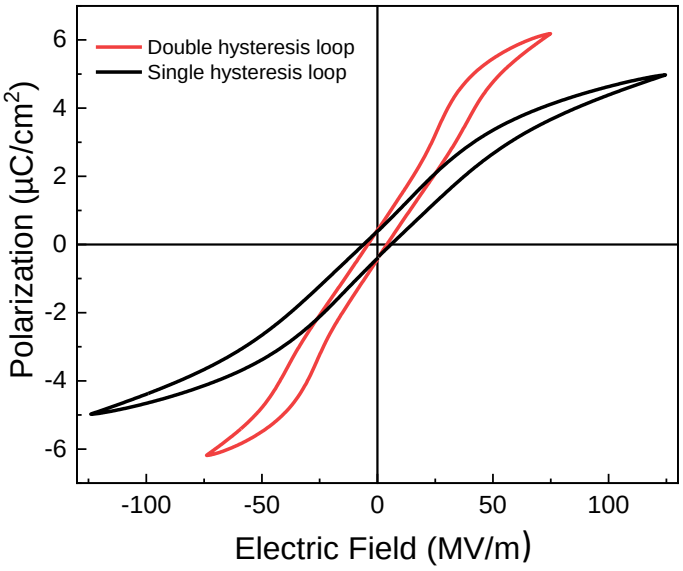

Figure 10 Single and double hysteresis loops observed in P(VDF-TrFE-CFE).

2.2 Electrocaloric Effect (ECE)

In terms of thermodynamics, the ECE can be explained as the adiabatic temperature change or the isothermal entropy change of a dielectric material in the presence of an electric field, as depicted in Figure 11. As specific entropy is a state function of the system in equilibrium, its differential for a dielectric material can be represented as: [10, 66]

$$dS = \left(\frac{\partial S}{\partial T}\right)_{\sigma,E} dT + \left(\frac{\partial S}{\partial \sigma}\right)_{T,E} d\sigma + \left(\frac{\partial S}{\partial E}\right)_{T,\sigma} dE \tag{3}$$

For the sake of simplicity, the tensor notations for mechanical stress (σ), and electrical field (*E)* are omitted. Under constant mechanical stress, dσ = 0, the equation will be:

$$dS = \left|\frac{\partial S}{\partial T}\right|_{E,\sigma} dT + \left|\frac{\partial S}{\partial E}\right|_{T,\sigma} dE \tag{4}$$

Under isothermal conditions (dT = 0), the first term in Equation 4 is equal to zero. The second term satisfies the Maxwell relation.

$$\left|\frac{\partial S}{\partial E}\right|_{T,\sigma} = \left|\frac{\partial P}{\partial T}\right|_{E,\sigma} \tag{5}$$

Under adiabatic conditions,

$$dQ = TdS = 0 \tag{6}$$

Hence, Equation 4 can be written as:

$$\left|\frac{\partial S}{\partial T}\right|_{E,\sigma} dT = -\left|\frac{\partial P}{\partial T}\right|_{E,\sigma} dE \tag{7}$$

$$dT = -\left|\frac{\partial P}{\partial T}\right|_{E,\sigma} \left[\left|\frac{\partial S}{\partial T}\right|_{E,\sigma}\right]^{-1} dE \tag{8}$$

$$T\left|\frac{\partial S}{\partial T}\right|_{E,\sigma} = c_{\sigma,E(T)} \tag{9}$$

$$dT = -\frac{T}{c_{\sigma,E(T)}}\left|\frac{\partial P}{\partial T}\right|_{E,\sigma} dE \tag{10}$$

Here, $c_{\sigma,E(T)}$ is the heat capacity at constant stress and electric field. [10, 66]

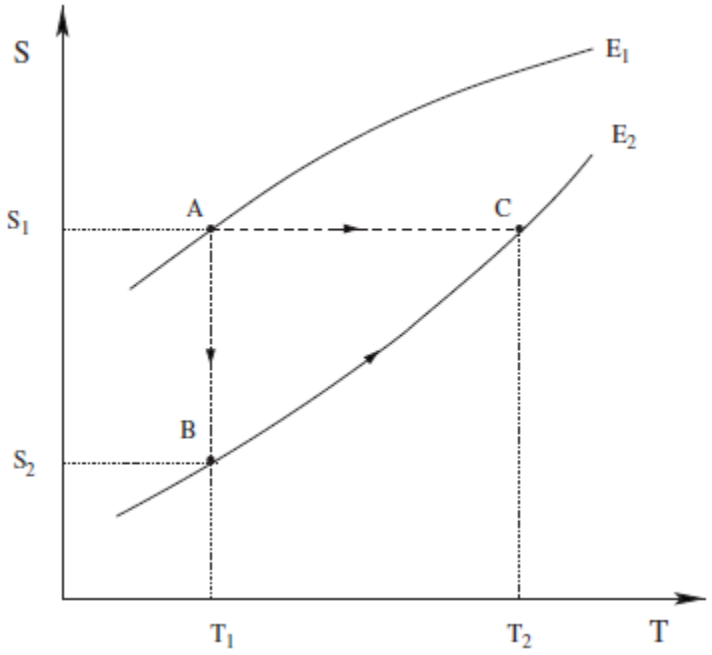

Figure 11 Schematic of the electrocaloric *T-S* diagram. [67]

When the electric field is changed from E_{min} to E_{max},

$$\Delta T_{EC} = -\int_{E_{min.}}^{E_{max.}} \frac{T}{c_{\sigma,E(T)}}\left|\frac{\partial P}{\partial T}\right|_{\sigma,E} dE \tag{11}$$

Finally, the isothermal entropy change is,

$$\Delta S_{EC} = \int_{E_{min.}}^{E_{max.}} \left|\frac{\partial P}{\partial T}\right|_{\sigma,E} dE \tag{12}$$

The Equations 11 and 12 are employed as an indirect method for the estimation of the electrocaloric entropy and temperature changes which will be discussed in detail in Section 2.2.2. [66]

Broadly speaking, the applied electric field orders the electric dipoles in a dielectric material and consequently lowers its dipolar entropy or, under adiabatic conditions, increases the temperature

resulting in a positive electrocaloric effect. However, a negative or an inverse electrocaloric effect, where the isothermal entropy change (ΔS_{EC}) is positive, while the adiabatic temperature change (ΔT_{EC}) is negative under an applied electric field, can also arise in certain materials under specific conditions. Such an inverse electrocaloric effect has been experimentally observed in antiferroelectric (AFE) and ferroelectric (FE) materials, which show transitions between different ferroelectric phases having distinct polarization directions. Moreover, in certain polar defect configurations in FE materials, a negative electrocaloric effect has been indicated. In all these cases, the inverse effect occurs in a specific temperature region and for a certain voltage amplitude. An increase in entropy in a dipolar system under an applied electric field, which is not so obvious, has been explained in terms of (different) directions of an applied electric field relative to the spontaneous polarization in the reported literature. The applied electric field can create a disorder in the alignment of the electric dipoles when the electric field is applied along a direction that is either non-collinear or antiparallel to the direction of the spontaneous electric polarization in the ferroelectric material. This disorder in the alignment of the dipoles under an applied electric field increases the entropy and leads to an inverse or negative ECE. Several studies have suggested to use the combination of the conventional and inverse/negative ECE to attain a significant overall electrocaloric temperature change for optimized EC cooling cycles in designed devices. [21, 66, 68, 69]

The operation of the EC cooling cycle can be explained in terms of the Brayton cycle. The schematic diagram of the EC cooling cycle is shown in Figure 12 consisting of four states (1 – 4). [21, 70]

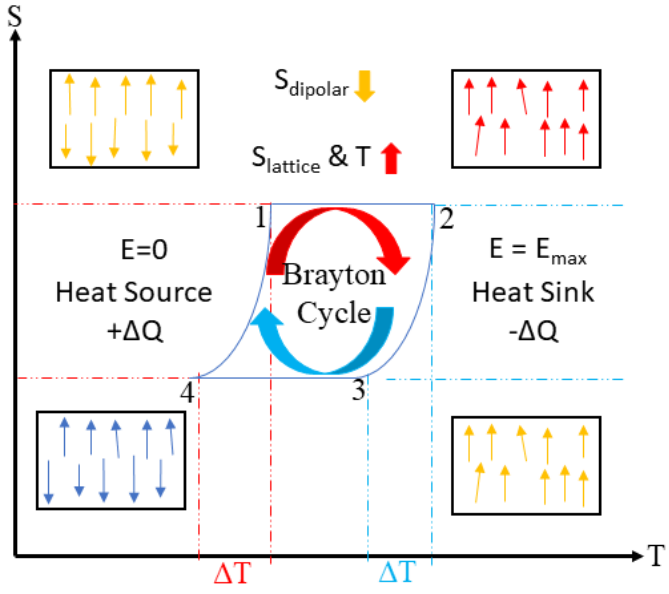

Figure 12 Brayton cycle for the electrocaloric cooling. (According to [21])

At state 1, the initial state of the cycle with no applied electric field ($E = 0$) having a high entropy with randomly oriented dipoles is depicted. An electric field ($\Delta E = E_{max}$) is applied between state 1 to state 2, which aligns the dipoles in the direction of an applied electric field causing the dipolar entropy to decrease, which is compensated by an increase in the lattice entropy, and the temperature increases adiabatically. The transition between state 1 and state 2 is an adiabatic process where there is no heat exchange with the surroundings. Between state 2 and state 3 is an isoelectric process (heat is exchanged with the surroundings), and the heat is removed from the system to the sink, lowering the temperature as well as entropy. Moving from state 3 to state 4, the applied electrical field is removed ($\Delta E = -E_{max}$), and the dipoles again become randomly oriented. The whole cycle repeats itself when the materials are heated up by absorbing the heat from the source or load (such as the interior of a refrigerator). [21, 70] The heat that can be transferred through an EC material between the cold and hot reservoirs is called the refrigerant capacity, *RC* represented Equation 13. [10]

$$RC = \int_{T_C}^{T_H} \Delta S_{max}(T)dT \tag{13}$$

where T_C and T_H are temperatures of the cold and hot reservoirs, respectively, and ΔS_{max} corresponds to the ΔS peak maximum. The ratio between the effective heat supplied or removed by a heat pump or cooling system, ΔQ, divided by the work required, ΔW, gives the coefficient of

performance (COP), $COP = \frac{\Delta Q}{\Delta W}$. *COP* is specific for each thermodynamic cycle. The COP of an ideal Brayton cycle is given in Equation 14. [10, 71]

$$COP = \frac{T_4}{T_3 - T_4} \tag{14}$$

2.2.1 Methods of Electrocaloric Measurement

There are various methods for the measurement of the electrocaloric temperature or entropy change, which can be categorized on the measurement principle, as shown in Figure 13. [10, 21, 71]

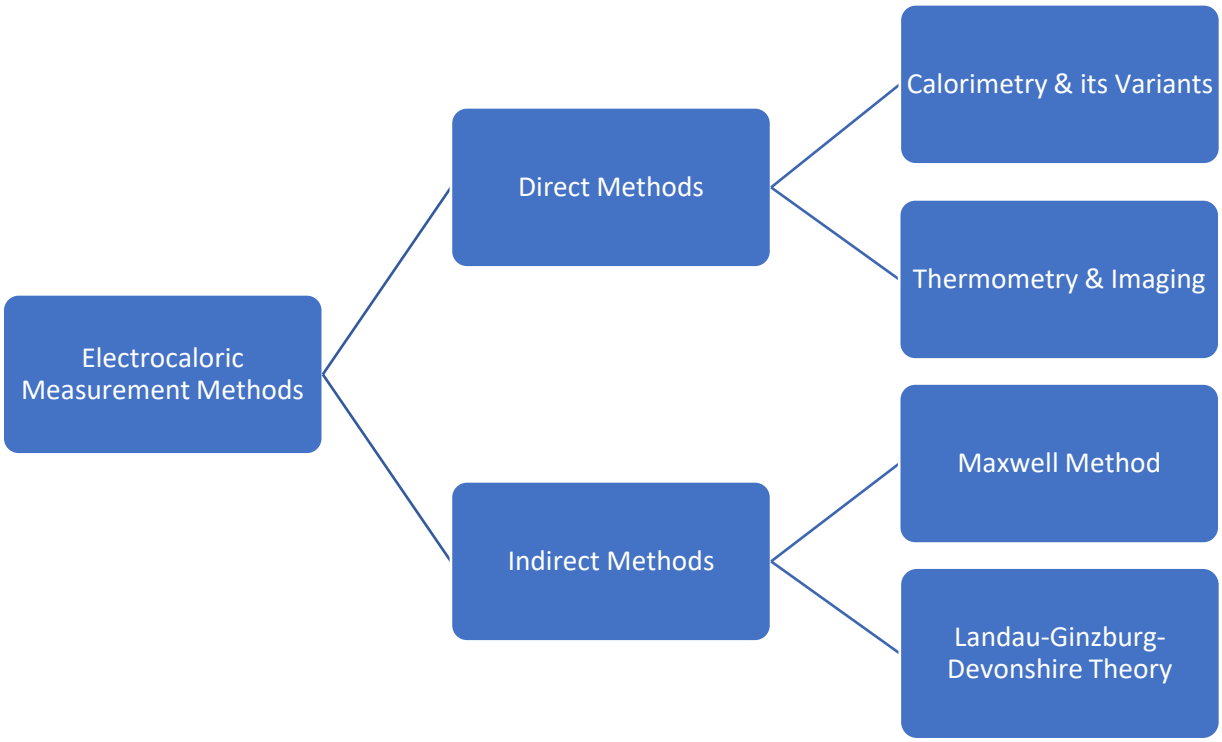

Figure 13 The measurement methods of the electrocaloric effect.

2.2.1.1 Calorimetry & its Variants

2.2.1.1.1 Modified Dynamic Scanning Calorimetry (DSC)

The modified differential scanning calorimetry (DSC) is a standard method for measuring the electrocaloric entropy change. The DSC devices are either built on the principle of heat flux or power compensation. The DSC designed on the heat flux principle has a single heating source for the reference pan as well as for the sample. The difference in temperature between the sample and the reference is recorded and is converted to the power difference which ultimately gives the difference in heat flow. On the other hand, the power compensated DSC has two separate heating sources, one for the sample and the other for the reference. The difference in temperature between the reference and the sample is kept close to zero by adjusting the heat flow in the power compensated DSC. Both models can be modified to obtain the Δh_{EC} (enthalpy change generated by the ECE) under isothermal conditions as shown in Figure 14. [72–74]

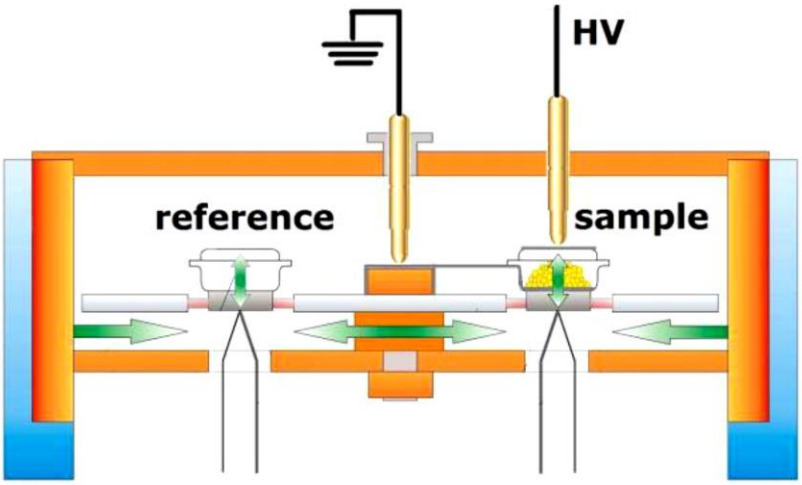

Figure 14 Schematic illustration of a modified dynamic scanning calorimetry for the electrocaloric measurement under isothermal conditions. [72]

The electrocaloric measurements in the DSC are conducted by heating the sample to the set temperature and allow the temperature to stabilize to achieve isothermal conditions. The electric field is then switched on and an exothermic peak is obtained that denotes the heat release to the environment. While, when the electric field is turned off, an endothermic peak is obtained as an output signal, shown in Figure 15. The area under the exothermic and endothermic peaks is then integrated and normalized to the sample volume to obtain the specific enthalpy change $\Delta h_{measured}$. The loss factor (K) due to the heat flow through the electric contacts is calculated and multiplied to

the measured specific enthalpy change $\Delta h_{measured}$ to obtain the effective Δh_{EC} as in Equation 15. [72, 75]

$$\Delta h_{EC} = h_{measured} \cdot K \tag{15}$$

Subsequently, the electrocaloric entropy change is calculated by $\Delta S_{EC} = \frac{\Delta h_{EC}}{T}$. The electrocaloric temperature ΔT_{EC} is calculated by dividing the Δh_{EC} with the specific heat capacity (c_P) of the sample measured as a function of the temperature (Equation 16). [21, 72, 75]

$$\Delta T_{EC} = \frac{\Delta h_{EC}}{c_p(T)} \tag{16}$$

It is very often that the specific heat capacity of the sample is measured only as a function of the temperature and the influence of the electric field on the specific heat capacity is not considered. This issue will be discussed in detail in Section 2.2.3.1. [21, 72, 75–78]

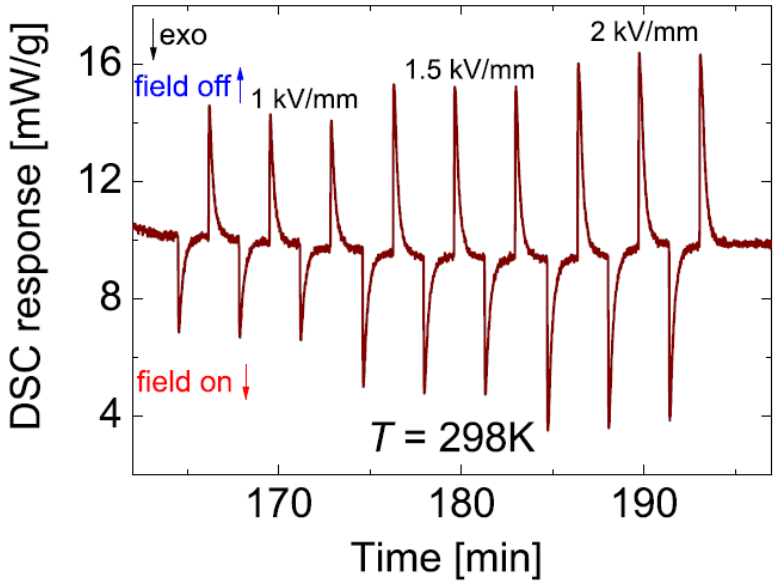

Figure 15 Output data obtained during the electrocaloric measurement using a modified scanning calorimetry. [72]

2.2.1.1.2 Calorimeter

A calorimeter is used by few research groups to measure the electrocaloric heat released/absorbed (Q_{EC}) by the material. When the short electric pulse of duration time (t) is applied to the resistor (R_0), Joule heat (Q_R) is produced by the resistor. As the magnitude of the applied voltage, V is

varied, the value of Q_R also changes. When the voltage signal peaks generated by the EC sample and the reference heater (detected by the heat flux sensor) have the same integrated areas, the EC heat released or absorbed by the sample (Q_{EC}) is equal to the Joule heat produced by the resistor (Q_R) . Thus, the Q_{EC} is obtained using Equation 17 by comparing the area of the endothermic peak produced by the sample to the area of the exothermic peak produced by the reference resistor. [62, 79–81]

$$\Delta Q_{EC} = \Delta Q_R = \frac{V^2 t}{R} \tag{17}$$

The directly measured quantity is the electrocaloric heat (Q_{EC}), and the electrocaloric temperature change ΔT_{EC} is calculated as, $\Delta T_{EC} = \frac{Q_{EC}}{c_p}$.

2.2.1.2 Thermometry & Imaging

2.2.1.2.1 Quasi-Adiabatic Calorimetry

A customized calorimeter was designed to measure the electrocaloric temperature change under the quasi-adiabatic conditions as shown in Figure 16. [83] The sample is hanged inside the inner chamber, while the middle chamber has the heating and cooling windings around it, which regulate the desired set temperature. A *Kapton®* insulated thermocouple of type K was attached to the sample using an alumina compound glue to sense the temperature variation in the sample upon the application or removal of the dc electric pulse (Figure 16). The operating range of the reported calorimeter is 260 K to 440 K, and it can be used to measure the EC effect in bulk ceramics, multilayer ceramic capacitors as well as in free-standing thick polymer films. [82, 83] This same quasi-adiabatic calorimeter is used within this work and will be discussed in detail in Section 3.2.3.

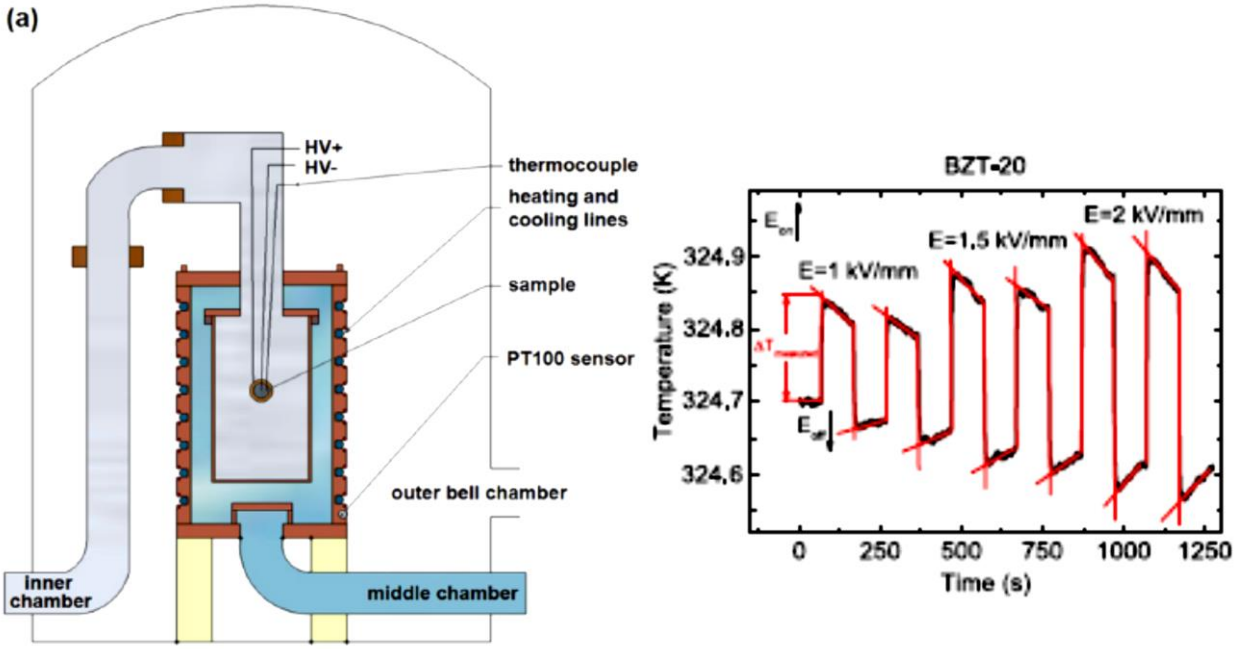

Figure 16 (a) Schematic illustration of a quasi-adiabatic calorimeter (b) data recorded during the electrocaloric measurement using a quasi-adiabatic calorimeter. [83]

As can be seen in Figure 16, there is a thermal diffusion during the time interval between the application and removal of the dc pulse. This thermal diffusion has been attributed to the heat radiation in the reported work, and the non-ideal quasi-adiabatic conditions within the calorimeter are verified. The thermal relaxation time constant was approximated to Equation 18. [83]

$$\tau \sim \frac{c_p}{4T_{bath}^3} \tag{18}$$

Where, τ is the thermal relaxation time constant, c_p is the specific heat capacity of the sample and T_{bath} is the bath temperature. The duration of the thermal diffusion or relaxation (τ) was reported to be shortest for the large electrocaloric temperature change. The values of the electrocaloric temperature change obtained using this custom-designed quasi-adiabatic calorimeter have been reported to show a good agreement with the values measured with the modified DSC and infra-red camera, as depicted in Figure 17. [83]

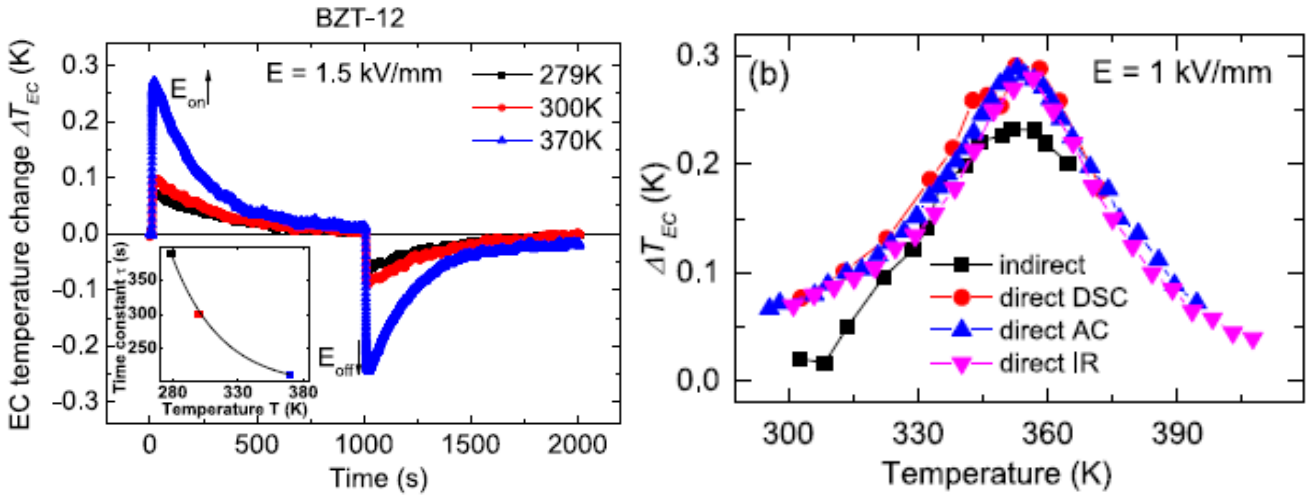

Figure 17 (a) Thermal diffusion in a quasi-adiabatic calorimeter during the electrocaloric measurement (b) comparison of the electrocaloric measurements through different methods. [83]

Recently, another customized calorimeter has been reported, which is developed by modifying Peltier-element based adiabatic scanning calorimetry (Figure 18). This calorimeter has two modes of operation, and can be used to measure the isothermal heat flow as well as the quasi-adiabatic temperature change. The calorimeter consists of a sample platform equipped with an electrical heater and a thermoresistor. A small Peltier element is used as a differential thermometer between the sample holder which is made of a copper block and the surrounding shield. The sample is mounted with silver paste onto the copper block (sample holder). Adiabatic conditions are realized by controlling the temperature of the shield to ensure that there is no temperature difference between the sample and the shield. This is done by a proportional- integrating *(PI)* loop aimed at keeping the Peltier-element voltage at zero. The electrocaloric enthalpy change induced by the applied/removed electric field is estimated by the heat flow from the sample to the shield through the calibrated Peltier element integrated over time. This is done by monitoring the voltage over the Peltier element, which is calibrated through a defined procedure. The heat flux across the Peltier element from the sample to the shield caused due to the electrocaloric effect in the sample is recorded through the calibrated Peltier voltage. The electrocaloric temperature change is measured as the difference between the average initial temperature values and the maximum temperature that is measured just after the electric field is on. Considering the short time span, it is assumed that there is no heat flow through the Peltier element yet, due to too short timespan for the heat to flow

to the shield, and the determined temperature change is measured under quasi-adiabatic conditions. [84] This method is not suitable for samples with low heat capacity.

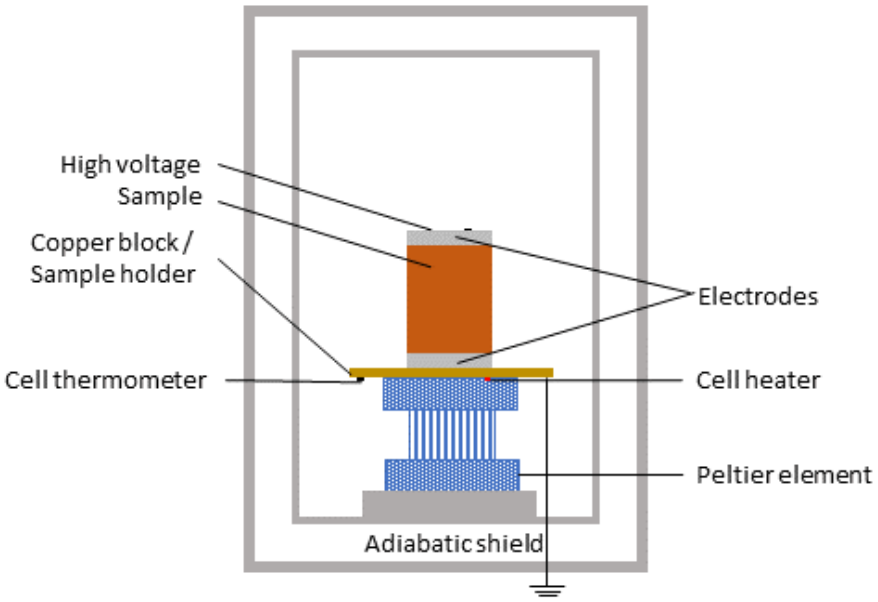

Figure 18 Schematic illustration of a customized calorimeter for the direct electrocaloric measurements. (According to [84])

2.2.1.2.2 Infrared Imaging

Another way to measure the electrocaloric temperature change is the infrared imaging technique, which is a non-contact method (Figure 19). The infrared sensing technique works on the principle of Planck's radiation law, which states that every physical object emits electromagnetic radiation continuously, and the emitted spectrum depends on the temperature of the object. The spectral radiance ($L(\lambda, T)$) of an object at temperature (T) having wavelength (λ) is given by: [85, 86]

$$L(\lambda, T) = \frac{2hc^2}{\lambda^5} \cdot \left[e^{\frac{hc}{\lambda k_B T}} - 1 \right]^{-1} \tag{19}$$

Where, h is Planck's constant, c is the speed of light in vacuum and k_B is the Boltzmann constant. The output signal of the detected infrared radiation is the voltage $V(T)$ which is directly proportional to the integral of the spectral radiance over the wavelength range of the sensor spectral sensitivity, $S(\lambda)$:

$$V(T) = K_I \int S(\lambda) \cdot \Theta(\lambda) \cdot L(\lambda, T) d\lambda + V_0 \quad (20)$$

Where, the integral limits are defined as the detector signals over a large area and/or certain time interval, K_I represents the conversion factor of the sensing electronic hardware, $\Theta(\lambda)$ has a value that depends on the size and emissivity of the sample, the transmission of the optical layout and the intermediate medium in the spectral range of the sensor sensitivity, while V_0 is the background signal. [87] The emissivity of the sample is increased by coating the top electrode of the sample with carbon ink which has an emissivity close to 1. Fast measurements are only possible, if the frame rate of the infrared camera is high enough to capture the temperature change in the sample within milliseconds. The frame rate of the camera and the spatial resolution are important features to obtain reliable results. Another variation of the infra-red method is reported by Sotnikova et al. and called as the mid-infrared method. They used a high-speed narrowband immersion lens photodiode to directly measure the pyroelectric coefficient. Equation 11 is employed to estimate the electrocaloric temperature change through the pyroelectric coefficient. [87]

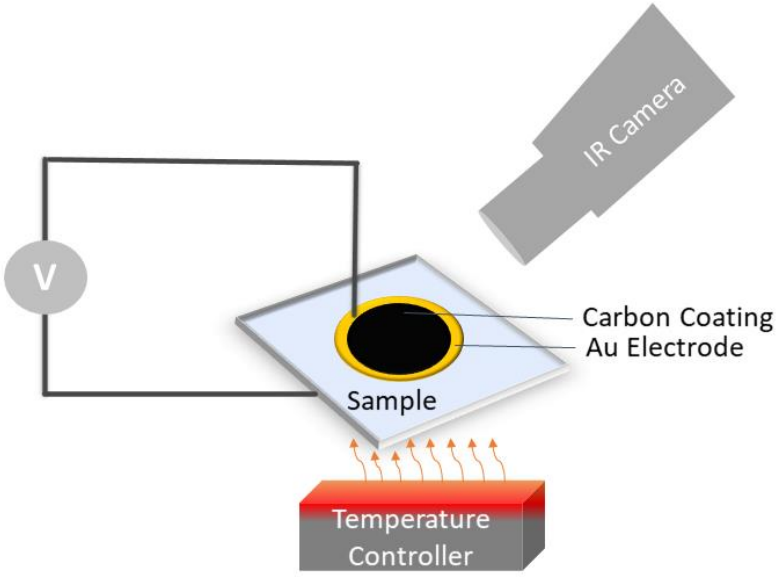

Figure 19 Schematic illustration of an infrared camera setup for the electrocaloric measurement. [81]

Tong et al. reported a customized setup for the direct measurement of the electrocaloric temperature change (Figure 20). The reported setup worked on the principle of thermoreflectance, which means that the temperature dependent optical reflectivity is measured as an output signal. They studied a lead zirconium titanate (PZT) thin film (150 nm) with strontium ruthenate (SRO) as

the top and bottom electrodes. The top electrode is sputter-coated with vanadium that reflects the laser beam to measure the thermoreflectance. Sinusoidal voltage waves are applied to the sample to induce the electrocaloric temperature change, which is then measured through the variation in the optical reflectivity of the vanadium layer by monitoring the intensity of the laser beam. [88]

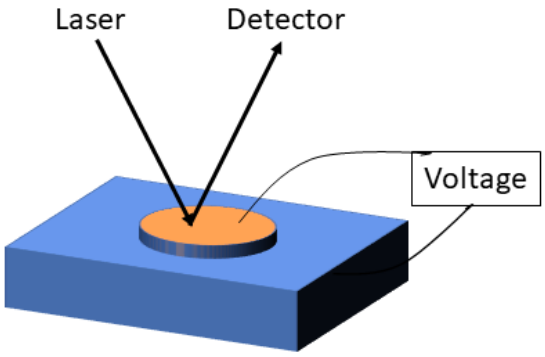

Figure 20 Schematic illustration of the electrocaloric measurement setup that works on thermoreflectance. (According to [88])

2.2.1.3 Scanning Thermal Microscopy (SThM)

Scanning thermal microscopy is a direct electrocaloric measurement method (Figure 21). It is capable to measure the ECE in a material on a much smaller scale, such as on the scale of the grain size. The SThM is based on the simultaneous detection of the interaction force between the tip and the sample (like conventional atomic force microscopy (AFM)) and the measurement of the localized temperature change in the sample through a special probe which is integrated in the AFM tip-cantilever assembly.

The detected signal in the SThM is related to a heat flux between the sample surface and the sensor, $\dot{Q}_{ts} \sim (T_{sample} - T_{sensor})/R_{ts}$. This heat flux depends on the temperature difference between the sensor and the sample as well as on the thermal contact resistance, R_{ts}. This implies that the temperature resolution of SThM is limited not only by the intrinsic noise of the sensor, but also by R_{ts}. Since, the thermal contact resistance has an inversely proportional relation to the effective thermal contact area, it is not possible to simultaneously achieve maximum temperature and spatial resolution using this method. However, for a spatial resolution of 10 nm, a temperature sensitivity of 0.1 K can be reasonable. [10, 81]

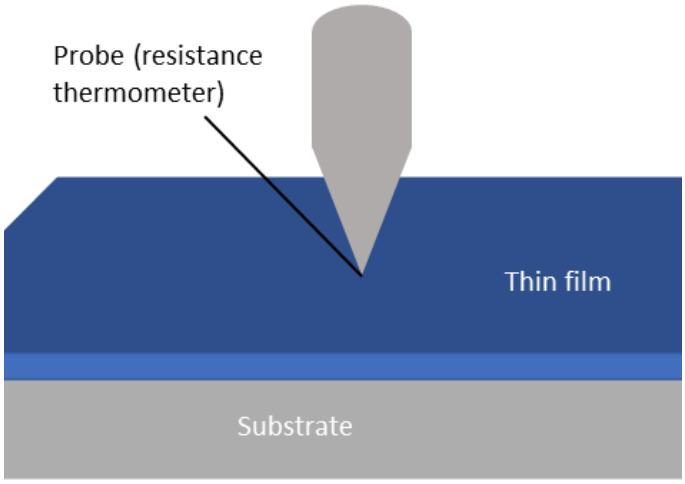

Figure 21 Schematic illustration of the scanning thermal microscopy (SThM).

Table 2 Highlighting the measuring quantity, advantages & limitations of each direct method for electrocaloric measurement.

Characterization Techniques	Advantages	Limitations
Thermometry	▪ Direct temperature measurement ▪ Fast response time ▪ Easy to realize ▪ Short measurement duration	▪ For large inactive volume, significant corrections required

Calorimeter	▪ Direct enthalpy measurement under isothermal conditions ▪ High sensitivity ▪ Good insulation of the calorimeter	▪ Measurement of c_p required ▪ Delayed response time ▪ Extensive modification of setup necessary ▪ Long time measurements ▪ Sample size (lateral) restriction
Quasi-Adiabatic Calorimeter	▪ Direct temperature measurement under quasi-adiabatic conditions ▪ Short measurement duration	▪ Delayed response time ▪ Complicated setup ▪ Corrections required ▪ Maximum applied voltage 1500 V
Thermal Imaging	▪ Non-contact method ▪ High spatial resolution ▪ Fast response time ▪ Spatial mapping of ECE possible	▪ Intensive calibration required ▪ Below room temperature measurement not possible
Scanning Thermal Microscope	▪ High temperature sensitivity ▪ High spatial resolution ▪ Measurement of ECE at nanoscale ▪ Spatial mapping of ECE possible	▪ Very long measurement duration

2.2.2 Indirect Method of Electrocaloric Measurement

The direct measurement methods for electrocaloric temperature and entropy changes require expensive devices which need to be modified and precisely calibrated to obtain reliable values. The devices must be operated either under isothermal or adiabatic conditions which are difficult to realize. This hinders the quick estimation of the ECE in new materials. An alternative approach to estimate the ECE temperature and entropy changes in a material is the indirect method.

2.2.2.1 Maxwell Relations

The most widely used method to deduce the electrocaloric temperature or entropy change is the Maxwell approach (Equations 11 and 12). In order to employ the indirect method, the first step is to record the polarization hysteresis curves over a range of temperatures usually under a bipolar (AC) field. However, it has been recently reported that the *P – E* curves recorded using a unipolar (DC) field may also be used for the Maxwell method [22]. In both cases, the polarization values from the discharge loop of the 1st quadrant are considered. The hysteresis curves are fitted to finally get the electrocaloric entropy and the temperature change. As shown in Figure 22, the procedure is initiated by the extraction of the polarization values at a definite electric field from the *P – E* curves, that are measured over a range of temperatures. It is important that the polarization values are extracted at small electric field intervals to have sufficient data points for the fitting. The extracted polarization values are then plotted against the temperature and the derivative $\frac{\partial P}{\partial T}$ is calculated. The derivative of polarization with respect to the temperature $\frac{\partial P}{\partial T}$ is known as the pyroelectric coefficient. The pyroelectric coefficient is then plotted and fitted with a polynomial of higher order, usually of the 4th or 6th order. The fitted data is then integrated over the electric field (E_{min} to E_{max}). The integrated values give the electrocaloric entropy change $\Delta S_{EC} = \int_{E_{min.}}^{E_{max.}} \left|\frac{\partial P}{\partial T}\right|_E dE$.

Subsequently, the electrocaloric temperature change can be calculated $\Delta T_{EC} = -\int_{E_{min.}}^{E_{max.}} \frac{T}{\rho c_P}\left|\frac{\partial P}{\partial T}\right|_E dE$ by multiplying the calculated EC entropy change values with the measurement temperature and dividing by the specific heat capacity (c_P) and density (ρ). [81] It is important to mention that although the specific heat capacity is written inside the integral, yet it is very often that the electric field dependence and even the temperature dependence of the specific heat capacity are not considered. This topic will be discussed in detail in Section 2.2.3.

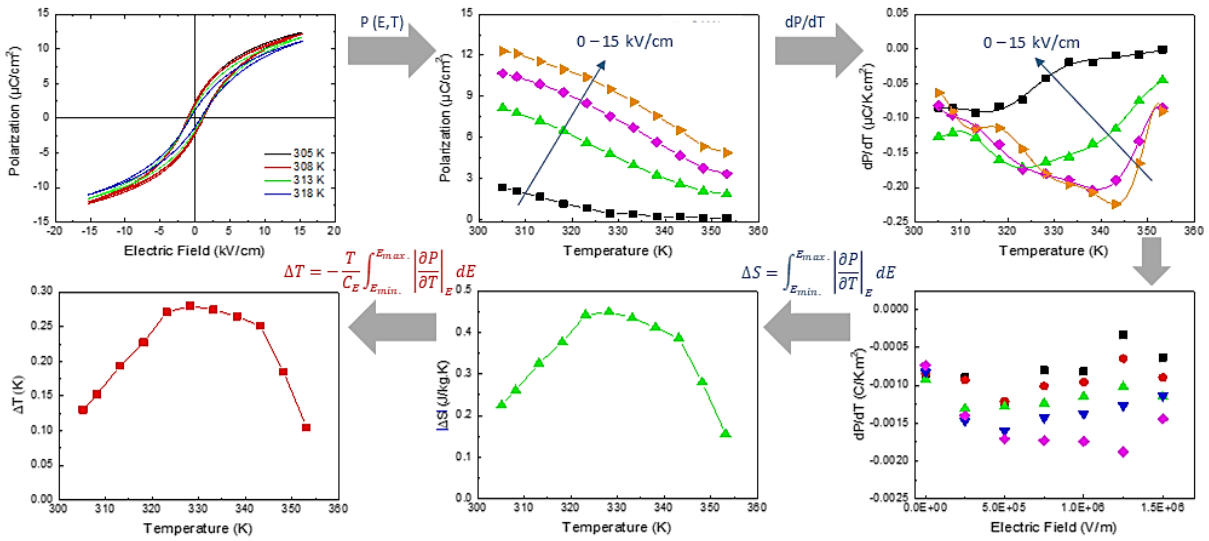

Figure 22 Stepwise explanation of the indirect measurement of the electrocaloric effect. [81]

One issue that is encountered very often is the observation of a "specious" negative or inverse electrocaloric effect. In this work, the term "specious" negative electrocaloric effect is frequently used to represent the negative/inverse electrocaloric effect that is only observed through the indirect method, but not confirmed by the direct measurements [6, 21-22]. In such cases, the negative electrocaloric effect is observed in certain temperature or electric field ranges when unsaturated hysteresis loops are used for the indirect estimation of electrocaloric effect [22]. Another phenomenon that becomes dominant with increasing temperature is the conductivity contribution. Consequently, the hysteresis loops broaden with the temperature and result in related increase of polarization. In such cases, a negative electrocaloric effect may be observed through the indirect method. [32-33] This has been observed, for example, in the ferroelectric polymers, where the indirect method indicated an "inverse" electrocaloric effect, while the direct measurements of the similar compositions showed only a conventional/positive ECE [34-36].

The Maxwell relations have been more often used than the direct measurement methods for the ECE estimation in the reported literature, but their limitations have been in discussion. [20, 21] The Maxwell relation method is valid when the temperature change is relatively small and the system is in thermodynamic equilibrium and in the ergodic state, which means that the system is entirely reversible, and the selection of the thermodynamic path does not play a major role [89]. In the case

of an irreversible system like a relaxor ferroelectric, the applicability of the Maxwell relations is questionable.

2.2.2.2 Landau-Ginzburg-Devonshire (LGD) Theory for Indirect ECE Calculation

It has been widely discussed that in the ferroelectric relaxors which are non-ergodic systems around the freezing temperature, the Maxwell relations may lead to an erroneous estimation of the EC response [21, 90]. Thus, it was considered important to further extend the indirect approach. Pirc et al. presented a theoretical study on the electrocaloric effect in the ferroelectric relaxors where the field-induced phase transition is the main point. [91] They proposed a new model for the estimation of the electrocaloric entropy and the temperature changes, specifically in the ferroelectric relaxors (Equation 21 and 22).

$$\Delta S = -\left(\frac{1}{2}\beta(T+\Delta T)P^2(E,T+\Delta T) - \frac{1}{2}\beta(T)P^2(0,T)\right) \tag{21}$$

$$\Delta T = \frac{T}{2C_E}[\beta(T)P^2(E,T) - \beta(T)P^2(0,T)] \tag{22}$$

Where, C_E represents the phonon part of the specific heat capacity and $a_1(T) \equiv \frac{da}{dT}$ is the temperature derivative of the first coefficient (at P^2) in the Landau expansion of the free energy on polarization powers. For ferroelectrics, a_1 does not depend on temperature, but for relaxors, a_1 is temperature dependent. Its temperature dependence can be, supposedly, obtained by measuring the quasi-static field-cooled linear dielectric susceptibility. [81] However, the exact measurements of a_1 are rather difficult. In the case of a first order phase transition, the *EC* entropy change must be calculated using the Clausius-Clapeyron equation instead of the Maxwell relation. However, for the calculation of the EC entropy change through the Clausius-Clapeyron equation, it is necessary to have the *E-T* phase diagram of the system in the phase transition region.

Merselmiz et al. estimated the EC response of $BaTi_{0.89}Sn_{0.11}O_3$ using both indirect approaches. [92] They showed that $BaTi_{0.89}Sn_{0.11}O_3$ has relaxor characteristics and considered the model proposed by Pirc et al. (Equation 21 and 22). A comparison is shown in Figure 23 between the ΔT_{EC} calculated by the Maxwell relation as well as through the Pirc model. The new model followed the same trend as the Maxwell relation and the estimated ΔT_{EC} values match perfectly in the paraelectric region. Both

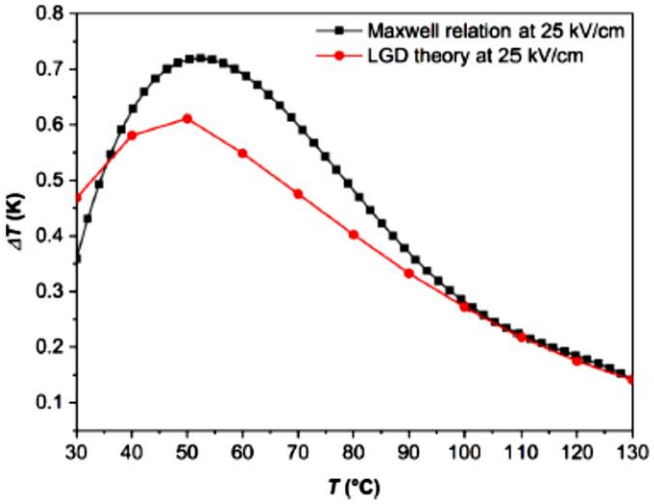

Figure 23 Indirectly measured electrocaloric effect in $BaTi_{0.89}Sn_{0.11}O_3$ through the Maxwell relation and the LGD theory. [92]

approaches show a maximum at the same temperature. However, the maximum ΔT_{EC} calculated through the new model is slightly lower than the one estimated through the Maxwell relations. They attributed this discrepancy to the temperature dependence of the β coefficient.

2.2.3 Insights into the Measurement Methods

2.2.3.1 Correlation of Electric Field & Specific Heat Capacity

As already mentioned, the temperature and electric field dependences of the heat capacity are often neglected while using the indirect method for ΔT_{EC} estimation. This may lead to erroneous results, since the specific heat capacity changes significantly especially in the vicinity of a phase transition. Novak et al. conducted an experimental and theoretical study on the single crystal barium titanate. They discussed the specific heat capacity anomaly related to the paraelectric to ferroelectric phase transition at different electric fields. The values of the heat capacity have been numerically and experimentally calculated at different electric fields (0 kV/cm, 5 kV/cm, 10 kV/cm). The phase transition temperature and heat capacity changed significantly with the applied electric field. [93] In another work, Novak et al. reported the existence of the electric-field-induced critical point for the ferroelectric to paraelectric phase transition in the single crystal barium titanate (Figure 25). The specific heat capacity shows a discontinuous and sharp anomaly at the phase transition temperature, in the absence of an electric field. When an electric field is applied, the phase transition shifts towards slightly higher temperatures. [94] Kukreti et al. studied the electric field dependence of the heat capacity in barium strontium titanate ($Ba_xSr_{1-x}TiO_3$) at different temperatures. Using a Green's function, they showed that the specific heat decreases remarkably as the electric field increases. [95] Marathe et al. conducted a computational study on the electric field dependency of the specific heat capacity. In Figure 24, at 0 kV/cm, there is a pronounced peak at the ferroelectric transition, which is characteristic for a first order phase transition. The phase transition peak of the specific heat shifts to higher temperatures with increasing magnitude of an applied electric field, and becomes smoother, thus suppressing the first-order phase transition. Their computed results also validated the phenomenon and the specific heat capacity decreased significantly with increasing magnitude of the electric field. [69, 96]

Molin et al. reported a comparison for the different direct measurement methods of the ECE in lead magnesium niobate-lead titanate multilayer bulk ceramic, and the specific heat capacity was assumed field independent. The results obtained through the different measurement methods were in good agreement. [97] Sebald et al. measured the ECE in poly (vinylidene fluoride-trifluoroethylene-chlorofluoroethylene) [P(VDF-TrFE-CFE)] using the modified DSC and the infrared

photometry methods. They assumed the heat capacity as being a material constant and assumed it to be independent of temperature and electric field. Their results were in reasonable agreement, and they concluded that the heat capacity of [P(VDF-TrFE-CFE)] is only weakly dependent on the electric field. [86] Lu et al. studied the ECE of P(VDF-TrFE-CFE) and its blend with poly(vinylidene-chlorotrifluoroethylene) to compare the direct and indirect methods. They showed that the electrocaloric temperature change deduced through the Maxwell relation is lower than that directly measured. This was attributed to the non-ergodic or irreversible nature of the relaxor ferroelectric polymer. [98] Sanlialp et al. compared the modified DSC and indirect measurement methods of the electrocaloric temperature change in barium zirconium titanate ($BaZr_xTi_{1-x}O_3$,x=0.12 and 0.20). They observed that the electrocaloric temperature change deduced through the polarization hysteresis curves (indirect methods) is lower than that calculated by Δh measured through the modified DSC (as direct method). [76] From the discussion, it can be concluded that the effect of applied electric field and temperature dependence of heat capacity should be considered.

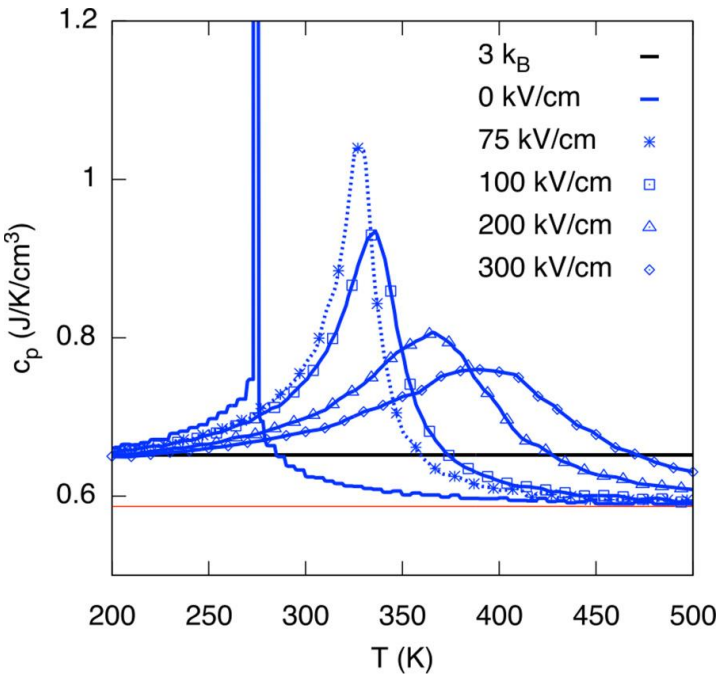

Figure 24 Calculated specific heat capacity of barium titanate as a function of temperature and electric field. [96]

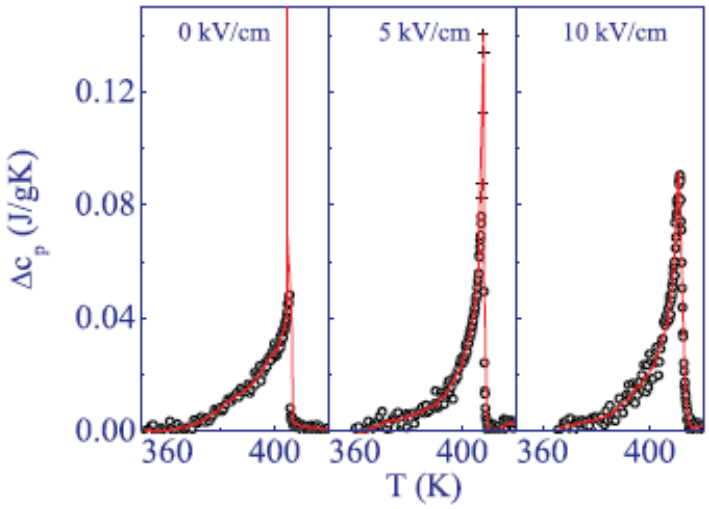

Figure 25 Temperature and electric field dependence of the heat capacity of single crystal barium titanate. [94, 96]

2.2.3.2 Electric Field Related Parameters

The frequency of hysteresis loop measurements may also influence the evaluation of ECE, since the polarization switching in ferroelectric changes with the frequency of the applied electric field. Cheng et al. conducted an experimental study on La-doped $PbZr_{0.49}Ti_{0.51}O_3$ to understand and explain the role of the frequency of the applied electric field on the $P-E$ loops and on the subsequent electrocaloric response estimated through those loops by applying the Maxwell equations. [20] Their work demonstrated that the $P-E$ loops measured at 1 Hz produced reliable electrocaloric temperature and entropy changes and were in close agreement to the directly measured values. While the $P-E$ loops measured at 100 Hz yielded a coexisting positive and negative electrocaloric response attributed to the domain switching mechanism. Their study indicates that the frequency of the electric field is a crucial parameter and the estimated EC values are influenced by the measuring frequency, since the kinetics and dynamics of the domain walls depend on it. Sanlialp et al. measured EC response of different compositions of BZT-BCT through a modified DSC and the indirect method. The $P-E$ loops were measured under *AC* electric field with a frequency of 100 Hz, while the modified DSC measurements were performed under long *DC* field pulse (100 s). They observed a discrepancy between the results obtained through the modified DSC and the indirect method, and attributed it to the absence of the thermodynamic equilibrium and the relatively fast changing electric field which may result in disturbing the isothermal conditions. [75] Bai et al. measured the

EC response of the BTO multilayer thick films using a modified DSC, and varied the rate of the rising electric field, while the rate of the falling field and the intensity were set to 200 kV/cm·s and 500 kV/cm, respectively (Figure 26). [73, 74] They reported that not only the amplitude of the electric field, but also the rate of the applied electric field influences the heat flow peaks. Bai et al. presented a power law relation between ΔQ and the varying rate of the electric field. [74]

As evident from the discussion, it can be concluded that the kinetics (frequency, rate of the field) and the nature (*AC/DC*) of the applied electric field are significant parameters for the EC response, though there is only a limited number of reported works that address the frequency and the form of the field. While comparing the EC response through the direct and the indirect methods, most studies remain focused only on the temperature and the electric field intensity dependency of ΔT_{EC}. [76, 89, 98, 99]

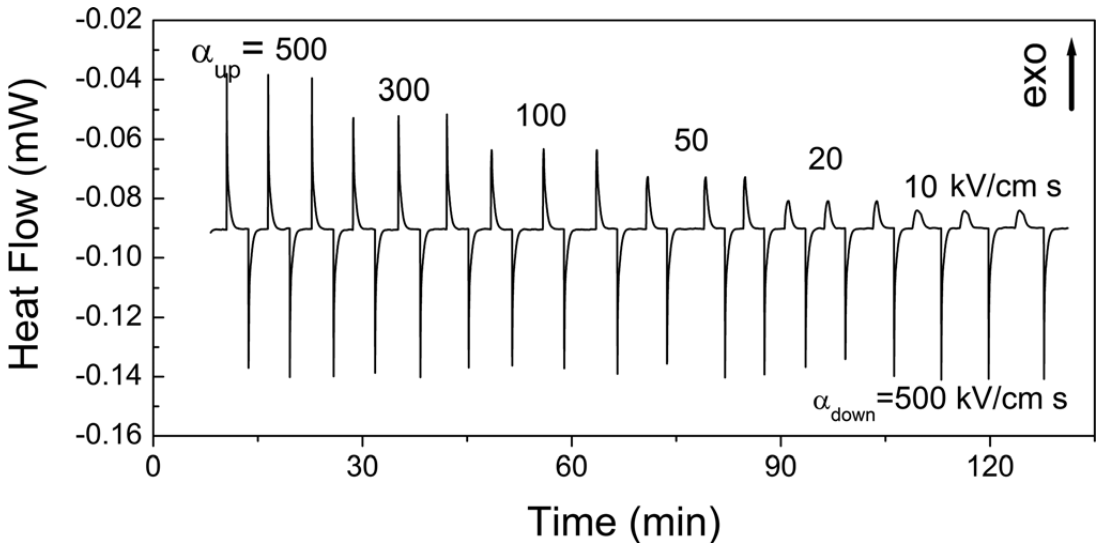

Figure 26 Influence of slew rate on the DSC peak during the electrocaloric measurement. [73]

2.2.3.3 Issue of Joule Heating

Starkov et al. explained the influence of the electric conductivity on the electrocaloric effect. When the electric conductivity is considered, the Maxwell relations for calculating the ECE are not satisfied. They discussed that the current resulting in the Joule heating is directly proportional to the square of the strength of the applied electric field. [100] The electrocaloric effect is also proportional to the

second power of the electric field, but only at its lower values, and as the value of the electric field increases, the exponent value decreases. Hence, it is imperative to decouple the electrocaloric effect and Joule heating especially at high electric fields, where Joule heating can be significant and impairs the reversibility of the ECE. [101] The reversibility of the ECE in the studied sample is indicated by a similar magnitude of the temperature change upon the electric field application or removal. As the field is applied/removed, the temperature relaxes back to equilibrium (base temperature) after a certain duration. The same values of the base temperature upon the electric field application/removal reveal that the contribution of Joule heating due to the leakage current is negligible. When the Joule heating is significant in the sample, this leads to an asymmetry between the relaxation curves for field-on and field-off regimes, and the relaxation curve of field-on regime will relax to a temperature higher than the baseline temperature. Subsequently, the Joule heat contribution can be determined from the difference between the base line temperatures for field-on and field-off relaxation curves as shown in Figure 27. [102–104]

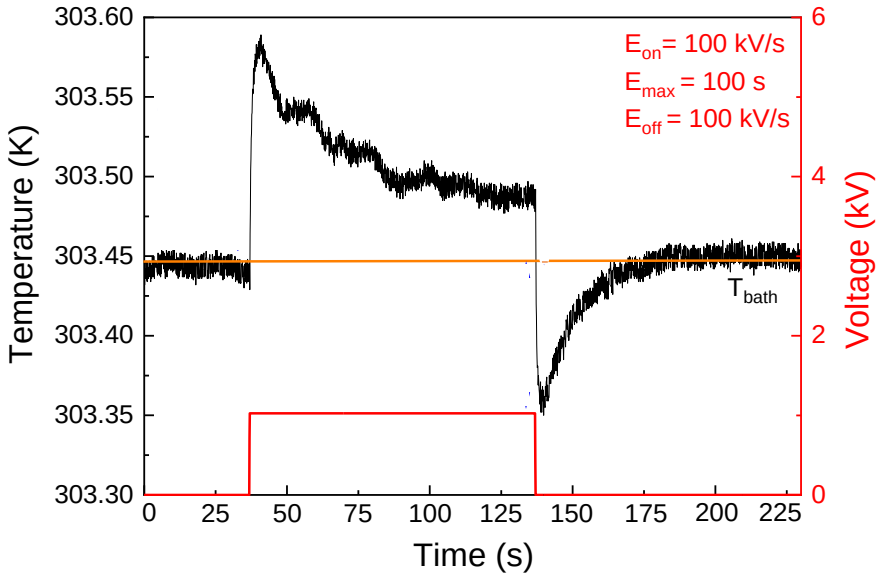

Figure 27 A typical electrocaloric cycle along with Joule heating. (According to [102])

2.2.3.4 Impact of Strain

The Maxwell relations have been derived under certain assumptions. [67, 69] One of those assumptions is that the stress is constant and there is no strain produced in the material.

Nevertheless, a violation of these conditions can occur in experiment, resulting in wrong results by the indirect ECE measurements. Marathe et al. reported that the strain in barium titanate thin film results in a discrepancy between the directly and indirectly measured electrocaloric temperatures changes. [69, 105] In the case of thin films, the effect of stress becomes critical, where the thermal expansion mismatch between the film and substrate, or the volumetric expansion during the phase transition can generate a significant strain mismatch between substrate and film. The influence of stress is not only crucial in the thin films, but also in bulk ceramics. A strong discrepancy between the direct and the indirect EC measurements is shown in uniaxially compressed lead zirconate titanate ceramics. [81] In the case of the free-standing films of soft dielectric materials, such as ferroelectric polymers, the constant stress/strain conditions can be easily violated by temperature change, as well as by application of a high electric field due to electrostriction or attraction of the metal electrodes, which is weak in ceramics but could come into play in polymers. [81]

2.2.4 Materials for Electrocaloric Effect

The quest for the best organic and inorganic dielectric materials exhibiting a substantial electrocaloric effect has been going on. The ideal material system must show a significant electrocaloric strength close to room temperature. The electrocaloric strength $^{\Delta T_{EC}}/_{\Delta E}$ of the material is defined as the ratio between the electrocaloric temperature change in response to the applied electric field. [106] One way to achieve a high electrocaloric strength is to utilize the vicinity of a ferroelectric phase transition, where the entropy and polarization change rapidly due to the transformations occurring in the crystal structure. [107] Broadly speaking, the electrocaloric strength of inorganic dielectrics (ceramics) is better than of organic (polymer) materials. On the other hand, in case of polymers, the dielectric breakdown strength is very high compared to inorganic dielectrics, but a very high amplitude of voltage is required to orient the dipoles of the bulky polymer chains. For inorganic dielectrics such as bulk ceramics, the low dielectric breakdown strength is a problem, where the thickness of the sample plays a major role. [108] According to the classical theory of the dielectric breakdown, the thicker a layer, the higher the potential difference necessary to generate the same field as in a thinner layer. This necessitates a higher charge density on the electrodes. Smaller geometrical defects become more critical in the higher charge density and cause local spots of field singularities. To tackle the issue of the dielectric breakdown strength of bulk ceramics, ceramic thin film, and multi-layer ceramic capacitors (MLCC) are studied for the electrocaloric effect.

The electrocaloric effect has been reported in thick and thin films of organic and inorganic systems which is summarized in Figure 28. The electrocaloric effect in copolymers of P(VDF) and their nanocomposites has been investigated at higher temperature, which is not favorable for electrocaloric cooling or refrigeration devices, that is supposed to operate near room temperature. The thin and thick films of ceramic, that exhibit a large electrocaloric effect at high temperatures, are based on lead compounds which are harmful for the environment. The barium titanate and hafnium based systems have a low electrocaloric coefficients compared to the P(VDF–TrFE–CFE) in the vicinity of room temperature. Therefore, the fluorinated terpolymers P(VDF-TrFE-CFE) and their nanocomposites are appropriate, as they exhibit the electrocaloric effect at room temperature. [1, 4, 109, 110]

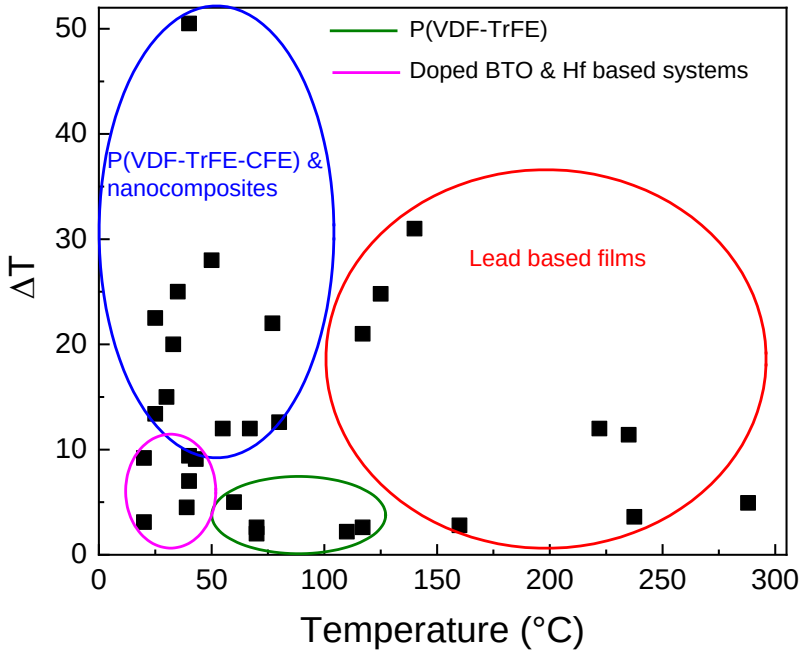

Figure 28 Electrocaloric temperature change in different materials as a function of temperature. (According to [4])

Table 3 enlists the electrocaloric effect in various compositions of P(VDF-TrFE) and P(VDF-TrFE-CFE) measured through different methods. It is clear from Table 3 that in most reported works on the direct measurement of the electrocaloric effect in P(VDF-TrFE-CFE), customized calorimeters are used to measure the electrocaloric enthalpy change under isothermal conditions and the

electrocaloric temperature change is estimated ($\Delta T_{EC} = \Delta Q_{EC}/C_p$) which is denoted by *(e)* and is significantly higher than the values measured through the infrared camera. The direct electrocaloric measurement in P(VDF-TrFE) 70/30 using a quasi-adiabatic calorimeter having a thermocouple as the sensor show a huge difference to the indirect measurement at the same measurement temperature. The directly measured ΔT_{EC} in P(VDF-TrFE) 70/30 is merely 0.12 K, in P(VDF-TrFE) 75/25 is 0.23 K, while it is calculated as 24 K through the indirect method. [111–113]

Table 3 Electrocaloric coefficients in various copolymer & terpolymer compositions through indirect and several direct methods (NA = not available, ρ = density, RT = room temperature, e = estimated via $\Delta T_{EC} = \Delta Q_{EC}/C_p$).

P (VDF_x-$TrFE_{1-x}$) P (VDF_x-$TrFE_y$-CFE_{1-x-y})	ΔT_{EC} (K)	ΔS_{EC} (J/kg·K)	Electric Field Change (MV/m)	Temperature (°C)	Measurement Method	Reference
55/45	12.5	60	209	80	Indirect	[13]
55/45	4	10	50	67	Thermistor	[114]
68/32	2	NA	50	NA	Thermistor	[15]
52/48	- 0.6	NA	60	57	Indirect	[17]
52/48	- 0.5	NA	45	60	Indirect	[18]
68/32 (irradiated)	20	100	160	33	Infrared camera	[115]
70/30 (LB film)	24	NA	300	120	Indirect	[111]
70/30	0.12	NA	20	110	Thermocouple (quasi-adiabatic calorimeter)	[112]
59.2/33.6/7.2	12	55	307	55	Indirect	[13]
59.2/33.6/7.2	15 (e)	NA	150	30	Calorimeter	[14]
59.2/33.6/7.2 (annealed)	4 (e)	20	300	30	Calorimeter	[116]
59.2/33.6/7.2 (quenched)	2 (e)	10	300	30	Calorimeter	[116]
59.2/33.6/7.2	3.6	NA	70	27	Infrared Camera	[115]

59.4/33.4/7.2	22 (e)	275/ρ	175		Calorimeter	[117]
62.3/29.9/7.8	4 (e)	35/ρ	75	40	Calorimeter	[118]
62.5/29/8.5	7.6 (e)	38	140	20	Calorimeter	[119]
62.3/29.9/7.8	15 (e)	130/ρ	150	RT	Calorimeter	[120]
56.2/36.3/7.5 (LB film)	4	NA	100	RT	Indirect	[111]
P (VDF_x-$TrFE_{1-x}$-CFE_y) 69.7/30.3/6	11 (e)	NA	90	20	Calorimeter	[121]
P (VDF_x-$TrFE_{1-x}$-CFE_y) 62.6/29.4/8	5.2	NA	90	RT	Infrared Camera	[85]
NA	2.75	15.1	80	27	Modified DSC & Infrared Camera	[86]
NA	12.5 (e)	NA	150	30	Calorimeter	[62]
NA	18 (e)	175/ ρ	175	30	Calorimeter	[64]
NA (hot pressed)	23 (e)	210/ ρ	175	30	Calorimeter	[64]

As already mentioned, polymers have a high dielectric breakdown strength, while ceramics have good polarizability. Therefore, polymer/ceramic nanocomposites are also interesting for the electrocaloric effect. The introduction of a ceramic nanofiller into the P(VDF-TrFE-CFE) matrix has the advantage of an enhanced polarization due to the large surface area with significant surface charges on the nanofiller/polymer interface and improves the electrocaloric properties at a comparatively low electric field. [122] To achieve a significant electrocaloric effect under a moderate electric field, the polymer nanocomposites with varying amount and different morphologies of nanofiller such as nanoparticles, nanoparticles in nanofibers, nanorods, nanowires, and nanosheets have been studied. [79, 118–120] [122] The electrocaloric property of the nanocomposites has been improved compared to the pure co- and terpolymers. However, the addition of nanofiller decreases the

dielectric breakdown strength of the polymer matrix. Therefore, Zhang et al. used boron nitride nanosheets (BNNs) to improve the dielectric breakdown strength of the polymer/BST nanocomposites. [118] It is clear from Table 4 that except for the indirect measurement, all the reported values of the electrocaloric temperature in nanocomposites of P(VDF-TrFE) and P(VDF-TrFE-CFE) are estimated from the measured isothermal enthalpy change. Another noticeable feature in Table 4 is that the directly measured electrocaloric temperature is positive.

Table 4 Electrocaloric coefficients in terpolymer P(VDF-TrFE-CFE) based nanocomposites containing inorganic ceramic nanofiller (NP = Nanoparticles, NF = Nanofibers, NW = Nanowires, BNN = Boron nitride nanosheet, ρ = density, RT = room temperature, e = estimated via $\Delta T_{EC} = \Delta Q_{EC}/C_p$).

Nanocomposites						
P (VDF_x-$TrFE_y$-CFE_{1-x-y}) – Filler	**ΔT_{EC} (K)**	**ΔS_{EC} (J/kg·K)**	**Electric Field Change (MV/m)**	**Temperature (°C)**	**Measurement Method**	**Reference**
61.3/30.5/8.2 – 5 vol.% $BaZr_{0.2}Ti_{0.8}O_3$ NP	7.4 (e)	30	90	20	Calorimeter	[122, 123]
62.5/29/8.5 – 3 vol.% ZrO_2 NP	9.2 (e)	46	140	20	Calorimeter	[119]
62.3/29.9/7.8 – 10 vol.% $Ba_{0.67}Sr_{0.33}TiO_3$ NP	9 (e)	80/ρ	75	40	Calorimeter	[118]
62.3/29.9/7.8 – 8 vol.% $Ba_{0.67}Sr_{0.33}TiO_3$ – 9 vol.% BNN	50.5 (e)	425/ρ	250	40	Calorimeter	[118]
59.4/33.4/7.2 – 37.5 wt.% 0.9$Pb(Mg_{0.33}Nb_{0.66})O_3-0.1PbTiO_3$ NP	30 (e)	200/ρ	175	RT	Calorimeter	[117]

62.3/29.9/7.8 – 5 vol.% $Ba_{0.67}Sr_{0.33}TiO_3$ NP	23 (e)	200/ρ	150	RT	Calorimeter	[120]
62.3/29.9/7.8 – 10 vol.% $Ba_{0.67}Sr_{0.33}TiO_3$ NW	32 (e)	273/ρ	150	RT	Calorimeter	[120]
N/A – 10 vol.% $BiFeO_3$ NP in $BaZr_{0.21}Ti_{0.79}O_3$ NF	31.4 (e)	300/ρ	150	30	Calorimeter	[79]
N/A – 7.5 vol.% $BaTi_{0.89}Sn_{0.11}O_3$ NP	9.08	79 kJ	100	RT	Indirect Method	[124]

Along with the pure co- and terpolymers and their nanocomposites with ceramic nanofiller, the blends of P(VDF-TrFE) with P(VDF-TrFE-CFE) and P(VDF-CTFE) were also studied for the electrocaloric effect as enlisted in Table 5. [125] [123, 126, 127] Those blends were prepared by simply mixing the respective amount of co- and terpolymer powder in the solvent. The electrocaloric change in blends is comparable to the pure co- and terpolymers.

Table 5 Electrocaloric coefficients in the blends of copolymer P(VDF-TrFE) with terpolymer (PVDF-TrFE-CFE) (NA = Not available, ρ = density, RT = room temperature, e = estimated via $\Delta T_{EC} = \Delta Q_{EC}/C_p$).

Polymer Blends						
P (VDF_x-$TrFE_{1-x}$) – P (VDF_x-$TrFE_y$-CFE_{1-x-y})	ΔT_{EC} (K)	ΔS_{EC} (J/kg·K)	Electric Field Change (MV/m)	Temperature (°C)	Measurement Method	Reference
90 wt. % P(VDF-TrFE) 55/45 – 10 wt.% P(VDF-TrFE-CFE) 62.5/29/8.5	9.5 (e)	90/ρ	150	RT	Calorimeter	[63]
30 vol.% P(VDF-TrFE) 65/35 – 70 vol.% P(VDF-TrFE-CFE) 61.5/30.3/8.2	NA	22	100	RT	Calorimeter	[123]
10 wt.% P(VDF-TrFE) 65/35 – 90 wt.% P(VDF-TrFE-CFE) 59/33/8 (unpoled)	10 (e)	52	100	25	Calorimeter	[128]
10 wt.% P(VDF-TrFE) 65/35 – 90 wt.% P(VDF-TrFE-CFE) 59/33/8 (poled)	12 (e)	63	100	25	Calorimeter	[128]

2.3 Electrical Energy Storage

The trend toward electrification is uprising worldwide. Materials with the electrical energy storage properties have a vital functionality and are an integral part of the consumer electronics, electronic gadgets, standby power systems, electric and hybrid vehicles in the form of storage components such as capacitors, batteries, supercapacitors, and fuel cells. The growing demands for the electrical power and the surge in electrification require advanced materials having high energy and power density, high breakdown strength, high fatigue endurance, thermal stability, light weight, and sustainability. Owing to the rapidly increasing necessity for the electrical energy storage, the quest of new materials with improved properties and new functionalities has also grown which is indicated by the rising number of publications in the field of dielectric capacitors for the energy storage over the past ten years (Figure 29). [129]

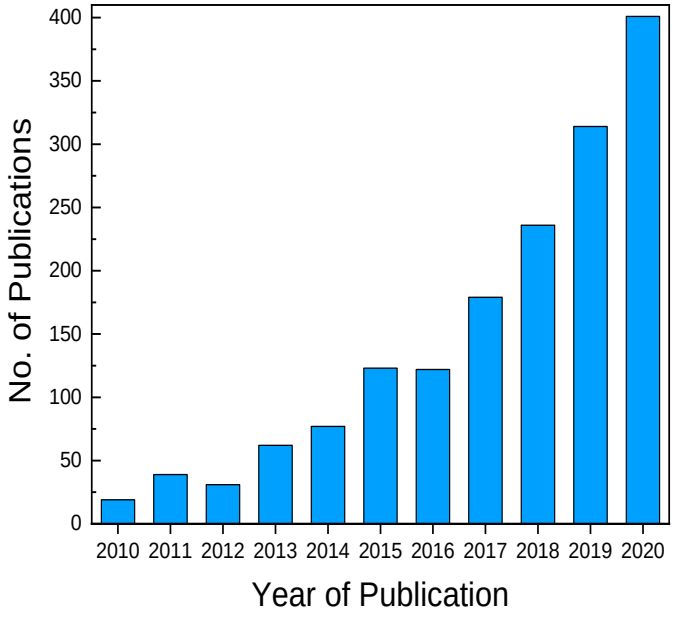

Figure 29 Number of publications on the electrical energy storage in the last decade. ***(Source: Web of Science – July 2021)***

There are two major parameters which are fundamental for the storage devices: the energy density and the power density. The energy density describes the amount of energy that can be stored in a specified volume or weight. While the power density defines the rate at which energy is stored or discharged from the device. The ideal storage device should possess both, high energy density as well as high power density. The capacitors store the electrical energy in the form of electric charges,

which are accumulated when a capacitor is connected to a power source. While a battery uses electrochemical processes to store and discharge energy, which need longer time to take place. Therefore, the capacitors are capable to release the stored energy much faster than the batteries. As depicted in Figure 30, the power densities of dielectric capacitors are high compared to the other electrical storage devices, such as batteries, and electrochemical capacitors, which make them favorable candidates in pulsed systems. However, the energy densities of conventional capacitors are usually too low to be acceptable for storing large amount of energy. Therefore, the integration of conventional energy storage units (e.g., batteries and fuel cells) and the electric energy storage devices in the high-power or pulse-power forms (e.g., capacitors) is the prime concern in the development of the new power systems. Thus, the dielectric capacitors having high power density are widely investigated to improve their energy densities and thermal stability and to minimize their electrical losses. [129, 130]

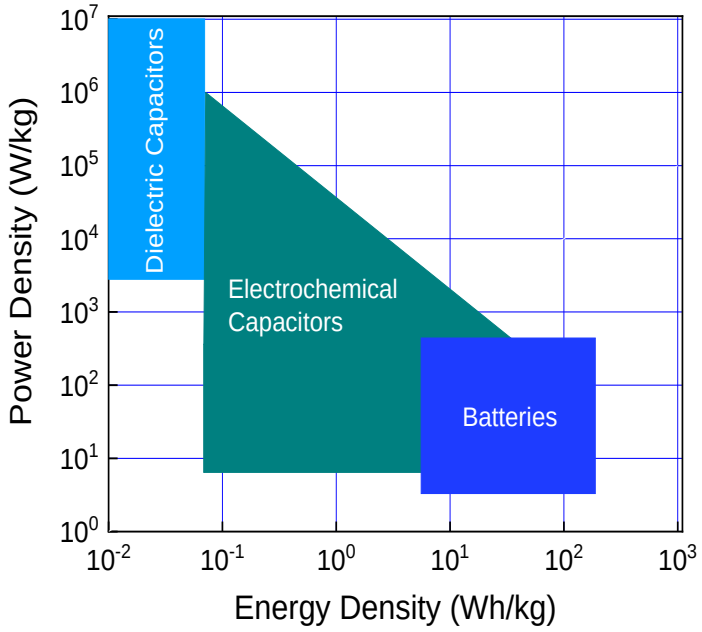

Figure 30 Energy density and power density of different material classes. (According to [131])

2.3.1 Dielectric Polymers for Electrical Energy Storage

Dielectric materials can be categorized into organic (polymers) and inorganic (ceramic) materials. Inorganic dielectrics offer the advantage of having a high dielectric constant or permittivity (>1000). However, their breakdown strength is very low. Whereas, polymeric dielectrics have high breakdown strength, that enables a reliable operation and a higher capacitance stability. [131] Capacitors made of polymer films as dielectric materials, are preferably used on off-shore platforms, as they exhibit an excellent self-healing behavior and a low production and maintenance cost. [132] Due to their high dielectric strength and light-weight, various dielectric polymers such as polypropylene, polycarbonate, and polyethylene terephthalate have been commercially used in thin film and thick film capacitors for decades. Dielectric polymers, for example polypropylene, do not only exhibit very high dielectric strength and lowest dielectric loss, but also provide easy manufacturing i.e. cost-effective and easy processing. However, most of the dielectric polymers have a low dielectric constant (< 10), low operating temperature, and low volumetric energy density compared to ceramics. The commercially available polymer-based film capacitors are primarily made of biaxially oriented polypropylene (BOPP). However, the dielectric permittivity of BOPP is very low (~ 2.2), consequently it has a low energy density of about $2\,J/cm^3$. Polyesters, like Polyethylene terephthalate (PET), are capable of storing more energy per volume, but they have higher dissipation factors which cause more heat production. Thus, the key factors to improve the performance of polymeric capacitors are: Increasing both the permittivity as well as the dielectric breakdown strength, and increasing the energy density without increasing the power losses. Among all dielectric polymers, P(VDF) offers several advantages such as a relatively high permittivity (> 10), and the cost-effective extrusion into large-scale film with a high mechanical flexibility (>15% elongation), but its high dielectric losses limit its usability. [129, 132–135]

2.3.2 Electrical Energy Storage in P(VDF–TrFE–CFE) & Their Nanocomposites

Nonlinear dielectric polymers, such as P(VDF), show a significant hysteresis loop and a large remnant polarization, owing to their ferroelectric nature. This is possible by the copolymerization of P(VDF) with hexafluoropropoylene (HFP) and chlorotrifluoroethylene (CTFE). [136] The blends of P(VDF) with P(VDF-HFP) have been examined as well. When VDF is copolymerized with trifluoroethylene (TrFE) and chlorofluoroethylene (CFE), the resulting terpolymer P(VDF-TrFE-CFE) possesses ferroelectric relaxor behavior with a very low remnant polarization and therefore low losses, and a

high discharge energy density. [137, 138] Several efforts have been made to improve the energy storage properties, by adding inorganic 0D (nanoparticles), 1D (nanowires, nanofibers), and 2D nanofillers (nanosheets, nanoflakes), mainly in P(VDF), but also in P(VDF–TrFE) and P(VDF–HFP). Inorganic non-conductive fillers such as barium titanate, doped and surface functionalized barium titanate, oxides of zinc and titanium, and conductive nanofiller such as carbon nanotubes (CNTs), graphene oxide, carbon black, and metallic (nickel) nanofillers have been reported. [49, 139–145] The dielectric permittivities of nanofillers as well as of the host polymer matrix have an influence on the breakdown strength of the nanocomposites. The dielectric properties of the nanocomposites depend on the physical properties of the nanofillers (permittivity, electrical conductivity, and band gap), their morphology and microstructure (filler shape, volume fraction, distribution, and orientation), and the nanofiller−matrix interface characteristics. [146] The interfaces formed between the nanofillers and the host polymer matrix can significantly affect the dielectric properties of the nanocomposites. [147, 148]

There are two models that explain the interface formed between a spherical nanoparticle and the host polymer matrix, namely Tanaka's model and Lewis' model. Tanaka's model divides the interface into three layers, all of which are bonded layers. The outermost layer, called the transition layer, is strongly bonded to both the inorganic and organic layers, and has a thickness of about 1 nm. The second layer mainly depends on the interaction between the nanofillers and the polymer matrix, and has a thickness of 2 – 9 nm. The polymer chains in the second layer are strongly bound to the first layer depending on its interaction with the nanofiller. The third layer is a loosely bound layer having a thickness of several nanometers, and is coupled to the second layer. The chain mobility, chain conformation, crystallinity, and free volume of the bulk polymer matrix are different on the polymer–nanofiller interface. [49, 130]

Another model to describe the nanoparticle–polymer interface is Lewis' model. This model is based on the accumulation of charges on the nanofillers. This charge accumulation occurs due to the difference of the Fermi levels between the nanoparticles and the polymer matrix. Consequently, the host polymer matrix forms counter charges in the vicinity of the surface of the nanofillers. Due to the Coulomb attraction, the charged nanoparticle surfaces will induce a charge redistribution within the polymer matrix. This redistribution of charges will result in the formation of an electrical double layer, consisting of Gouy–Chapman diffused layer, and the Stern layer. This double layer significantly

influences the dielectric properties of polymer nanocomposites. Under an externally applied electric field, the nanoparticles act like large dipoles, as the charge carriers move along the interface, owing to their higher mobility compared to the host polymer matrix. This causes a polarization of the interface around the nanoparticles, and results in an increase in the effective permittivity of the nanocomposite, which exceeds the permittivity value calculated with the mixing rule. However, the losses can also increase in this case, because of the formation of a diffuse cloud of charge carriers around the nanoparticles, which oscillates out of phase at low frequency of applied electric field. [49, 130]

As mentioned before, most of the reports on P(VDF) based systems focus on P(VDF), P(VDF–TrFE–CFE), and P(VDF–HFP) and their nanocomposites. It is very often that only the dielectric properties are examined, but the energy density of the investigated systems is not discussed. In this work, the electrical energy storage of P(VDF–TrFE–CFE) and its nanocomposites with 0D ceramic nanofiller along with their dielectric properties are examined. Reported values of the electrical energy storage characteristics of different compositions of P(VDF–TrFE–CFE) and its nanocomposites with conductive and non–conductive nanofillers are summarized in Table 6.

Table 6 Electrical energy storage characteristics of P(VDF-TrFE-CFE) & its nanocomposites at room temperature (HZ = hydrazine hydrate, BTO = barium titanate, NW = nanowires).

$P(VDF_x\text{-}TrFE_{1-x}\text{-}CFE_y)$	Dielectric Constant (1 kHz)	Loss Tangent (1 kHz)	Electric Field (MV m^{-1})	Discharged Energy Density ($U_{discharged}$) (J cm^{-3})	Reference
64/36/7.2	NA	NA	100	1.8	[149]
70/30/8.1	NA	NA	100	2	[149]
63/37/8.1	NA	NA	200	3.8	[150]
P(VDF–TrFE–CFE) / 1.7 vol.% HZ RGO	> 10000	2.52	NA	NA	[141]
P(VDF–TrFE–CFE) / 17.5 vol.% BTO NW	NA	NA	75	1.6	[143]

2.3.3 Measurement Methods of Energy Density

The electrical energy storage properties, such as stored and discharged energy density, are measured through the following three methods, namely, polarization-based, direct charge-discharge and indirectly calculated (Figure 31). All these three methods will be explained in detail in the following sections.

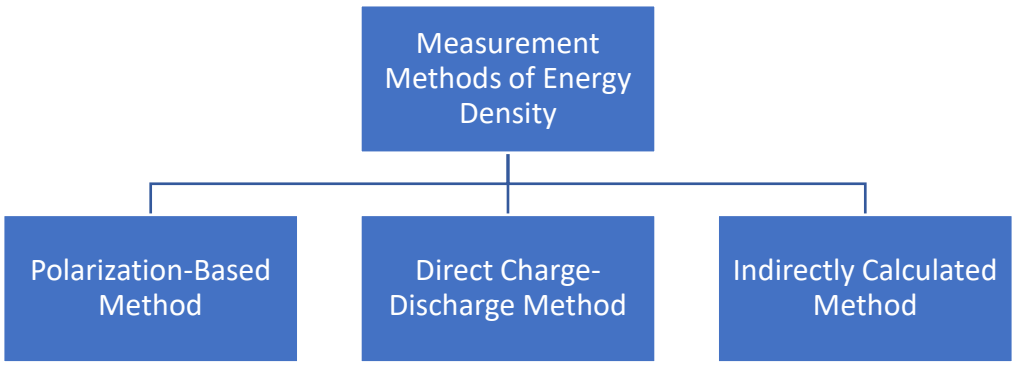

Figure 31 The measurement methods of the electrical energy storage characteristics.

2.3.3.1 Polarization-Based Method

The practical applications of energy storage are based on charging the dielectric capacitor under a *DC* voltage followed by the discharge to a load. This charge-discharge process can be realized under a unipolar electric field, to estimate the energy density of any dielectric material. In this method, the stored energy density of the dielectrics can be obtained by integrating the area between the *charging* branch of the *D – E* loop and the dielectric displacement axis. The electric displacement *D* of a dielectric having high permittivity, is very close to their electrical polarization *P,* according to the relation $D = \varepsilon_o E + P$. As shown in Figure 32, the polarization increases to its maximum P_{max}, as the electric field increases from zero to the maximum E_{max}. Subsequently, the electrical energy with a density (U_{stored}) is charged (stored) in the dielectric, which is represented by the total area of green and shaded region in Figure 32, and can be written as,

$$U_{stored} = \int_0^{P_{max}} \vec{E}\,(\vec{P})_{charge} \cdot d\vec{P} \qquad (23)$$

As the electric field declines from E_{max} to zero, the polarization also drops from P_{max} to P_{rem}. As a result, a part of the charged or stored energy (U_{stored}), that is known as the recoverable electrical energy density ($U_{discharged}$), is then discharged, portrayed by the green area in Figure 32 and is given by,

$$U_{discharged} = \int_{P_{rem}}^{P_{max}} \vec{E}\,(\vec{P})_{discharge} \cdot d\vec{P} \tag{24}$$

As evident in Figure 32, the charged and discharged energies are not the same, and a part of the charged electrical energy has been lost. This lost energy (U_{loss}), which is dispersed during the *charge–discharge* process is indicated by the shaded area, enclosed by the *charge* and *discharge loops*, and can be given by Equation 25. [130, 135, 151]

$$U_{loss} = U_{stored} - U_{discharged} \tag{25}$$

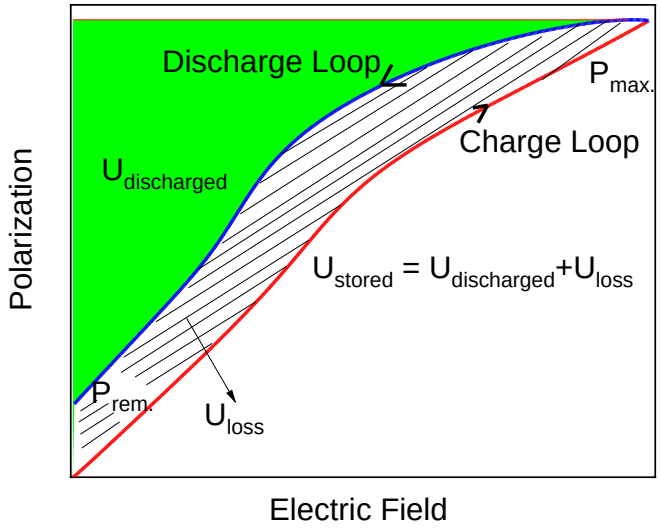

Figure 32 Polarization method for the estimation of the stored energy density, discharged energy density, and losses.

Thus, the charge-discharge efficiency *(η)* is estimated by the ratio between the discharged ($U_{discharged}$) and the stored (U_{stored}) electrical energy densities, as given in Equation 26. [152]

$$\eta = \frac{U_{discharged}}{U_{stored}} = \frac{U_{discharged}}{U_{discharged} + U_{loss}} \quad (26)$$

It can be summarized from the Equation 26, that a large energy density as well as a high energy efficiency can be achieved in dielectrics having a large difference between P_{max} and P_{rem}, and a high breakdown strength (BDS). This indicates that dielectrics with a high breakdown strength, such as ferroelectric polymers and glass-ceramic ferroelectrics, paraelectrics, relaxor ferroelectrics having a large $P_{max} - P_{rem}$, and antiferroelectric (AFE) materials with negligible P_{rem}, are most attractive for electrical energy storage applications, which is also clear from Figure 33. [130]

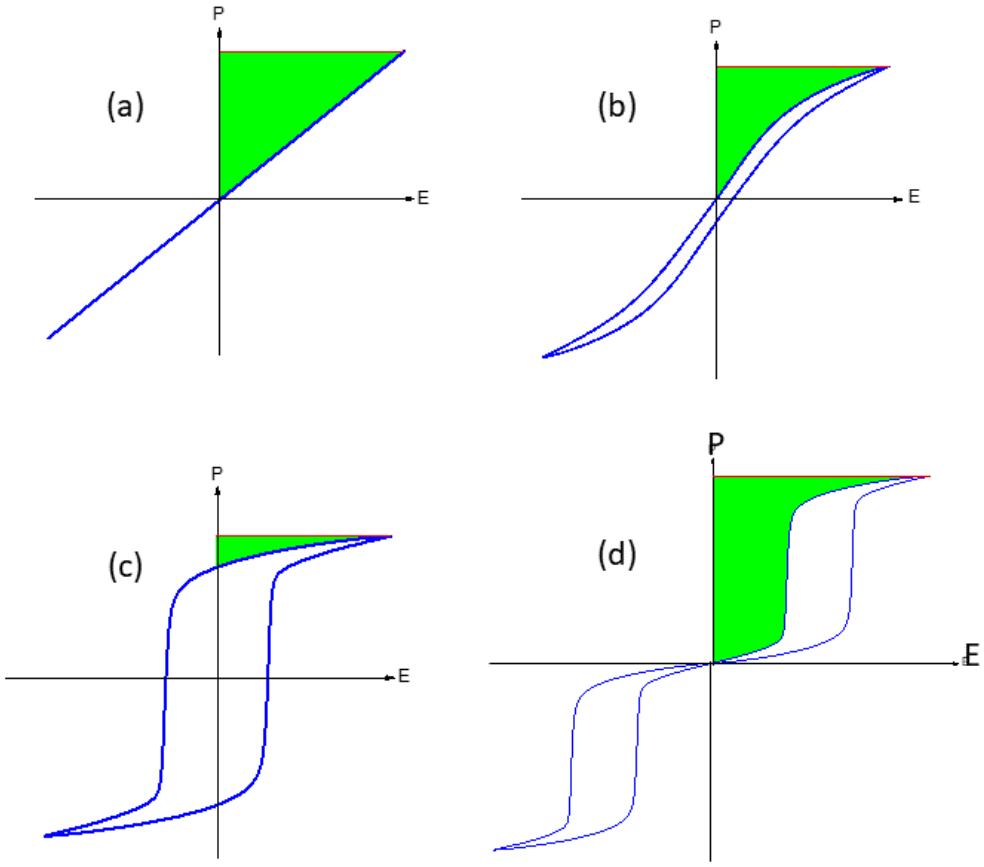

Figure 33 Discharged energy density in (a) paraelectric, (b) relaxor, (c) ferroelectric, and (d) anti-ferroelectric materials. (According to [131])

The $P-E$ loop-based method is a straight-forward method to estimate the energy density of the material. This method does not require any special setup apart from the Sawyer-Tower circuit, which

can be easily realized. Hence, this method is a widely used method to study the energy-storage properties. [130]

2.3.3.2 Direct Charge-Discharge Method

A customized circuit has been reported to measure the real discharged energy density as well as the discharge time of the dielectrics. In this customized circuit, the sample capacitor is first charged by an external electric field, and the electric energy is stored in the dielectric. The charged capacitor is then connected to a load (R) by a switch, to form a discharge circuit (LCR). The inductance (monitor coil) is connected with a resistor (of known resistance) and oscilloscope. Subsequently, a part of the stored energy is discharged, and a transient current is formed in the closed circuit, which is monitored by the oscilloscope. An $I(t)-t$ curve is recorded, and the recoverable energy density $(U_{discharged})$ is calculated by Equation 27.

$$U_{discharged} = \frac{R}{A \cdot d} \int I^2(t) dt \tag{27}$$

Where, R is the resistance of the load, t is the discharge time, and $A \cdot d$ is the volume of the capacitor. The major benefit of this method is that the discharge time of the capacitor in the circuit can be directly determined from the $I(t)-t$ curve, which is useful for the investigation of pulsed dielectric capacitors. The *discharge time (T)* of a capacitor in a specific circuit can be mathematically written as,

$$T = \frac{2\pi}{\omega} = \frac{2\pi}{\sqrt{\frac{1}{LC} - \left(\frac{R}{2L}\right)^2}} \tag{28}$$

According to Equation 28, the *discharge time* (T) is determined by the load (R), inductance (L), and capacitance (C) in the circuit. When the values of R and L are constant, the discharge time is only dependent on C. Thus, for the nonlinear dielectrics, the discharge time can be electric field dependent, while for the linear dielectrics, the discharge time is linear.

The power density (P) can also be estimated through this method by employing the $U_{discharged}$ and discharge time (T). The power density (P) is defined as the energy released per second per volume and is mathematically written as Equation 29.

$$P = \frac{dU}{A \cdot d\ dt} \tag{29}$$

Thus, the power density can be calculated using Equation 30. [130]

$$P = V(t) \cdot I(t) \tag{30}$$

2.3.3.3 Indirectly Calculated Method

For dielectrics, which have an electric-field-independent dielectric constant (linear dielectrics), such as glass, metal oxides, and glass-ceramics, the stored energy density can be estimated by measuring their dielectric constant according to Equation 31. [130, 152]

$$U_{stored} = \frac{1}{2}\varepsilon_0 \varepsilon_r E^2 \tag{31}$$

Where, ε_0 is the permittivity of the free space, and ε_r is the relative permittivity of the dielectric. The maximum stored energy density can be calculated by determining the BDS value. Despite being a simple and quick method, the indirect calculated method has its limitations. This method is only applicable for the rough estimation of the stored energy density (U_{stored}) for linear dielectrics. The recoverable and the loss energy density cannot be determined by this method. Additionally, the dielectric constant is field and temperature dependent, and its variation is difficult to prevent at high electric fields, which may lead to an erroneous result. Therefore, this method is rarely used. [130]

3 Materials & Methodology

The main materials studied in this work are the copolymer and terpolymer of P(VDF), namely, P(VDF-TrFE) and P(VDF-TrFE-CFE).

3.1 Experimental Details

The copolymer P(VDF-TrFE) and terpolymer P(VDF-TrFE-CFE) were bought in powder form from *Piezotech (France)*. The respective amount of constituting monomers in each composition is enlisted in Table 7. For the sake of comparison between P(VDF-TrFE) and P(VDF-TrFE-CFE), the molar amount in P(VDF_x-$TrFE_{1-x}$-CFE_y) is written in VDF + TrFE = 100 format.

The terpolymer is usually synthesized through the suspension polymerization method. The synthesis is carried out in a stainless-steel reaction vessel *(Parr)*. Potassium peroxodisulfate is used as an initiator and introduced into the reaction vessel along with deionized water. The reaction vessel is then sealed and degassed using a vacuum pump. Liquid nitrogen is used to cool the reaction vessel. The gaseous vinylidenefluoride (VDF), trifluoroethylene (TrFE) and chlorofluoroethylene (CFE) are used as precursors. Each precursor gas enters the reaction vessel separately at an individual flow rate. The vessel is then heated to 90°C for the reaction to occur. After the completion of the reaction, the synthesized polymer is obtained in powder form. The powder is then washed using deionized water and ethanol by vacuum filtration to get rid of any impurities or traces of the initiator. Subsequently, the washed powder is dried at 90°C for 24 h. [56]

Table 7 The molar content of each component in the studied P(VDF-TrFE) & P(VDF_x-$TrFE_{1-x}$-CFE_y) compositions. The molar contents of P(VDF-TrFE-CFE) are mentioned in a way that the amount of VDF and TrFE adds up to 100.

Co-polymer & Terpolymer	Composition		
	Vinylidenefluoride [VDF (mol. %)]	Trifluoroethylene [TrFE (mol. %)]	Chlorofluoroethylene [CFE (mol. %)]
P(VDF – TrFE)	70	30	-
P(VDF_x-$TrFE_{1-x}$-CFE_y)	51.3	48.7	6.2
	63.8	36.2	7.2
	59.8	40.2	7.3
	70	30	8.1
	68	32	8.5
	64.8	35.2	7.8

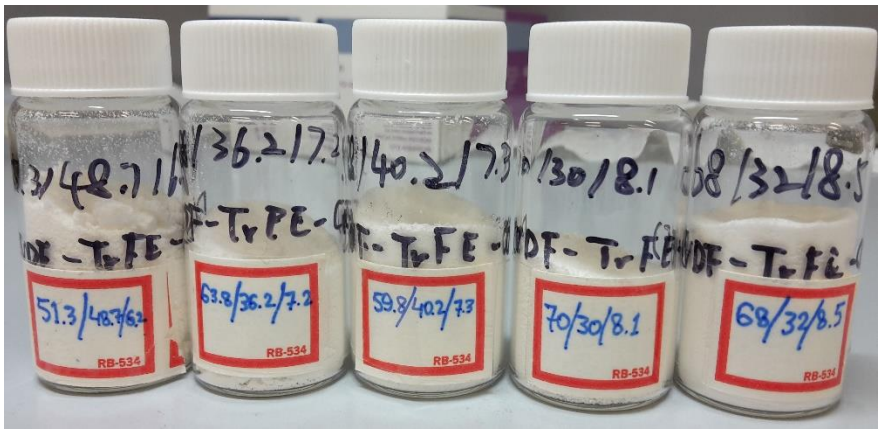

Figure 34 Powder sample of five different compositions of P(VDF–TrFE–CFE).

3.1.1 Polymer Film Fabrication

The free-standing polymer film is prepared by the solution casting method (Figure 35). The polymer powder is dissolved in dimethyl formamide (DMF) *(VWR Chemicals,)* and stirred overnight at room temperature. The concentration of the polymer solution is set to 20 g/L. The polymer solution is then deposited on the glass substrate *(Corning Inc.)* via the filtered drop coating. The sample is dried at 60°C in an oven for ~ 20 h. After drying, the sample is annealed at 100°C under vacuum for 8 h, and cooled down slowly to room temperature. The sample with the substrate is immersed in water

for some time, and a free-standing film is obtained. The final thickness of the free-standing film is ~ 20 µm.

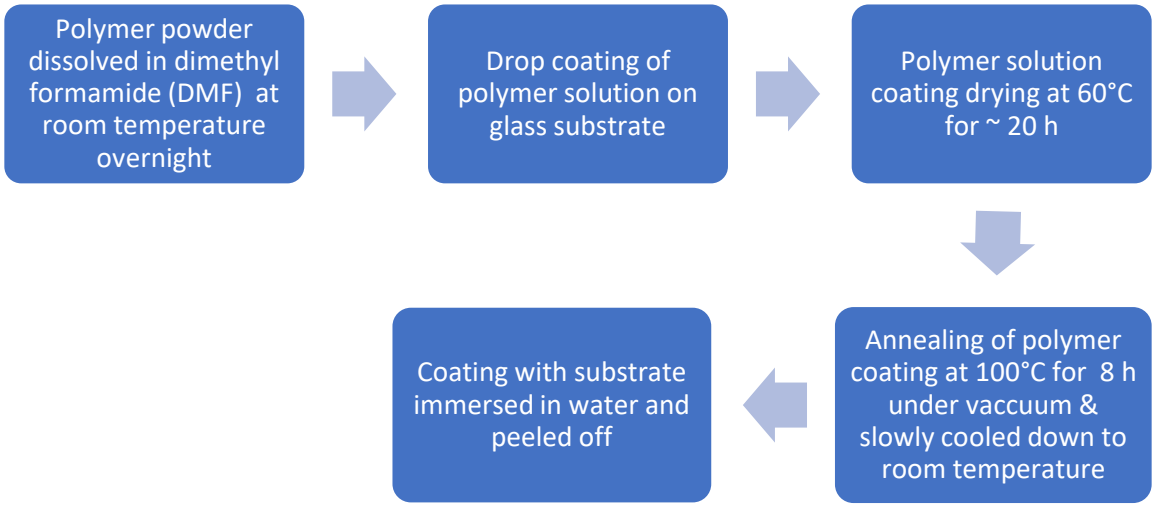

Figure 35 Summarizing the fabrication steps of the free-standing polymer film.

3.1.2 Synthesis of $BaZr_{0.2}Ti_{0.8}O_3$ Nanoparticles via Hydrothermal Method

The hydrothermal method is a standard synthesis route for nanomaterials. The hydrothermal process involves the mixing of precursors and other reagents into a solvent, which is primarily water. Hence, the process is called hydrothermal. If the solvent is anything else other than water, the process is known as solvothermal. The mixed precursors are then transferred into a sealed autoclave made of stainless steel, which is lined with *Teflon*. The precursor mixture is then heated in the autoclave at a certain temperature with a pre-defined heating rate for a specific time, and autogenous pressure. The pressure in the autoclave rises with temperature.

3.1.2.1 Mixing of Precursors

The zirconium doped barium titanate ($BaZr_{0.2}Ti_{0.8}O_3$) nanoparticles are synthesized in the autoclave through the hydrothermal method (Figure 36). The relative amount of dopant, that is zirconium, is chosen as 20 mol% to match the Curie temperatures of BZT and P(VDF-TrFE-CFE). The precursors are barium hydroxide octahydrate ($Ba(OH)_2{\cdot}8H_2O$) (solid) *(Fluka™)*, solution of titanium isopropoxide

($Ti(OCH(CH_3)_2)_4$) *(Sigma-Aldrich)* and zirconium butoxide ($Zr(OC_4H_9)_4$) *(Sigma-Aldrich)*. The respective volumes of titanium isopropoxide and zirconium butoxide are added to 10 mL of absolute ethanol (Figure 36). The solution is stirred for 1 h in a water bath, and the temperature of the water bath is set to 70°C. The calculated amount of barium hydroxide octahydrate is added to the 20 mL of pre-heated deionized water, and stirred at 90°C for 1 h. 5 mL of ammonia solution is then added to the titanium/zirconium/ethanol solution, and the resulting suspension is subsequently added to the barium/water solution, and stirred for another hour. The mixture is then transferred to the reaction vessel of the autoclave chamber. [112, 153, 154]

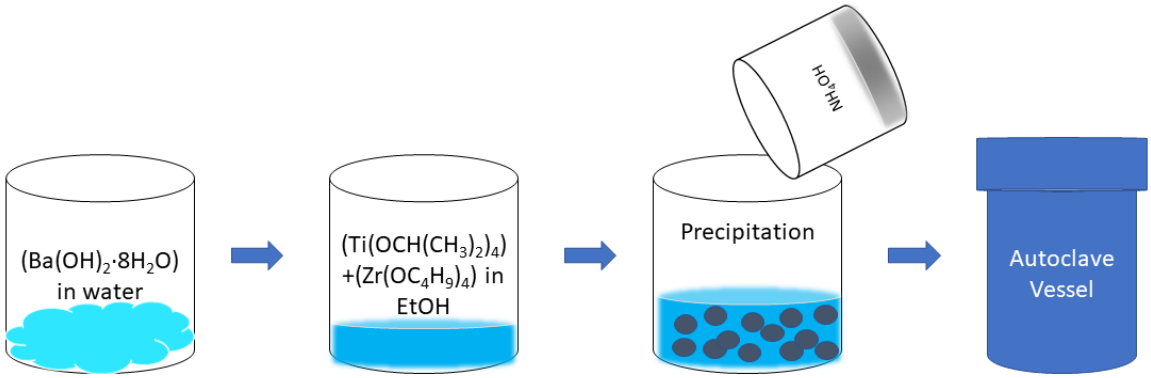

Figure 36 Stepwise synthesis of zirconium doped barium titanate nanoparticles (BZT) through hydrothermal method.

3.1.2.2 Reaction Mechanism

The reaction vessel is made of polytetrafluoroethylene (PTFE). The vessel is sealed, and argon purging is carried out. The temperature of the autoclave (Figure 37) is set to 200°C, and the reaction is carried out for 24 h. During the hydrothermal treatment in the autoclave, the temperature gradient in the (autoclave) vessel changes the solubility of the precursors in the solvent, and leads to the crystallization of the nanoparticles. [112, 153, 154]

Figure 37 Autoclave used for the hydrothermal synthesis of BZT nanoparticles.

3.1.2.3 Post-Processing Steps

The obtained product is in the form of particles, which are then washed repeatedly with a 1:1 solution of water and ethanol, to remove the residual precursors by centrifuging. The centrifugation step is performed using a *UNIVERSAL 320 R (Hettich)* device, equipped with *1620A* rotor. The centrifugation speed is set to 9000 rpm, and the centrifugation duration is 5 min, to separate the nanoparticles from the suspension. The separation process in the centrifuge works on the principle of Stokes' law, which is given by,

$$v = \frac{d^2(\rho_p - \rho_f) \cdot g}{18\,\eta} \tag{32}$$

Where, v is the sedimentation velocity of a spherical particle, d is the diameter of the particle, ρ_p is the density of the particle, ρ_f is the density of the fluid (medium), g is the gravitational acceleration, and η is the viscosity of the fluid (medium).

The supernatant is carefully extracted from the centrifuged sample to obtain the sedimented nanoparticles.

Additionally, the particles are washed, and centrifuged with a 5 vol.% solution of acetic acid (CH_3COOH) and water, to remove the other impurities formed as by-products during the reaction. Finally, the washed nanoparticles are dried at 90°C overnight.

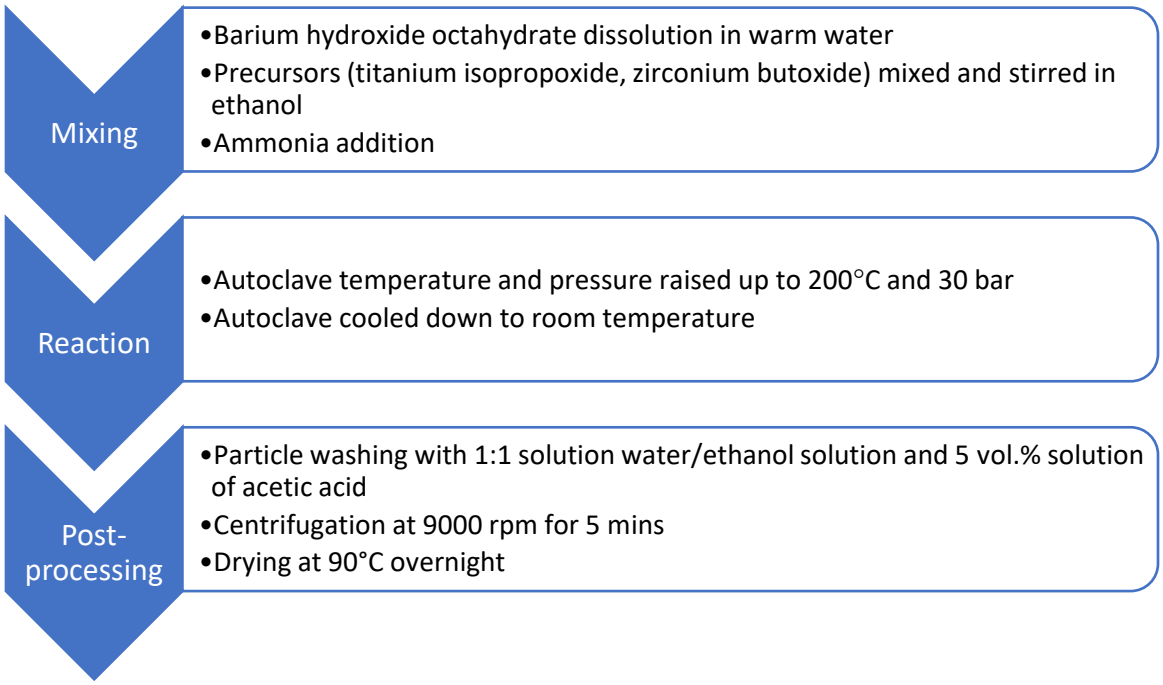

Figure 38 Summarizing the processing and post-processing steps involved in the hydrothermal synthesis of nanoparticles.

3.1.3 Nanocomposite Film Fabrication

The nanocomposite films of $BaZr_{0.2}Ti_{0.8}O_3$ nanoparticles/P(VDF-TrFE-CFE) are fabricated, and the volume of nanoparticles is varied. The amount of BZT nanoparticles is 1.25 vol.%, 2.5 vol.%, and 5 vol.%. The calculated amount of the $BaZr_{0.2}Ti_{0.8}O_3$ nanoparticles, equivalent to the target volume, is added to the polymer solution, and the suspension is stirred for ~ 2 h at room temperature. The remaining procedure and parameters are the same as the (neat) polymer film fabrication, and has been explained in Section 3.1.1. The free-standing nanocomposite film fabrication process is shown step-by-step in Figure 39.

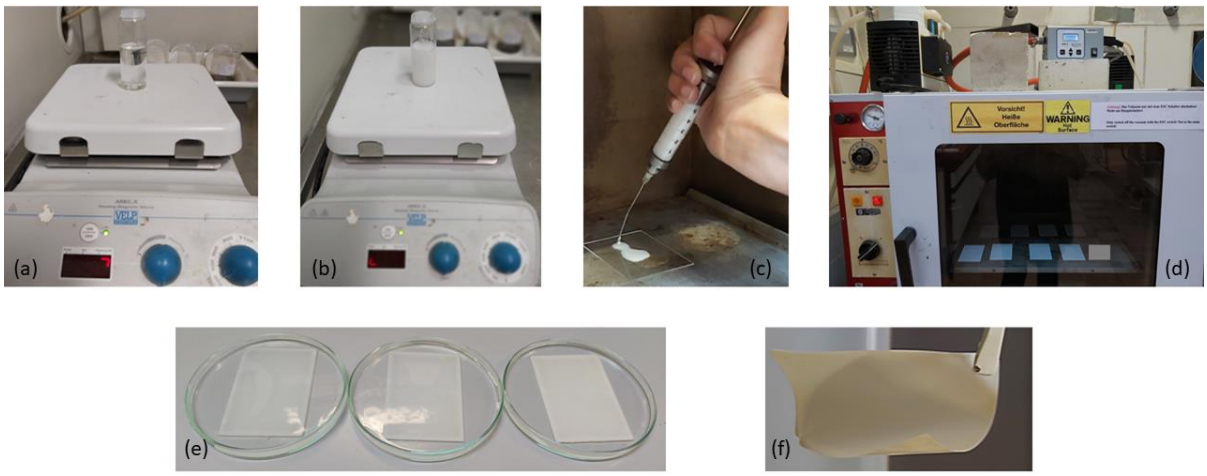

Figure 39 Steps involved in the preparation of free-standing polymer nanocomposite films, dissolution of polymer powder in DMF (a), nanoparticles stirred in polymer solution (b), polymer/nanoparticle suspension drop coated on the glass substrate (c), drying and annealing (d), films immersed with glass substrate in water (e), free-standing polymer nanocomposite film (f).

3.1.4 Electrode Deposition via Sputtering

Electrodes are deposited on the free-standing films via sputtering, which is a physical vapor deposition (PVD) method. The argon (Ar) gas is used as the sputtering gas, while a silver target is used as the material for electrodes. The argon ions hit the silver target, and silver atoms are ejected, which are then deposited on the substrate (sample) to form an electrode layer. The free-standing films are sputtered using a *Cressington sputter coater 208 HR* (Figure 40). The current is set to 60 mA, and the sputtering duration is 100 s. The approximate thickness of the sputtered silver layer is 50 nm, while the diameter is either 4 mm or 5 mm using an appropriate mask.

Figure 40 Sputter coater setup for electrode deposition.

3.2 Characterization Methods

3.2.1 Dielectric Spectroscopy

Dielectric spectroscopy, also known as the impedance spectroscopy, is frequently used to study the response of a material under an applied electric field of constant or varying frequency. Dielectric spectroscopy explains the dielectric properties of a material as a function of the frequency. A broad frequency range of the electromagnetic spectrum is utilized to interact with the materials on molecular, atomic, and sub-atomic level. A material may possess several dielectric mechanisms or polarization mechanisms (such as ionic, orientational, atomic, and electronic), that contribute to its overall dielectric permittivity at different frequencies, as shown in Figure 41. Dielectric materials possess electric charges that can be displaced by an externally applied electric field. Under an applied electric field, the positive and negative charges in a material move in opposite directions. The dielectric permittivity describes the interaction of a material with an electric field. This is a complex quantity with a real part and an imaginary part. The real part of the complex permittivity, which is the dielectric constant *(ε')* of the material, is a measure of the amount of energy stored in the material under an external electrical field. While the imaginary part (ε") is a measure of the amount of energy dissipated from the material due to an external electric field. Its value is always greater than zero, and includes the effects of both dielectric loss and conductivity. The ratio of the imaginary part to the real part of the complex permittivity yields the dielectric loss tangent (tan δ) or the dissipation factor.

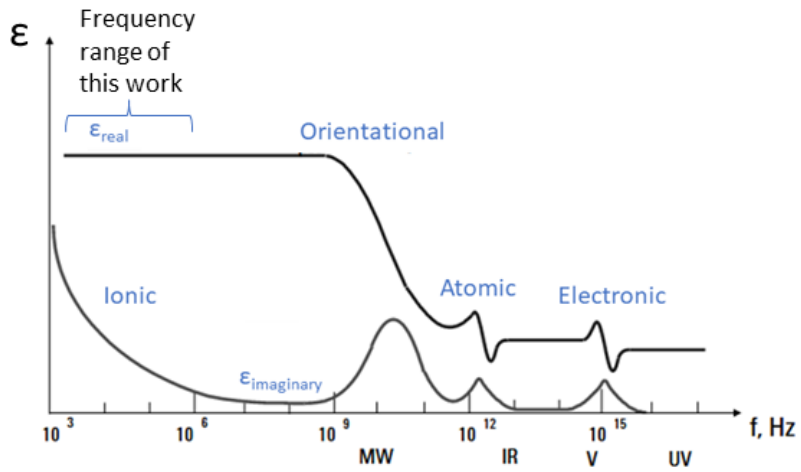

Figure 41 Various kind of polarization as a function of frequency.

Copper wires are attached to the silver electrodes, deposited on the sample via sputtering, using silver paste. The dielectric permittivity is measured as a function of temperature in a frequency range 10^3 to 10^6 Hz, using a *Solartron 1260 impedance analyzer* with a *dielectric interface of 1296*. The measurements are performed within a temperature range of 270 K to 370 K upon heating, as well as upon cooling, and the data points are collected every 2 K.

3.2.2 Polarization Hysteresis Measurement

The polarization hysteresis loops, energy storage and electromechanical properties of free-standing films were evaluated using a *TF Analyzer 2000 (Aixacct)* equipped with a temperature controller, and a laser interferometer. A triangular wave function is used, and a frequency of 10 Hz is employed for all measurements, unless otherwise mentioned. Unipolar as well as bipolar electric fields are used for the different measurements. The energy storage properties are evaluated by analyzing the $P - E$ loops measured under a unipolar field of varying amplitude. The field dependent mechanical strain curves are also measured to investigate the electromechanical properties.

3.2.2.1 Indirect Electrocaloric Effect

The indirect electrocaloric effect is calculated according to the method already explained in Section 2.2.2.1. The $P - E$ loops are converted to obtain the electrocaloric temperature and the entropy changes according to the Maxwell relations (Equations 11 and 12). In this work, all samples are measured in a temperature range between 298 K – 323 K, upon heating as well as upon cooling to eliminate the effect of processing. The $P - E$ loops measured upon cooling are then analyzed for the indirect calculation of the electrocaloric effect.

The impact of unipolar and bipolar field, frequency, and the leakage current on the indirect electrocaloric effect is analyzed. Unipolar or bipolar electric fields are applied to the sample to measure the $P - E$ loops. The unipolar and bipolar $P - E$ loops are measured at 10 Hz and 100 Hz.

Besides frequency and electric field, another parameter that is studied is the influence of the leakage current. In this regard, the unique feature of the leakage current compensation, available as a built-in function in the *Aixacct* measurement setup, is employed. The unipolar as well as bipolar $P - E$ loops are measured with and without the leakage current compensation.

3.2.2.1.1 Leakage Current Compensation

The principle of the leakage current compensation for the unipolar field is different from the bipolar field. In the case of a unipolar field, the voltage is increased stepwise, and the current is monitored during each voltage step, and after the decay of the load current. The load current decays exponentially, and the leakage current is estimated in the region of 70 % – 90 % of the step time, as shown in Figure 42. [155]

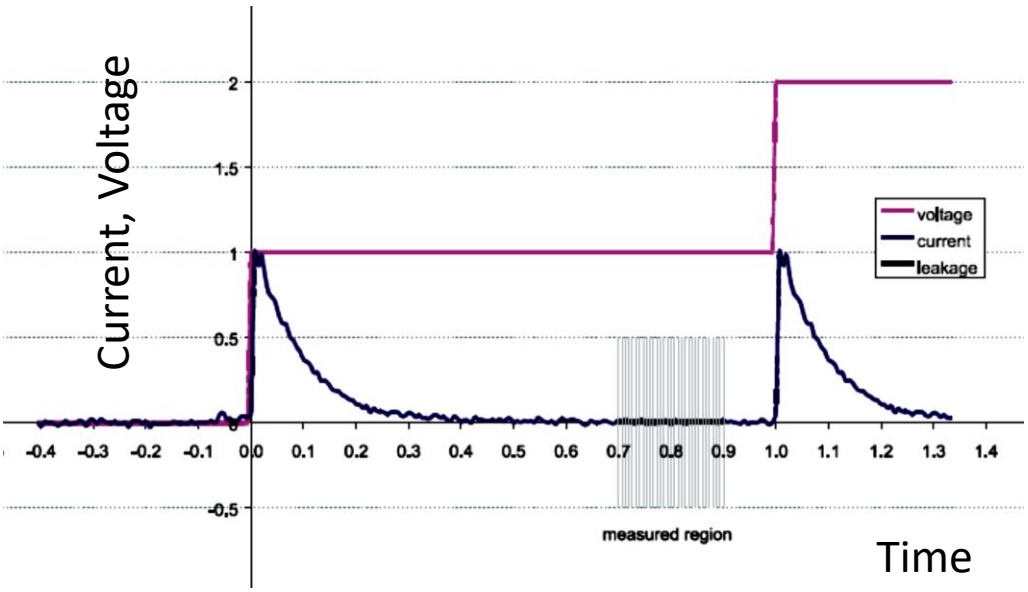

Figure 42 Leakage current estimation in *Aixacct*. [155]

To distinguish the leakage current from the ferroelectric switching current and dielectric displacement current under a bipolar field, another method is available in the *Aixacct* measurement system, named as Dynamic Leakage Current Compensation (DLCC). The working principle of this method is based on the frequency dependence of the ferroelectric, dielectric and the ohmic contributions to the total current. The dynamic leakage current compensation method mainly works by using different frequencies. Leakage current elimination is based on two bipolar measurements performed at adjacent frequencies.

The details and the assumptions of the dynamic leakage current compensation method have been reported elsewhere. [156] An analogy was established between a ferroelectric capacitor and an electrical circuit. The electrical behavior of a ferroelectric capacitor at a particular frequency is similar to an electrical circuit, having a parallel combination of a passive resistor and a passive

capacitor. This electric circuit is connected in parallel with a time invariant voltage-controlled charge source, serving for the displacement current in case of ferroelectric switching. It was assumed that the resistor (R) is only dependent on the applied voltage (V_{ext}), and the frequency (ω) dependence is not considered. The current (i_R) passing through the resistor (R) is given by:

$$i_R = \frac{V_{ext}}{R} \tag{33}$$

The capacitor in the same electrical circuit can also show a voltage dependence, and the current passing through the capacitor (i_C) can be calculated as,

$$i_C = j\omega C \times V_{ext} \propto \omega \tag{34}$$

The frequency dependence of the current caused by switching the ferroelectric polarization can be estimated through Equation 35, under the assumption, that the spontaneous polarization (P_S) of the ferroelectric capacitor will switch completely, when the external voltage (V_{ext}) is swept from V_{min} at t_0 to V_{max} at t_1. Thus, mathematically it can be written as,

$$P_S = \frac{1}{A}\int_{t_0}^{t_1} i_F \, d\tau \tag{35}$$

where, i_F represents the ferroelectric displacement current caused by the switching of the spontaneous polarization (P_S), and A is the area of the capacitor.

The time duration $t_0 - t_1$ is reciprocally comparable to the frequency of the voltage. The switching current is supposed to increase with frequency, to keep the spontaneous polarization constant, as in Equation 36.

$$i_F \propto \omega \tag{36}$$

It has been observed that the coercive voltage (V_C) increases weakly with frequency. Therefore, Equation 36 can be considered as a first-order approximation, and the frequency dependence of the coercive voltage can be neglected.

The total current (i) passing through the capacitor is calculated by the sum of the individual components, and can be written as,

$$i = i_R + i_C(\omega) + i_F(\omega) \tag{37}$$

When $i_C(\omega)$ and $i_F(\omega)$ have a linear dependence on the frequency, they can be replaced by $i_C^0 \times \omega$ and $i_F^0 \times \omega$, respectively, and the Equation 37 will become,

$$i = i_R + \omega i_C^0 + \omega i_F^0 \tag{38}$$

The difference Δi between currents for two frequencies, ω_1 and ω_2 (where $\omega_2 > \omega_1$), can be calculated according to Equation 38. The resistive element is assumed to be independent of frequency.

$$\Delta i = (\omega_2 - \omega_1)\left(i_C^0 + i_F^0\right) \tag{39}$$

Taking $\omega_2 = 2\omega_1$, the equation can be written as,

$$\Delta i = (\omega_1)\left(i_C^0 + i_F^0\right) \equiv \omega_1 i_C + \omega_1 i_F \equiv i_{comp}(\omega_1) \tag{40}$$

where, i_{comp} corresponds to the current response for a leakage free capacitor at frequency ω_1. Thus, for any frequency ω, the leakage current is eliminated, and the current response of the leakage free capacitor can be calculated as, [156]

$$i_{comp}(\omega) = \frac{\omega}{\omega_2 - \omega_1}[i(\omega_2) - i(\omega_1)] \tag{41}$$

The elimination of the leakage current is an important aspect, while measuring the *P – E* loops as a function of the temperature. The leakage current significantly increases with the temperature. The *P – E* loops measured at a higher temperature may contain huge errors in the polarization values due to the rapidly increasing leakage current. Subsequently, the indirectly calculated electrocaloric effect can also be erroneous. Therefore, the impact of the leakage current compensation on *P – E* loops and on the indirect electrocaloric effect is studied in detail in this work.

3.2.3 Quasi-Adiabatic Calorimetry

The direct electrocaloric measurement is conducted using an in-house built quasi-adiabatic calorimeter. This calorimeter consists of three chambers, namely, an outer vacuum chamber, a middle, and an inner chamber. The inner and the middle chambers are fabricated of copper to generate a (fairly) homogenous chamber wall temperature. The inner walls of the middle chamber

are coated with gold, while the inner chamber is fully gold coated to prevent the changes of the surface emissivity due to oxidation. Helium is used as the heat carrier between the chambers, and removed for the experiment, when the set-temperature is achieved everywhere in the chamber including the sample.

A customized sample holder and a sheathed thermocouple are introduced in the setup. The custom-designed sample holder is made of polytetrafluoroethylene (PTFE). The lower plate is sputter coated with silver electrodes, and the copper wire is attached to it with silver paste. The sample is placed on the lower plate in a way that the electrode area of the sample is in contact with the copper wire on the lower face, as shown in Figure 43. While the upper face of the electrode area of the sample is in contact with the sheathed thermocouple. The temperature of the heating line (Figure 44) is regulated, and measured by a *Lake Shore 336* controller. The voltage pulse is generated through a *National Instrument Card*, and amplified by a *Trek PD05034* high voltage amplifier. Due to the small capacitance of the samples, it is warranted that the current limit of the amplifier is not reached during the experiment. The data is collected using a LabVIEW program. [83]

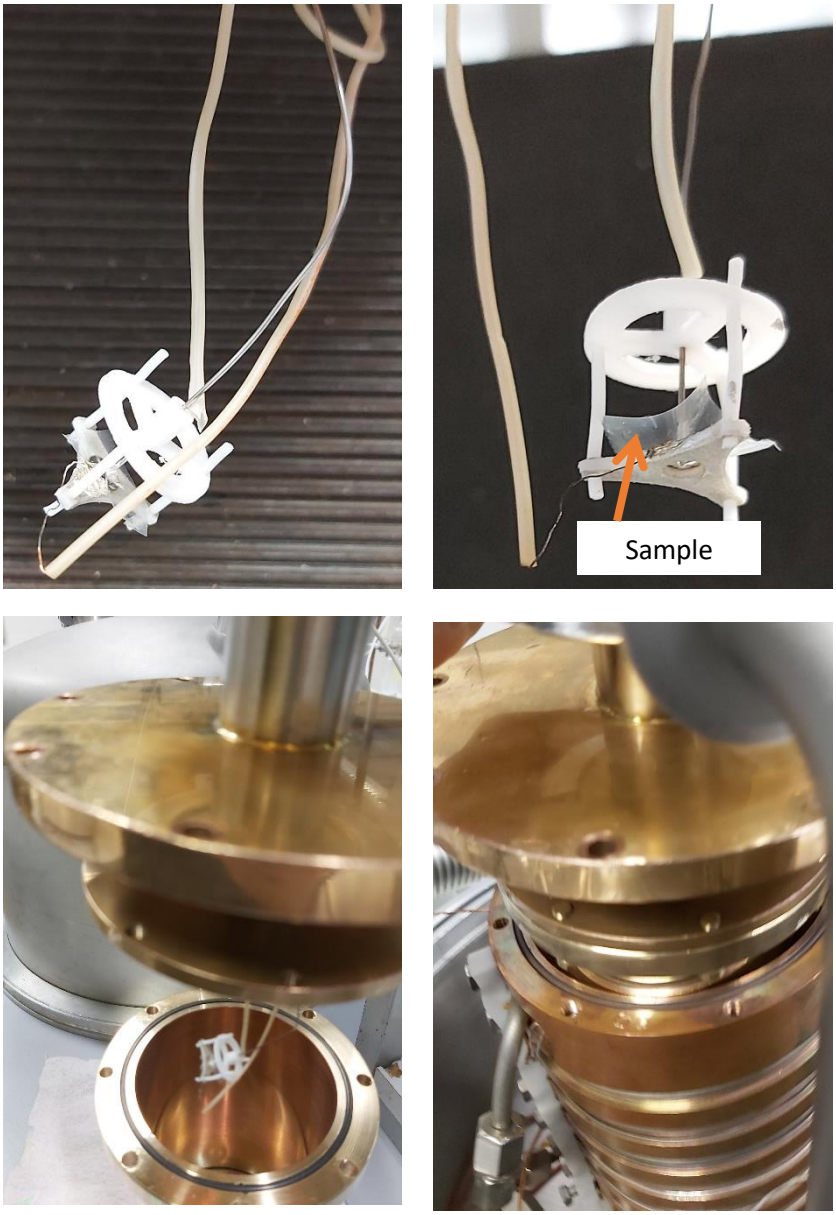

Figure 43 Sample holder for the quasi-adiabatic calorimeter with sample, copper wires and thermocouple, hanging in the inner chamber.

The quasi-adiabatic electrocaloric measurement runs as follows. Initially, the inner, middle, and outer chambers are evacuated, and the pressure drops to 2×10^{-5} mbar. The desired temperature is regulated, and helium is introduced into the outer chamber which is used for heat exchange between the chambers. The inner chamber remains evacuated during the measurements, apart for the measurements where the temperature interval was large. The temperature of the sample is adjusted to the desired value. The setup remains at this stage, until the temperature of the sample stabilizes, and does not fluctuate above 0.2 K within 5 min. The outer chamber is again evacuated, followed by the middle and the inner chambers. The system remains at this stage for precise adjustment of sample temperature. When the temperature fluctuation is not more than 0.08 K within 10 min, the system will move to the next stage, and the measurement will be initiated. [83] In this work, the measurements are performed from 298 K to 320 K with 4 K step size. The voltage amplitude is 1000 V and 1500 V. A saw shaped electric pulse with a slow field-on ramp (E_{on} = 0.1 kV/s) and fast field-off ramp (E_{off} = 100 kV/s) is used. The duration of the maximum applied electric field (E_{max}) is 0.1 s. The time lapse between the applied voltage pulses is 200 s.

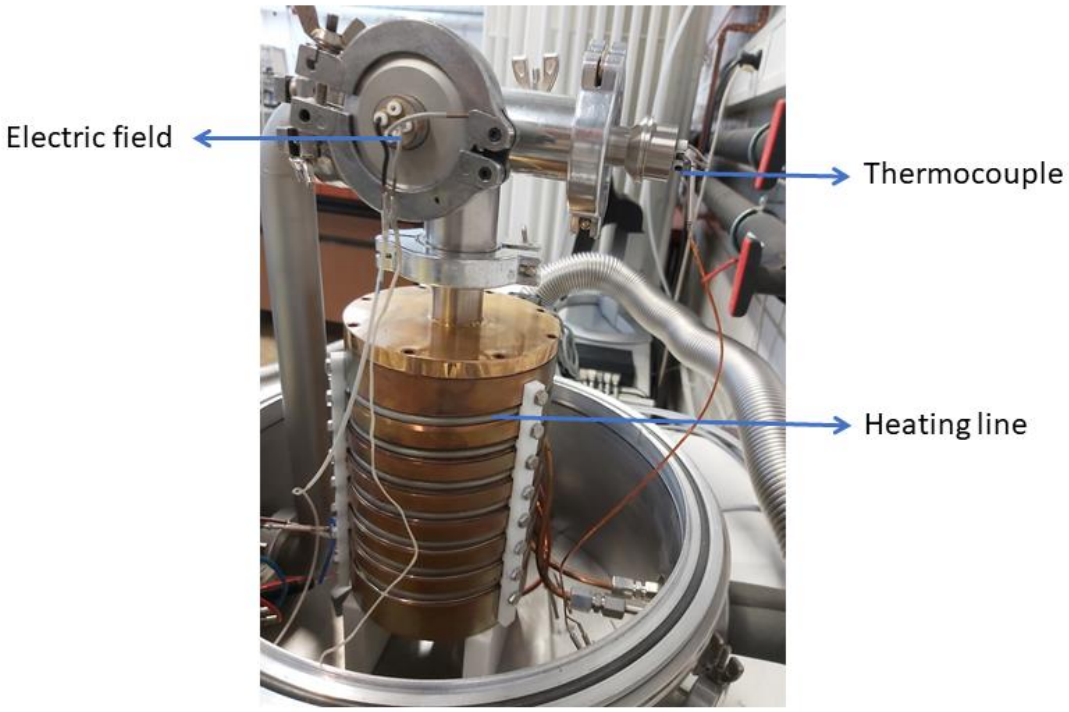

Figure 44 The outer chamber of the quasi-adiabatic calorimeter with thermocouple and voltage connections.

3.2.3.1 Correction for Heat Distribution during Direct Electrocaloric Measurement

Inside the quasi-adiabatic calorimeter, apart from the external thermal relaxation, a much faster internal relaxation also takes place due to the distribution of the heat generated by the EC-active element (sample volume under the electrodes). The ECE only concerns the sample volume under the electrodes, and the generated ECE heat flows to the other components of the system, such as the electrode-free part of the sample, electrodes, wires, and thermoelement. The internal relaxation occurs very fast, within a few milliseconds to seconds. [10] In order to estimate the actual EC temperature change ΔT_{EC}, the measured value, $\Delta T_{measured}$, must be corrected by taking into account the geometry of the system and the heat capacities of all components. [83]

$$\Delta T_{EC} = \Delta T_{measured} \cdot \frac{\sum_i c_p^i}{c_p^{EC}} \tag{42}$$

Here, C_p^i are the heat capacities of each individual component (EC active and inactive sample volume, electrical wires, electrodes, thermocouple) of the system, while C_p^{EC} is the heat capacity of the sample volume covered by the electrodes. For bulk materials and free-standing thick films, the ratio $\frac{\sum C_p^i}{C_p^{EC}}$ is between 1–1.5, the ratio of 1 indicates the absence of wires, electrode-free area of sample, and therefore is unrealistic. [10, 81] Whereas in films on a substrates, the ratio can easily exceed 10, depending on the thickness ratio between film and substrate. The correction factor becomes critical in the case of thin films, as the ratio $\frac{\sum C_p^i}{C_p^{EC}}$ can be of several thousand in this case. [10] In thin films, the $\Delta T_{measured}$ values are typically of a few mK, which is then calibrated using the correction factor. The incorrect estimation of the contributions from the EC inactive parts can be a major source of error. In this work, the sample is in the form of a free-standing thick film, which is placed on a hollow plate that serves as the substrate. The hollow plate is used due to the low thermal mass of polymer, and sample part under the electrodes is not in contact with the substrate, as schematically shown in Figure 45. The heat generated in the EC–active element will flow to the EC–inactive sample volume, silver electrodes, silver paste, attached copper wires, and sheath thermocouple made of steel. Since, the EC active sample volume is not in contact with the hollow plate, therefore it is assumed that the heat transfer to the plate will only occur from the EC inactive sample volume, and is not considered.

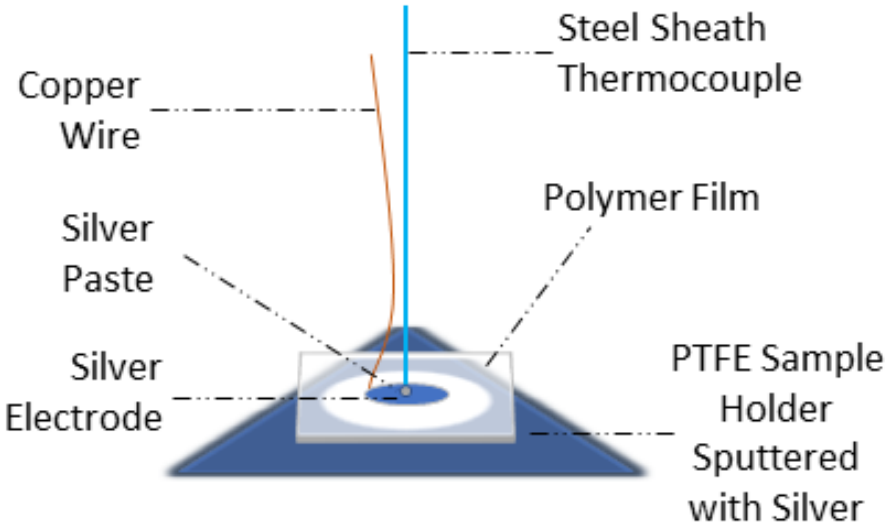

Figure 45 Schematic illustration of electroded polymer films sample placed on the sample with other components (wires, thermocouple, silver paste).

Consider the polymer sample which is 20 µm thick, with 1 cm × 1 cm width and length, the volume will be,

$$Total\ volume\ of\ the\ sample\ =\ 2 \times 10^{-9} m^3$$

The diameter of the sputtered silver electrode is 0.5 cm, so the EC–active sample volume can be calculated as the volume of a cylinder($d = 0.5\ \times 10^{-2} m, h = 20 \times 10^{-6} m$),

$$Sample\ volume\ under\ electrodes = 3.93\ \times 10^{-10} m^3$$

And the inactive sample volume will be,

$$EC-inactive\ sample\ volume\ =\ 1.61 \times 10^{-9} m^3$$

The above-mentioned values of the volume can be converted into mass taking the density of P(VDF–TrFE–CFE) $\rho = 1920\ kg/m^3$.

$$Total\ mass\ of\ the\ sample = 3.84 \times 10^{-6}\ kg$$

$$Mass\ of\ sample\ under\ the\ electrodes = 7.54 \times 10^{-7}\ kg$$

$$EC-inactive\ mass\ of\ sample = 3.09 \times 10^{-6}\ kg$$

$$Total\ mass\ of\ silver\ electrodes = 2.06 \times 10^{-8}\ kg$$

$$Mass\ of\ silver\ paste = 1.0 \times 10^{-6}\ kg$$

$$Assumed\ mass\ of\ thermocouple\ and\ copper\ wires = 1.58 \times 10^{-5}\ kg$$

Taking the following heat capacities;

$$c_p^{polymer} = 1.5\ kJ/kg \cdot K$$

$$c_p^{Ag} = 0.24\ kJ/kg \cdot K$$

$$c_p^{steel} = 0.49\ kJ/kg \cdot K$$

$$c_p^{Cu} = 0.38\ kJ/kg \cdot K$$

$$Correction\ factor = \frac{\sum c_p^i \times mass^i}{c_p^{polymer} \times mass^{EC\ active}} \quad (43)$$

After inserting all the values in Equation 43,

$$\boldsymbol{Correction\ factor = 12\ \pm 6}$$

3.2.4 X-Ray Diffraction Analysis

The XRD is one of the most established and robust (nondestructive) technique for the characterization of crystalline materials. This technique is used to deduce information about the crystal structure, phases, and preferred crystal orientation (texture). Several other datasets which are correlated to the atomic arrangement and microstructure, and microstrain can also be extracted through XRD diffractogram. The working principle of the X-ray diffraction (XRD) technique is based on Bragg's law (Equation 44) as depicted in Figure 46.

$$n\lambda = 2dsin\theta \quad (44)$$

Where, n is an integer, λ is the wavelength of the incident beam, d is the interplanar distance and θ is the angle of incidence.

A monochromatic beam of X-rays is incident on the sample. Since the atoms are arranged in a periodic structure in crystalline materials, constructive as well as the destructive interference occurs. The outgoing beam is (elastically) scattered at specific angles according to Bragg's law, and is detected by the detector. The detected rays generate a unique diffraction pattern that presents several sharp peaks, also known as Bragg diffraction peaks.

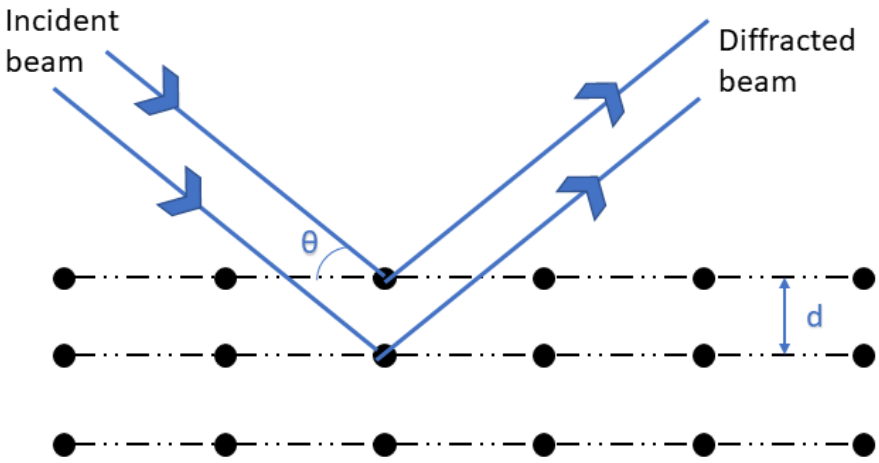

Figure 46 Schematic illustration of the working principle of X-ray diffraction (XRD).

The XRD measurement is conducted using a *Panalytical Empyrean* (Cu Kα radiation) diffractometer over a 2-θ range of 10–80° with a step size of 0.05°. The collected diffractograms are analyzed using the *HighScore Plus (version 4.7)* software.

3.2.5 Scanning Electron Microscopy

The scanning electron microscope (SEM) is a versatile state-of-the-art instrument, which is widely used to study the microstructure and the surface of materials. A high-energy electron beam is used in the SEM, which reveals the information about the topography, morphology, orientation of grains, grain boundaries, impurities etc. in the material. Hence, SEM is a robust tool for microstructural characterization of the materials. The image is produced by scanning the sample surface with a high-energy beam of electrons. The primary electron beam is generated at the top of the microscope by an electron gun under a high vacuum, and scanned across the surface of the sample (Figure 47). The primary electron beam travels through electromagnetic lenses, which focus the beam down towards

the sample surface. As the beam hits the sample, the primary electrons interact with the sample; the interaction volume depends on the accelerating voltage. Subsequently, the backscattered electrons (BSE) (electrons which are reflected after an elastic interaction with the sample), secondary electrons (SE) (ejected by the atoms of the sample after inelastic interaction with the primary electron beam), and X-rays are ejected from the sample. The ejected secondary electrons and backscattered electrons are collected by the detector to form an image. The secondary electrons provide information about the topographic contrast.

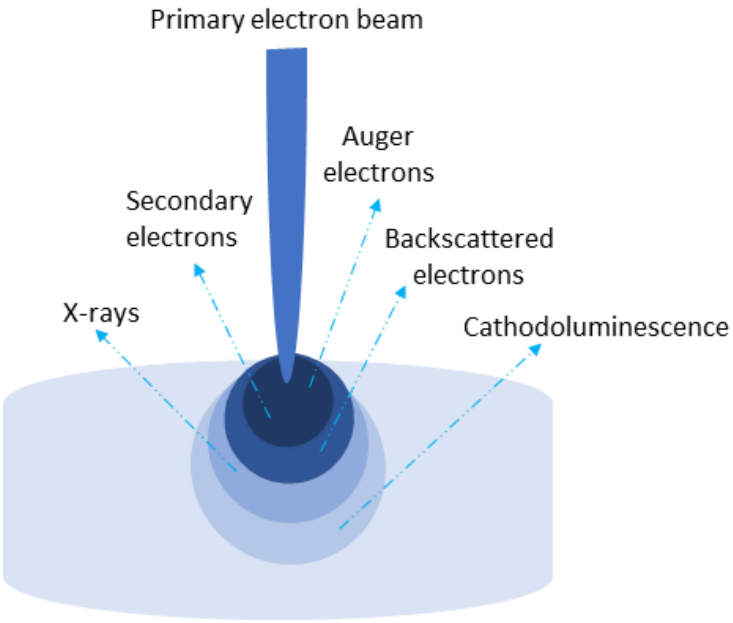

Figure 47 Interaction depth of an electron beam with a material and the corresponding emitted rays.

The SEM images are collected using an *ESEM Quanta 400 FEG, FEI*. Two-sided carbon tape is fixed to a SEM sample holder; the nanoparticles are sprinkled, or the polymer film is affixed onto the surface of the carbon tape. The samples are then sputtered with silver for 15 s to make them conductive. The particle size distribution is measured by analyzing the SEM images through *ImageJ version 1.52a.* Statistical functions are used to obtain the cumulative as well as the frequency distribution of the particle size. For the cross-sectional analysis of the nanocomposite film, the cryofracture technique is utilized to break the film. The free-standing film is immersed in liquid nitrogen and broken into fragments through slight hits.

3.2.6 Differential Scanning Calorimetry

The differential scanning calorimetry (DSC) is a useful technique for the analysis of thermal events, oxidation, and thermal degradation. DSC is a quantitative method that allows the determination of the heat capacity, melting temperature, crystallization temperature, glass transition temperature (T_g), phase transition temperature and their respective enthalpies. It measures the heat transferred to or from a sample undergoing a thermophysical or thermochemical change.

The dynamic scanning calorimetry analysis is conducted on the powder samples using a *DSC-204 (Netzsch)* setup. The amount of power required to keep the difference in temperature between the reference and the sample close to zero is used to calculate the heat flow. All the samples are analyzed upon heating as well as cooling to estimate the melting and crystallization temperatures, respectively. 10 mg of polymer powder is placed in the aluminum crucible, and the lid is pressed. The P(VDF-TrFE-CFE) powder samples are analyzed in a temperature range between 0°C→150°C→0°C, while the P(VDF-TrFE) is analyzed between 0°C→190°C→0°C. The heating and cooling rates are 10 K/min. Liquid nitrogen is used to regulate the temperature during measurement. The enthalpies of melting, crystallization and phase transition are determined by estimating the area under the respective peaks (Figure 48).

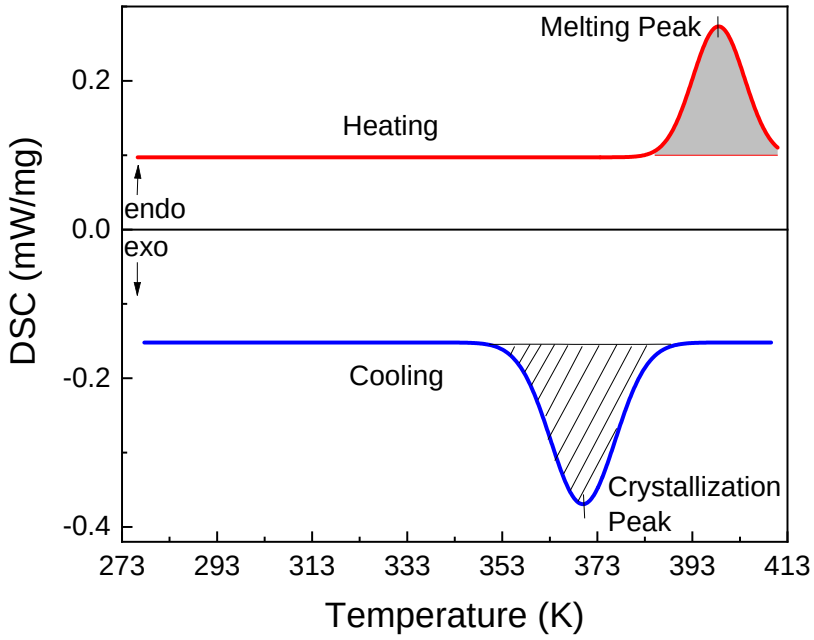

Figure 48 Output of differential scanning calorimetry with heating and cooling curves. The melting and crystallization peaks are measured along with their respective enthalpies (area under the peak).

4 Results & Discussion

This chapter, namely results and discussion, is subdivided into four sections. The first two sections focus on the material structure-property characterization. While, the other two sections focus on the functionality of the material for cooling (electrocaloric) and electrical energy storage applications. The synthesis and processing of materials, analyzed in this section, and the details of characterization methods and parameters, have been discussed in Chapter 3.

4.1 Comparison of Ferroelectric & Relaxor Properties

It has been already discussed that the incorporation of a bulky monomer like chlorofluoroethylene into P(VDF-TrFE) drastically alters the properties of ferroelectric compositions. In this section, the crystal structure, thermophysical, dielectric, ferroelectric, and electromechanical properties of well-known ferroelectric copolymer composition P(VDF-TrFE) 70/30 and the relaxor terpolymer composition P(VDF-TrFE-CFE) 70/30/8.1 are studied. A comparison between the ferroelectric and relaxor properties is shown (Figure 49). The X-ray diffraction technique is employed to examine the crystal structure. The dynamic scanning calorimetry is used to study the thermal phase transitions in powder samples. The dielectric and the ferroelectric properties are investigated using dielectric spectroscopy and polarization hysteresis loops. The electromechanical properties of the ferroelectric copolymer and the relaxor terpolymer compositions are analyzed.

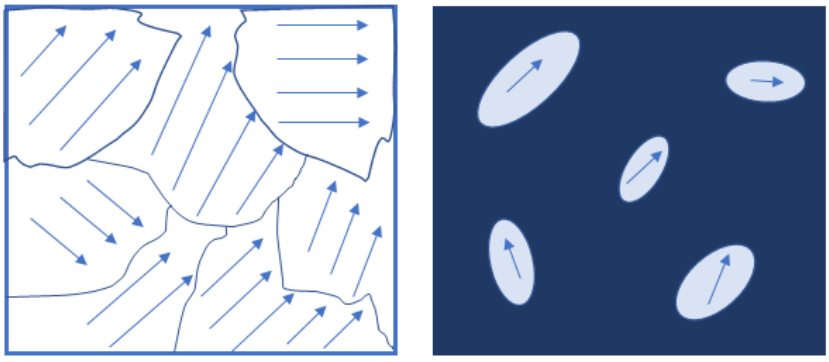

Figure 49 Schematic illustration of ferroelectric (left), and a relaxor with polar nanoregions (right).

4.1.1 Crystal Structure Analysis

In Figure 50, the XRD diffractograms of P(VDF-TrFE) 70/30 and P(VDF-TrFE-CFE) 70/30/8.1 are depicted. P(VDF-TrFE) 70/30 show a peak at 19.2° with the interchain space (d) of 4.62Å, characterizing the β phase, which is ferroelectric. P(VDF-TrFE-CFE) 70/30/8.1 has a narrow peak at 17.8°, and the interchain space (d) is 4.96Å. The peak at 17.8° in the P(VDF) based polymers represents the α crystalline phase, which is non-polar and paraelectric. The processing parameters for P(VDF-TrFE) 70/30 and P(VDF-TrFE-CFE) 70/30/8.1 are similar, but the peak position and lattice spacing are different in both samples, which shows that the incorporation of CFE monomers influences the crystalline phase. The interchain space of terpolymer is larger than for the copolymer. The van der Waals radius of chlorine is 1.8Å, which is larger than the van der Waals radius of fluorine (1.35Å), therefore the incorporation of CFE monomers in P(VDF-TrFE) chain results in an increase in the distance between the P(VDF-TrFE-CFE) chains. [157] The expansion of the interchain spacing results in weakened interchain interactions, which favors the gauche state in the isolated terpolymer chains. [158]

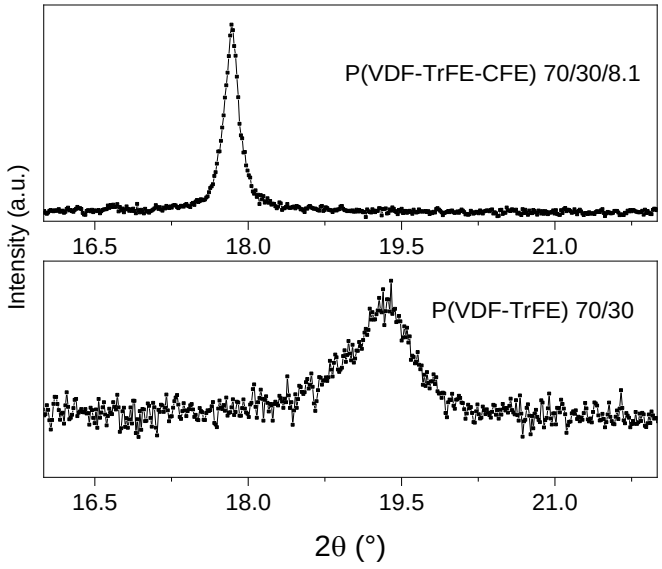

Figure 50 X-ray diffractogram of P(VDF–TrFE–CFE) 70/30/8.1, and P(VDF–TrFE) 70/30.

4.1.2 Thermophysical Analysis

The differential scanning calorimetric analysis is performed to investigate the thermophysical properties, and the associated phase transitions in the copolymer P(VDF-TrFE) 70/30 and the terpolymer P(VDF-TrFE-CFE) 70/30/8.1 compositions. The heating curve of P(VDF-TrFE) 70/30 shows two distinct peaks, one corresponds to the ferroelectric–paraelectric phase transition, while the other is the melting peak, (Figure 51). On the other hand, P(VDF-TrFE-CFE) 70/30/8.1 shows only the melting peak which is shifted to a lower temperature. The cooling curves follow a similar trend, which are shown in Figure 52. The recrystallization peaks can be observed for both compositions, and the paraelectric–ferroelectric transition peak of P(VDF-TrFE) 70/30 is very distinct. The peak of the ferroelectric to paraelectric transition in the copolymer composition is at 358 K, while the paraelectric–ferroelectric transition (cooling) is at 334 K. There is a thermal hysteresis, and the F–P (heating) and P–F (cooling) temperatures have 25 K difference. Such a thermal hysteresis in the DSC measurements has already been observed in different P(VDF-TrFE) compositions. The presence of a thermal hysteresis F–P (heating) and P–F (cooling) temperatures indicates the first-order phase transition. [159]

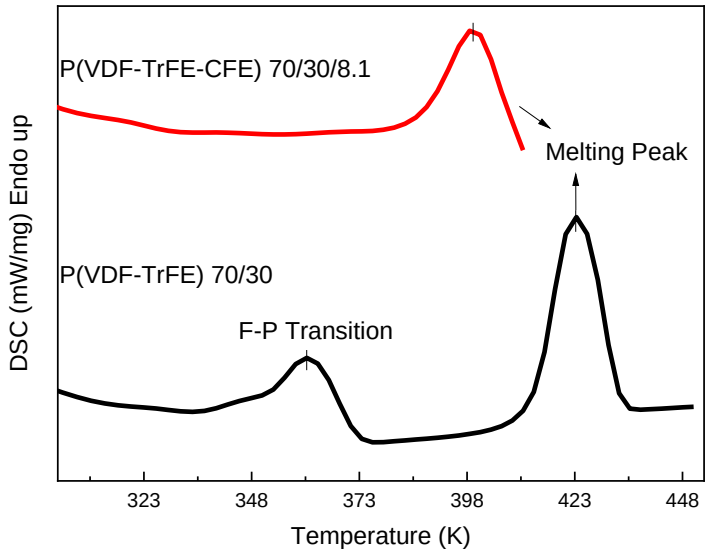

Figure 51 DSC scan of P(VDF–TrFE–CFE) 70/30/8.1, and P(VDF–TrFE) 70/30 recorded upon heating with melting and phase transition peaks.

The phase transition temperature is estimated from the position of the respective peak, while the associated enthalpy change is estimated by integrating the area under the peak, as enlisted in Table

8. It can be observed that the incorporation of –CFE monomer in P(VDF-TrFE) 70/30 shifts down the melting and recrystallization temperatures, and lowers their respective enthalpy changes. This trend is in agreement to previous reports. [158, 160]

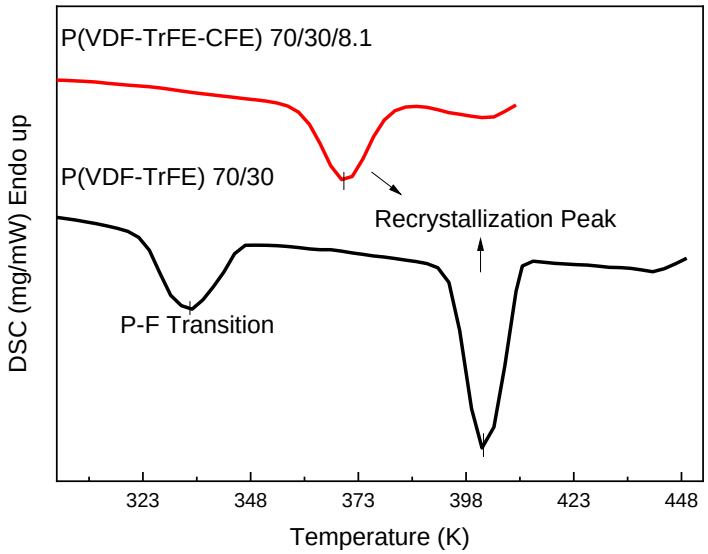

Figure 52 DSC scans of P(VDF–TrFE–CFE) 70/30/8.1, and P(VDF–TrFE) 70/30 recorded upon cooling with crystallization and phase transition peaks.

Table 8 Comparison of the thermophysical properties of P(VDF-TrFE) 70/30 & P(VDF-TrFE-CFE) 70/30/8.1 compositions studied through differential scanning calorimetry (DSC) (NA = not applied).

	$P(VDF_x\text{-}TrFE_{1-x})$ (mol. %) 70/30	$P(VDF_x\text{-}TrFE_{1-x}\text{-}CFE_y)$ (mol. %) 70/30/8.1
Ferroelectric–Paraelectric Transition (K)	358	NA
Enthalpy of Ferroelectric–Paraelectric Transition (J/g)	11.3	NA
Melting Temperature (K)	424	398
Enthalpy of Melting (J/g)	26.7	14.4
Crystallization Temperature (K)	401	370
Enthalpy of Crystallization (J/g)	28.4	16.3
Paraelectric–Ferroelectric Transition (K)	334	NA
Enthalpy of Paraelectric–Ferroelectric Transition (J/g)	18.5	NA

4.1.3 Dielectric Properties

The dielectric permittivity and loss tangent curves of both compositions, measured upon heating as a function of frequency in a range of 1 kHz to 1 MHz, are shown in Figure 53. The P(VDF-TrFE) 70/30 sample is measured from room temperature to 390 K, while P(VDF-TrFE-CFE) 70/30/8.1 is measured from 270 K – 370 K, owing to their different transition temperatures. The dielectric permittivity curves of the P(VDF-TrFE) 70/30 composition show a ferroelectric to paraelectric transition peak at 378 K (Curie temperature (T_c)) estimated by the peak maximum. The incorporation of 8.1 mol.% CFE into the P(VDF-TrFE) 70/30 shifts the position of the maximum dielectric permittivity towards room temperature, and broadens the maximum. The P(VDF-TrFE) 70/30 permittivity curves do not show frequency dependent dispersion, while the position of the maximum of the P(VDF-TrFE-CFE) 70/30/8.1 sample is shifting towards a higher temperature with increasing frequency. The relaxor behavior is characterized by such diffuse peaks and frequency dependent dispersion. [161] The modified Curie-Weiss law is widely utilized to approximate the temperature dependence of $\varepsilon(T)$ above T_m (Equation 45). [162]

$$\frac{\varepsilon_m}{\varepsilon(T)} - 1 = \left(\frac{T - T_m}{2\sigma}\right)^{\gamma} \tag{45}$$

Here, ε_m is the maximum value of the dielectric permittivity, T_m is the temperature at the maximum permittivity, the parameter σ defines the broadening of the dielectric peak, and the exponent γ signifies the degree of the relaxor behavior. The value of γ is equal to 1 for classical ferroelectric materials, whereas for the canonical relaxors, its value approaches 2. [163] The γ value of P(VDF-TrFE-CFE) 70/30/8.1 is 1.50 (Table 9) which is higher than for P(VDF-TrFE) 70/30 (γ = 1.24), thus confirming the relaxor behavior of P(VDF-TrFE-CFE) 70/30/8.1.

Table 9 Dielectric characteristics of ferroelectric copolymer and relaxor terpolymer compositions (NA = not applied).

	$P(VDF_x\text{-}TrFE_{1-x})$ (mol. %) 70/30	$P(VDF_x\text{-}TrFE_{1-x}\text{-}CFE_y)$ (mol. %) 70/30/8.1
Degree of dielectric relaxation (γ)	1.24	1.50
Curie Transition Temperature (T_c)	378 K	NA
Freezing Temperature (T_f)	NA	280 ± 2 K

At 1 kHz, the maximum value of the relative dielectric permittivity values of P(VDF-TrFE) 70/30 and P(VDF-TrFE-CFE) 70/30/8.1 are ~120 and ~80, respectively, which are comparable to previous reports. [80] Comparing the tangent loss curves of copolymer and terpolymer compositions between 360 K and 370 K, it can be noted that the tan loss values in P(VDF-TrFE-CFE) are almost double than those in P(VDF-TrFE), although both film samples are prepared under the same processing conditions and parameters. It has been already reported that the presence of polar group(s) causes conductivity losses, for example, the dielectric losses in polyvinylidene chloride (PVC) are significantly higher than in polyethylene (PE) due to the presence of a polar entity i.e. chlorine. [50, 164, 165] Thus, it is plausible to conclude that the higher losses in P(VDF-TrFE-CFE) compared to P(VDF-TrFE) can be due to the presence of –CFE monomers.

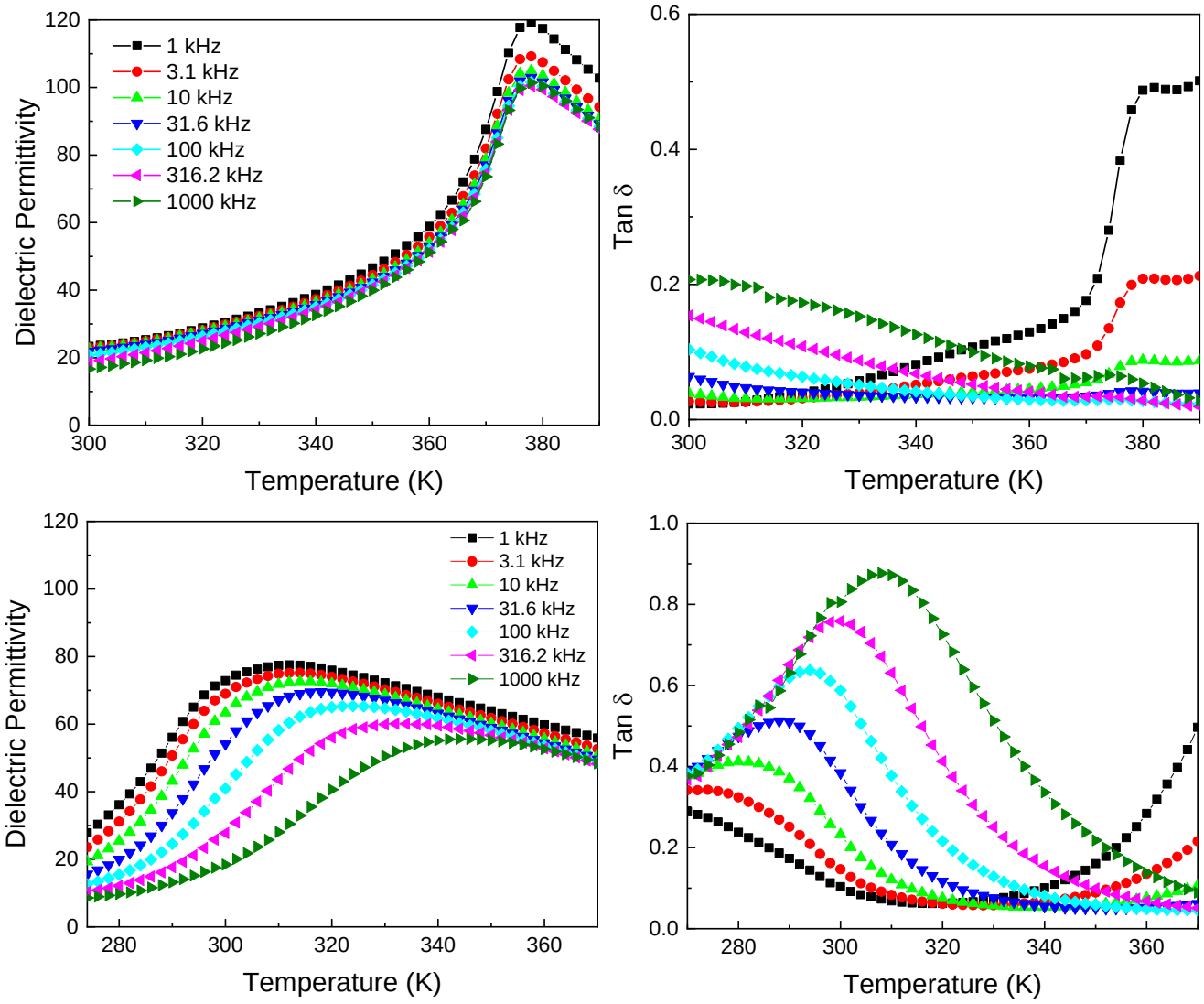

Figure 53 Dielectric permittivity and tan losses of P(VDF–TrFE) 70/30 (top), and of P(VDF–TrFE–CFE) 70/30/8.1 (bottom).

4.1.4 Polarization Behavior

The polarization hysteresis loops of copolymer and terpolymer compositions measured at room temperature are shown in Figure 54. P(VDF-TrFE) 70/30 shows a typical ferroelectric loop with wide hysteresis. The remnant polarization and coercive field of P(VDF-TrFE) 70/30 are much higher than of P(VDF-TrFE-CFE) 70/30/8.1, as enlisted in Table 10. P(VDF-TrFE-CFE) 70/30/8.1 shows a slim loop with a double hysteresis, that is attributed to the field induced phase transition. Such double hysteresis loops have been previously reported in P(VDF) terpolymers. [54] From the XRD analysis, it is already observed that the incorporation of CFE monomers in P(VDF-TrFE) chain expands the interchain distance in P(VDF-TrFE-CFE) chains, which is in agreement with literature. [158] This causes the weakening of the cooperative or coherent polarization of the P(VDF-TrFE) dipoles, and reduces the size of the ferroelectric domains to the nanoscale. The structure of the relaxor P(VDF-TrFE-CFE) contains more or less random T_mG ($m \leq 4$) sequences, while the ferroelectric structure contains relatively long T*n* ($n > 4$) sequences (T and G represent the trans and gauche conformations, while m and n represent the numbers of segments, respectively). [166] CFE possesses its own dipole moment. When the magnitude of the applied electric field is large enough, the dipoles of CFE may rotate which favors the switching of the surrounding P(VDF-TrFE) dipoles, and the formation of a ferroelectric state with large domains. [166] These FE domains transform back to the disordered relaxor phase with decreasing electric field which is later removed as shown in Figure 54.

Table 10 Comparison of ferroelectric characteristics of P(VDF–TrFE) 70/30 and P(VDF–TrFE–CFE) 70/30/8.1. (NA = not applied)

	$P(VDF_x\text{-}TrFE_{1-x})$ (mol. %) 70/30	$P(VDF_x\text{-}TrFE_{1-x}\text{-}CFE_y)$ (mol. %) 70/30/8.1
Saturation Polarization (P_{sat}) ($\mu C/cm^2$)	8.6	NA
Maximum Polarization (P_{max}) ($\mu C/cm^2$)	NA	6.2
Remnant Polarization (P_{rem}) ($\mu C/cm^2$)	6.9	0.46
Coercive Field (E_c)(MV/m)	28	4.5

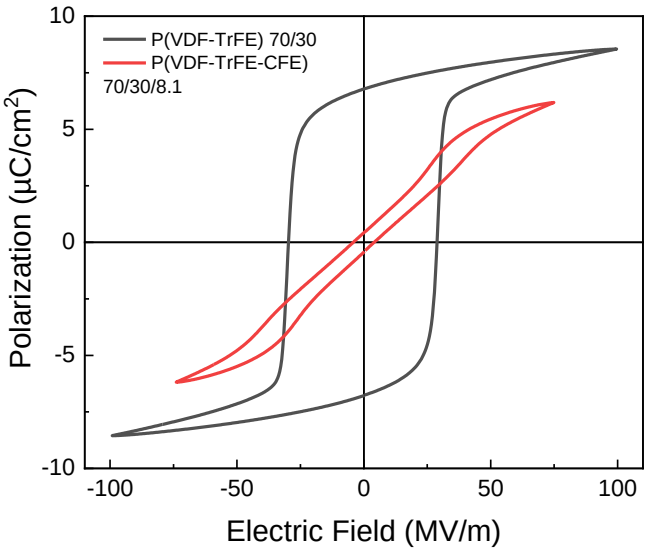

Figure 54 Polarization hysteresis loops of P(VDF–TrFE) 70/30 and P(VDF–TrFE–CFE) 70/30/8.1 at room temperature.

4.1.5 Electromechanical Properties

In Figure 55, the displacement curves of the copolymer and terpolymer compositions are plotted against the applied voltage. The film samples of both compositions contract under an applied electric field resulting in negative values of displacement. The strain and the longitudinal piezoelectric coefficient (d_{33}) are calculated, and given in Table 11. The piezoelectric coefficient (d_{33}) of the copolymer composition is calculated from the slope of the discharging branch at lower magnitude of the applied electric field. The piezoelectric coefficient (d_{33}) of the copolymer composition P(VDF-TrFE) 70/30 is - 39 pm/V, which is almost the same as the previously reported values. [167] The negative strain and piezoelectric coefficient show the longitudinal contraction along the direction of the applied electric field. The strain values of P(VDF-TrFE-CFE) 70/30/8.1 are superior to those of P(VDF-TrFE) 70/30 even at a lower applied voltage. The strain in relaxor composition is almost double (0.35 %) than in the copolymer composition (0.80 %). The large electrostriction in the relaxor terpolymer is beneficial for electromechanical applications. The losses in P(VDF-TrFE-CFE) 70/30/8.1 are also minimal compared to P(VDF-TrFE) 70/30 due to the relaxor characteristics. These findings are in agreement with previous reports, where similar copolymer and terpolymer compositions have been studied. [167]

Table 11 Electromechanical properties of copolymer 70/30 and terpolymer 70/30/8.1.

P(VDF-TrFE) 70/30				P(VDF-TrFE-CFE) 70/30/8.1	
Maximum Strain (%)	0.35	d_{33}	-39 pm/V	Maximum Strain (%)	0.80

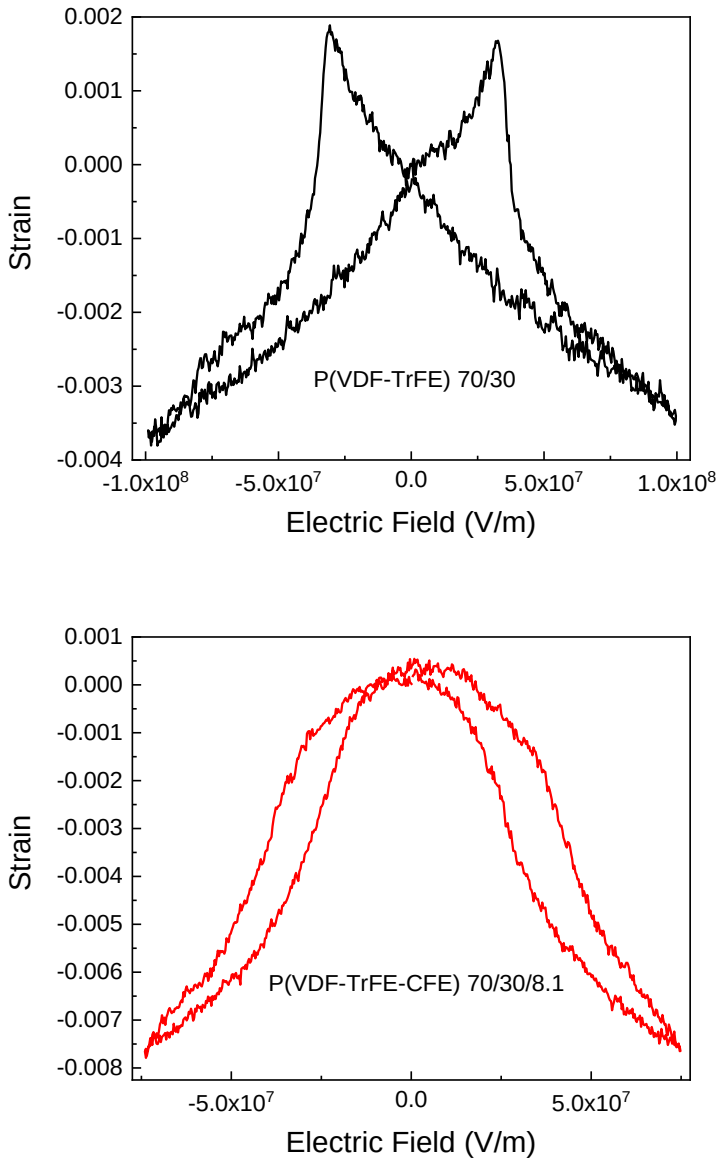

Figure 55 Strain voltage loops of copolymer 70/30 and terpolymer 70/30/8.1.

4.1.6 Conclusion

The crystal structure, thermophysical properties, dielectric, polarization and electromechanical properties of the ferroelectric copolymer P(VDF–TrFE) 70/30 and the relaxor terpolymer P(VDF–TrFE–CFE) 70/30/8.1 compositions are compared. The incorporation of 8.1 mol.% CFE in P(VDF–TrFE) 70/30 alters the crystal structure from ferroelectric **β** to paraelectric **α** phase, by breaking the long range ordering of all-trans, and due to the large interchain distance. The phase transition as well as the melting and recrystallization temperatures of P(VDF–TrFE) 70/30 are shifted towards a lower temperature due to the presence of CFE monomer, as observed by the DSC analysis. The dielectric measurements of P(VDF–TrFE) 70/30 show a sharp transition peak at 378 K, which becomes broad and shifted towards room temperature with a frequency dispersion in P(VDF–TrFE–CFE) 70/30/8.1, confirming its relaxor behavior. The polarization hysteresis loop of P(VDF–TrFE) 70/30 shows a high remnant polarization, which is typical for pure ferroelectrics. While P(VDF–TrFE–CFE) 70/30/8.1 shows a slim hysteresis loop and undergoes a field induced phase transition. In the reported work, the FTIR spectra, recorded under a high electric field (100 MV/m), showed that the **α** phase can be converted to the **δ** as well as the **β** phase. [168] Therefore, it is plausible to assume that the phase formed under an applied electric field is a mixture of all-trans (**β** phase) and polar trans-gauche (**δ** phase) conformations. The electrostrictive strain in P(VDF–TrFE–CFE) 70/30/8.1 is superior to its ferroelectric counterpart.

4.2 Effect of Composition on Polarization Hysteresis & Relaxor Properties of P(VDF-TrFE-CFE)

It has been shown in the previous section that the P(VDF-TrFE-CFE) relaxor terpolymer has low hysteresis losses. The relaxor properties are introduced in P(VDF-TrFE-CFE) terpolymers when the VDF/TrFE molar ratio is below 75/25, and the molar amount of CFE is above 4%. [52, 53, 57] There are many possible compositions of relaxor terpolymers, but only a few compositions have been reported so far. Therefore, the dielectric and ferroelectric properties of terpolymers in a broader concentration range should be investigated to understand the mechanism of the formation of the relaxor state, and the relationship between the property and composition in the terpolymers.

In this section, the detailed analysis of six different compositions of P(VDF-TrFE-CFE) is presented.[1] The molar fraction of each monomer in terpolymer is depicted in Figure 56, and is already listed in Table 7 in Section 3.1. The three compositions: 51.3/48.7/6.2, 59.8/40.2/7.3, and 70/30/8.1, are studied for the first time, to the best of the author's knowledge. The crystal structure and the microstructure are examined using the X-ray diffraction technique and scanning electron microscopy. The thermophysical properties of all powder samples are studied using DSC. Dielectric spectroscopic measurements are carried out, and the dielectric spectra are evaluated to assess the relaxor characteristics, such as the freezing temperature. The polarization behavior of all compositions is discussed in detail with a special focus on the electric field induced ferroelectric phase transition. The electrostriction and energy storage properties of all compositions are analyzed and compared.

[1] *A major portion of section 4.2 has been published in "Polymers" Volume 13, Issue 8, 2021, under the title of "Effect of Composition on Polarization Hysteresis and Energy Storage Ability of P(VDF-TrFE-CFE) Relaxor Terpolymers".*

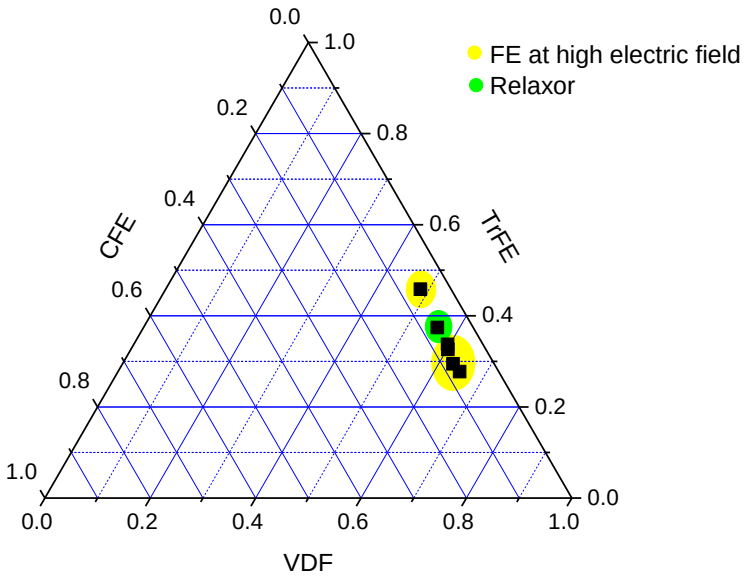

Figure 56 The ternary compositional diagram of P(VDF-TrFE-CFE) indicating the compositions studied in this work. [151]

4.2.1 X-Ray Diffraction

In Figure 57, the XRD patterns of terpolymer film samples are shown. All studied compositions show a peak at 17.8°, and an interchain spacing of 4.9Å, which represents the paraelectric α crystalline phase. Bao et al. reported the presence of the α crystalline phase in a similar composition, namely P(VDF-TrFE-CFE) 61.5/30.3/8.2 (notated as P(VDF_x-$TrFE_{1-x}$-CFE_y) 67/33/8.9 in this work), when the terpolymer film was annealed at 110°C under vacuum for 24 h, and slowly cooled down to room temperature. Their processing parameters are similar to the ones used in this work i.e. drop casting and drying from the DMF solution, followed by annealing under vacuum and cooling. [158]

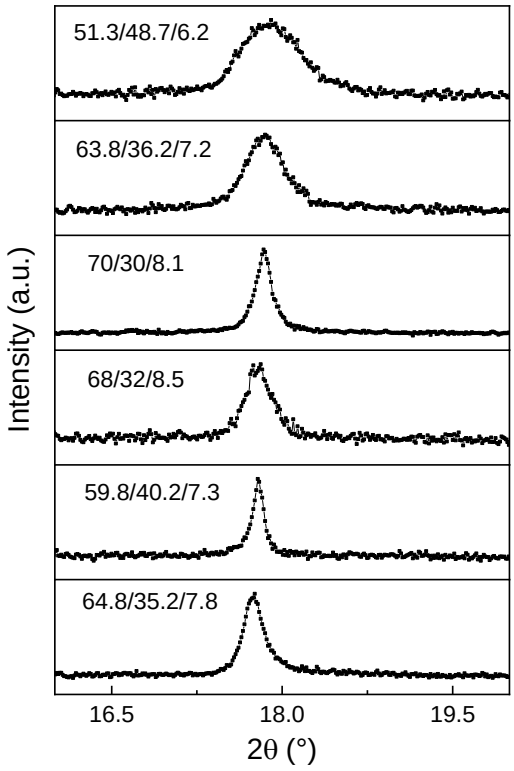

Figure 57 X-ray diffractograms of all studied compositions of P(VDF–TrFE–CFE).

4.2.2 SEM Analysis

A representative image of the microscopic morphology of the terpolymer film sample is revealed using the SEM, as shown in Figure 58. All the compositions are processed under the same conditions to fabricate free-standing films. The terpolymer film sample (P(VDF-TrFE-CFE) 64.8/35.2/7.8) represents that the processing of the polymer solution in the vacuum oven results in a uniform and dense structure. There are no visible pores, voids, cracks or any impurities under a magnification of 15000 x in the film sample. The terpolymer film adapted a lamellar morphology which can be clearly observed in Figure 58.

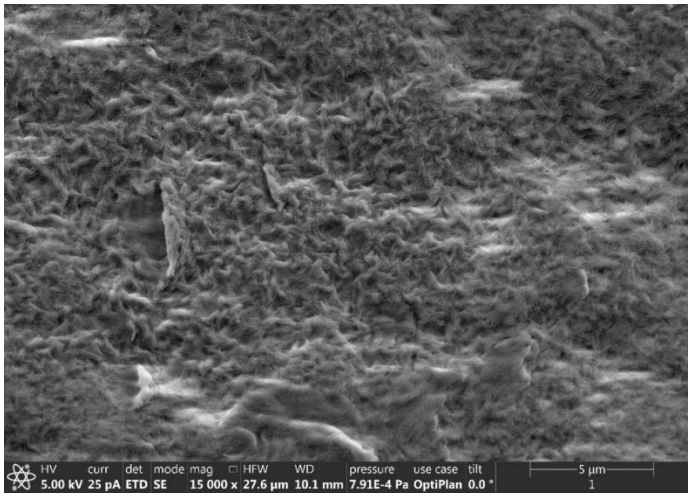

Figure 58 Scanning electron microscope (SEM) representative image of free-standing polymer film.

4.2.3 Thermal Analysis

The impact of the compositional variation on the thermal properties (melting and recrystallization temperatures) of the polymer powder is studied. The melting and recrystallization temperatures of all samples are determined from the positions of the endo – and exothermic peaks (Figures 59 and 60). While the enthalpies of melting and crystallization are calculated from the area under the respective peaks. The estimated quantities are enlisted in Table 12, and are in agreement with literature. [158, 160] The melting temperatures of the studied compositions lie between 394 K–406 K, while the crystallization temperatures are between 369 K and 381 K, respectively. P(VDF-TrFE-CFE) 51.3/48.7/6.2 and 59.8/40.2/7.3 samples show the highest melting temperatures (406 K), while their crystallization temperatures are 381 K and 379 K, respectively.

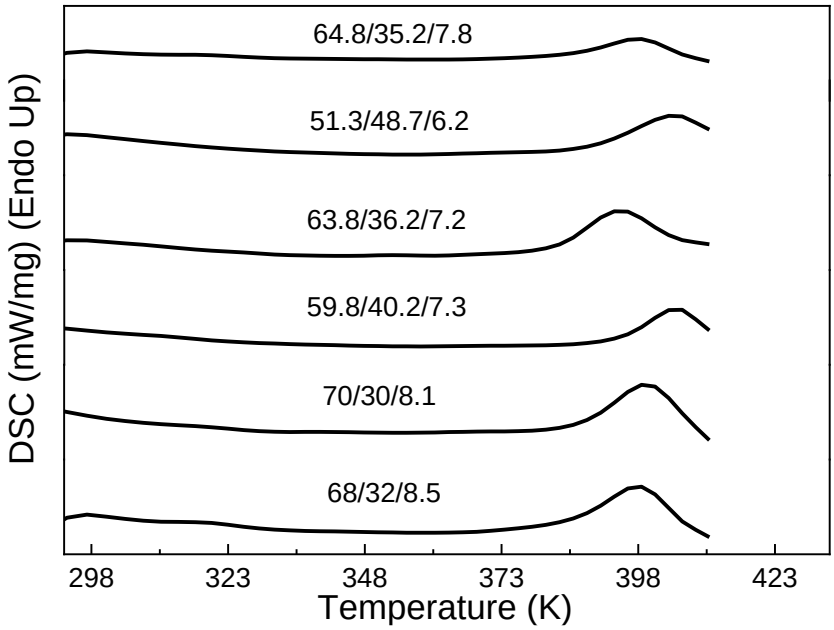

Figure 59 Heat flow curves measured by DSC upon heating where the peaks correspond to melting.

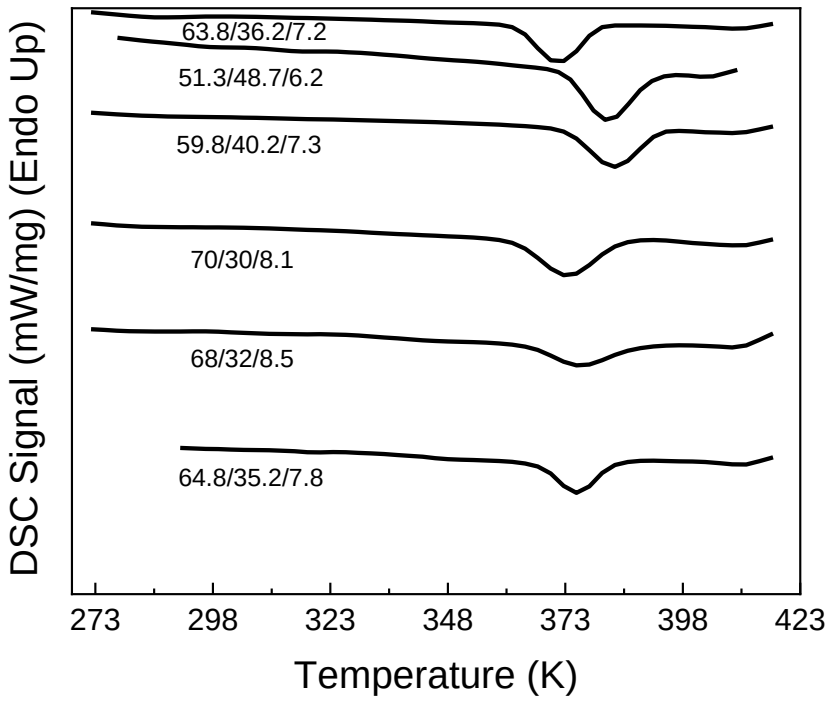

Figure 60 Heat flow curves of all studied compositions measured by DSC upon cooling where the peaks correspond to crystallization.

Table 12 The melting and recrystallization temperatures of the studied compositions and their respective enthalpies estimated from DSC measurements

$P(VDF_x\text{-}TrFE_{1-x}\text{-}CFE_y)$ (mol. %)	Melting Temperature (K)	Enthalpy of Melting (J/g)	Crystallization Temperature (K)	Enthalpy of Crystallization (J/g)
51.3/48.7/6.2	406	19.3	381	- 26.5
63.8/36.2/7.2	394	15.6	369	- 26.9
59.8/40.2/7.3	406	16.2	379	- 18.4
70/30/8.1	398	14.4	370	- 16.3
68/32/8.5	398	19.4	371	- 15.3
64.8/35.2/7.8	403	16.7	376	- 20.1

4.2.4 Relaxor Properties

In Figure 61, the temperature dependence of the dielectric permittivity and the dielectric loss tangent, measured at frequencies between 1 kHz and 1 MHz upon cooling, are shown. All studied compositions of P(VDF-TrFE-CFE) show a broad maximum of the dielectric permittivity, and the position of maxima is shifting towards higher temperature with increasing frequency. The relaxor behavior is characterized by such diffuse peaks and frequency dependent dispersion. The maximum value of the relative dielectric permittivity lies in the range of 45 to 90, which is in conjunction with previous reports. [80]

The dielectric permittivity-temperature curves are further evaluated to describe the relaxor behavior in detail. In relaxors, the slowing down polarization dynamics causes a transition into a glassy-like state with short-range correlated polarization (non-ergodic relaxor state) at the freezing temperature, T_f. The freezing temperature is assessed using the Vogel-Fulcher equation (Equation 2). In Figure 62a, an example of a Vogel-Fulcher equation fit for the P(VDF-TrFE-CFE) 68/32/8.5 film is demonstrated. The best fitting parameters for the studied samples are enlisted in Table 13. The variation of the freezing temperature for the different compositions is exhibited in Figure 62c. For the estimation of the degree of relaxor behavior, the modified Curie-Weiss law (Equation 45), is utilized to approximate the temperature dependence of $\varepsilon(T)$ above T_m. [162, 163] Figure 62b shows an example of the fit of $\varepsilon(T)$ using the Modified Curie-Weiss law for the P(VDF-TrFE-CFE) 68/32/8.5 sample. The fitting curve matches the experimental data quite well. The best fit values for γ is between 1.5 and 1.7 (Table 13), validating the strong relaxor behavior in all studied compositions of P(VDF-TrFE-CFE).

P(VDF-TrFE-CFE) 51.3/48.7/6.2 shows the highest freezing temperature 306±2 K among all studied compositions. While, the freezing temperatures of the remaining compositions lie between 278 K–288 K.

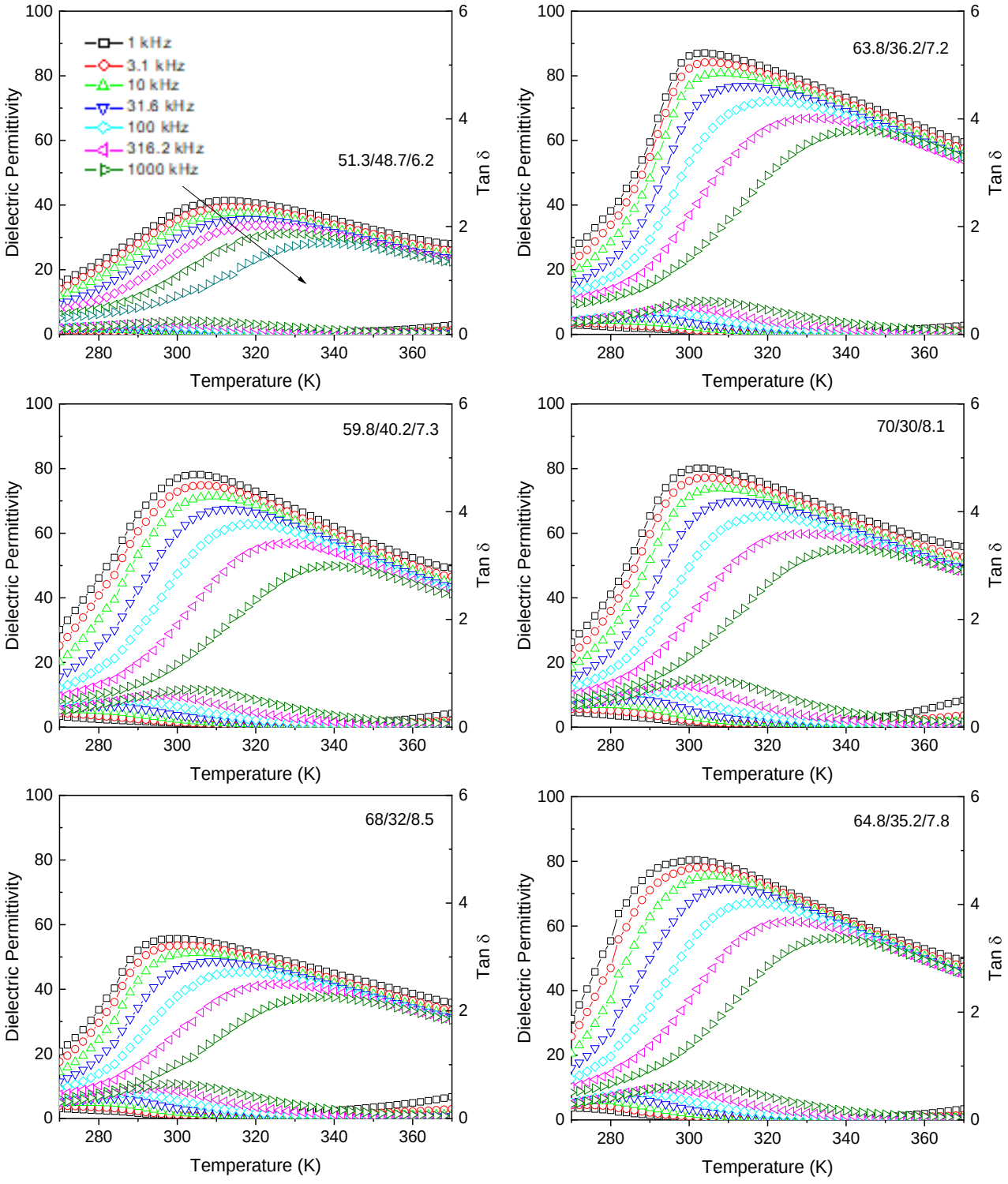

Figure 61 Temperature dependence of the dielectric permittivity and dielectric loss tangent of P(VDF-TrFE-CFE) film samples measured at varying frequencies on cooling.

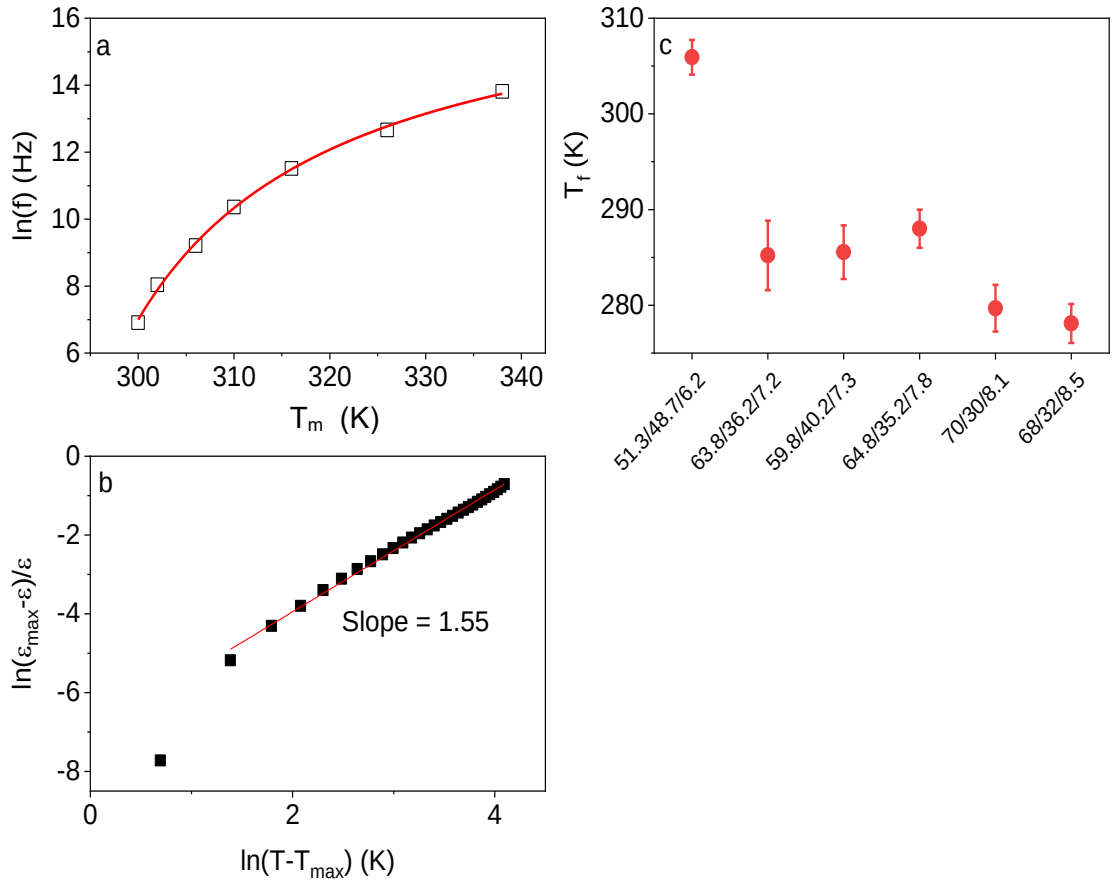

Figure 62 Examples of (a) the Vogel-Fulcher fitting, (b) the modified Curie-Weiss law fitting for the P(VDF-TrFE-CFE) 68/32/8.5 film (c) The freezing temperatures of the studied compositions.

Table 13 Parameters explaining the relaxor behavior of the studied the P(VDF_x-$TrFE_{1-x}$-CFE_y) film samples.

P(VDF_x-$TrFE_{1-x}$-CFE_y) (mol. %)	Degree of Dielectric Relaxation (γ)	Freezing Temperature (K)	Fitting Parameters for the Vogel-Fulcher Equation	
			ln(f_0)	E_a (meV)
51.3/48.7/6.2	1.61	306 ± 2	15.8 ± 0.9	6 ± 2
63.8/36.2/7.2	1.52	285 ± 4	16.3 ± 0.8	14 ± 4
59.8/40.2/7.3	1.64	286 ± 3	17.3 ± 0.7	16 ± 4
64.8/35.2/7.8	1.61	288 ± 2	16.3 ± 0.4	11 ± 2
70/30/8.1	1.50	280 ± 2	17.5 ± 0.5	21 ± 3
68/32/8.5	1.55	278 ± 2	17.6 ± 0.5	20 ± 3

4.2.5 Polarization Hysteresis Behavior

In Figure 63, the polarization hysteresis loops measured upon cooling are shown. The 59.8/40.2/7.3 terpolymer shows slim polarization hysteresis loops, which is typical for relaxors. A distinct feature of other compositions is the sudden increase of the polarization above a certain electric field value, named as critical field (E_{cr}), which introduces the DHL shape (Figure 63). Such DHL-shape has been already observed for some P(VDF-TrFE-CFE) polymers, e.g. for 59.2/33.6/7.2 (notated as P(VDF_x-$TrFE_{1-x}$-CFE_y) 63.8/36.2/7.8). The DHL has been explained in terms of a reversible, electric field-induced relaxor to ferroelectric phase transition. [54]

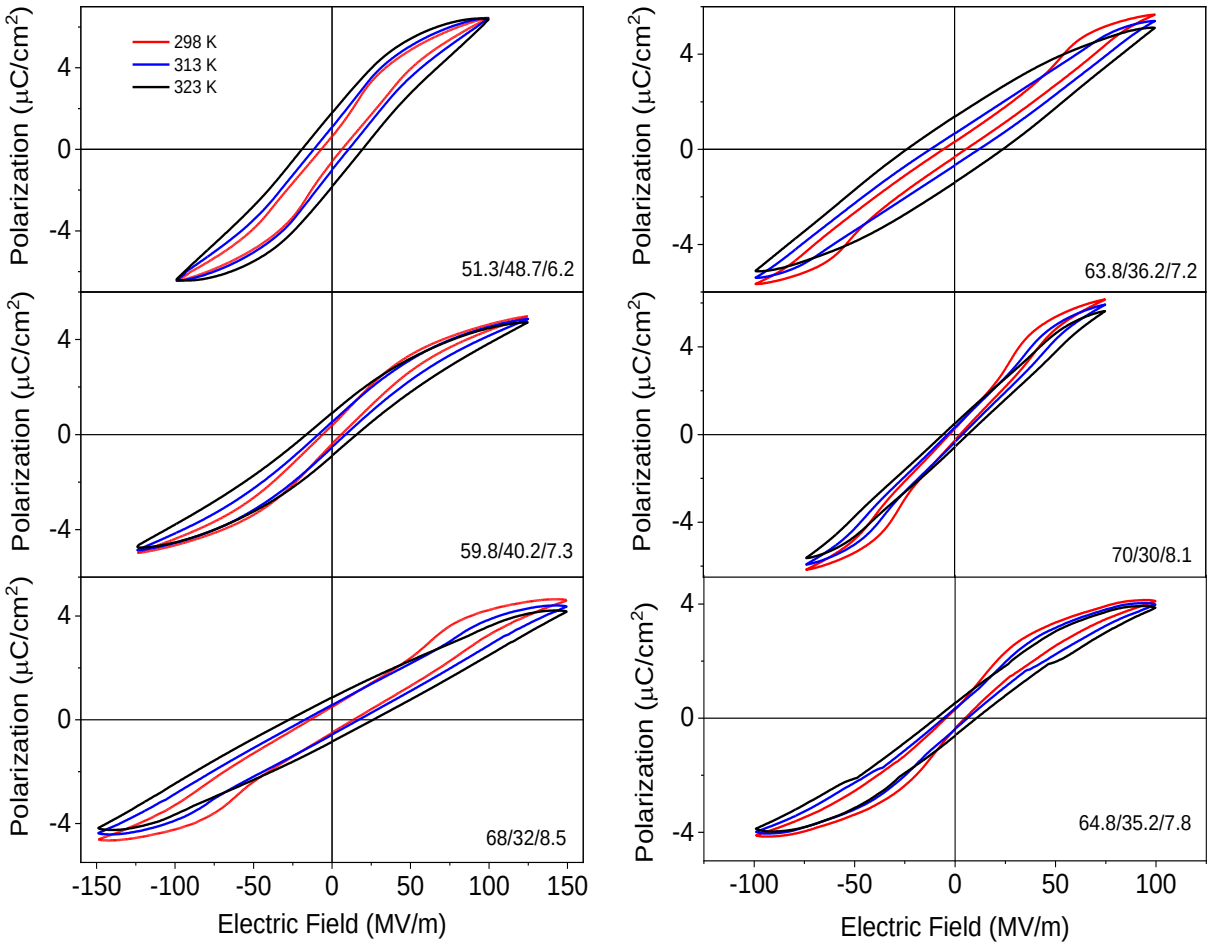

Figure 63 Polarization hysteresis loops measured as a function of temperature under triangular wave of 10 Hz on cooling.

The polarization curves shown in Figure 63 are assessed in detail to evaluate the critical fields corresponding to the reversible transition to the ferroelectric state, E_1, followed by the transition back to the relaxor state, E_2. The values of the critical fields are estimated from the minima (E_1) and maxima (E_2) of the derivative of polarization with respect to electric field. The temperature dependences of E_1 and E_2 for the studied compositions are demonstrated in Figure 64. It is clear from Figure 64 that the P(VDF-TrFE-CFE) 63.8/36.2/7.2 and P(VDF-TrFE-CFE) 68/32/8.5 samples have the largest critical field values, (E_1 = 80 – 90 MV/m) at room temperature; while for the P(VDF-TrFE-CFE) 51.3/48.7/6.2, the transition to the ferroelectric state occurs already at 40 MV/m. For all the studied compositions, both E_1 and E_2 increase with temperature, except for P(VDF-TrFE-CFE) 51.3/48.7/6.2, where E_1 slightly decreases upon heating.

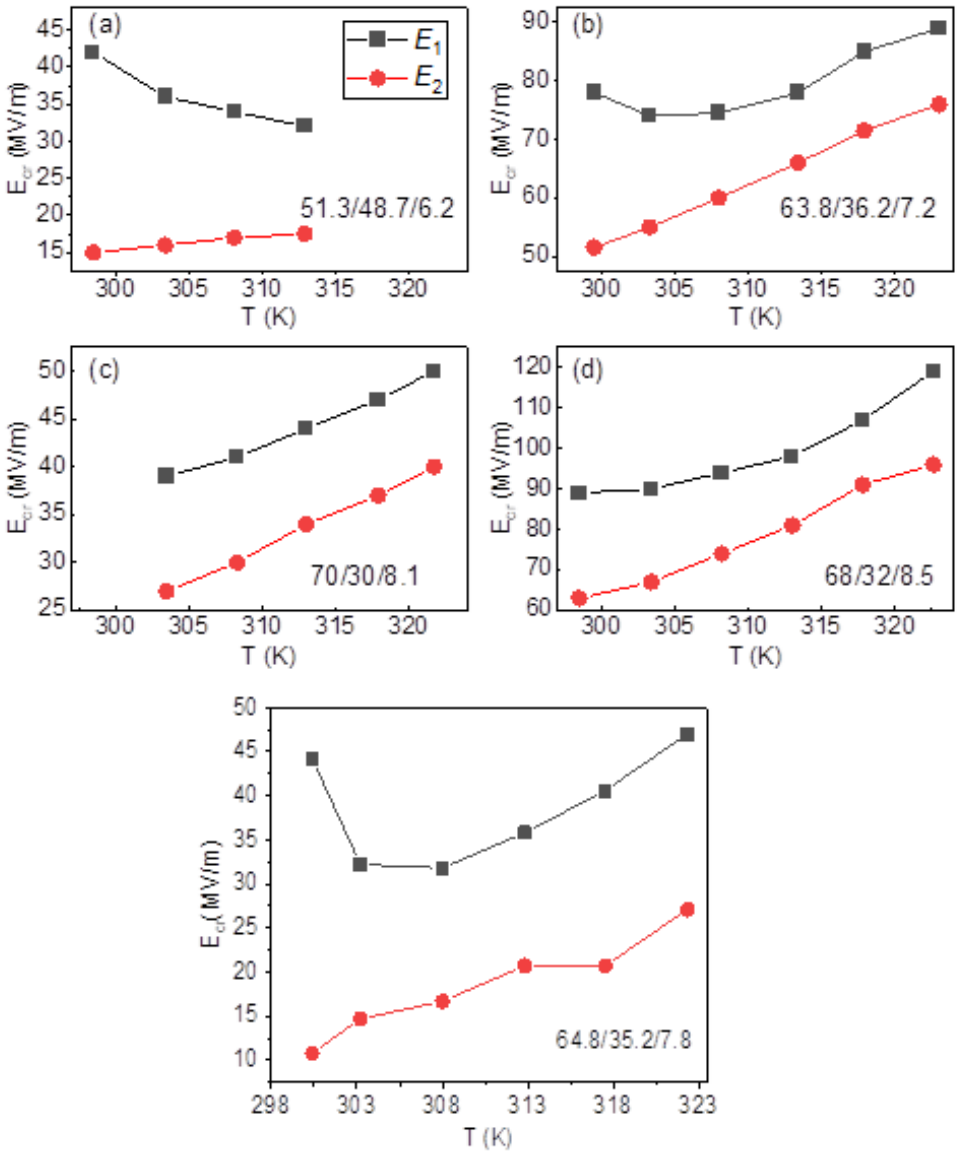

Figure 64 The critical fields, E_1 and E_2, corresponding to the field induced transitions between relaxor and ferroelectric states as a function of temperature for P(VDF-TrFE-CFE) terpolymers.

Referring to the field induced relaxor-ferroelectric transition in inorganic relaxors, such as $(Pb,La)(Zr,Ti)O_3$ [169] or $Na_{0.5}Bi_{0.5}TiO_3$-$BaTiO_3$, [170], it is observed that the critical field value increases with temperature in the ergodic relaxor state, but decreases with temperature in the non-ergodic relaxor state. The non-ergodic relaxor state is the state below the freezing temperature, where the interaction between PNRs hinders their reorientation and related dynamics. From the analysis of the dielectric data, the freezing temperature of the P(VDF-TrFE-CFE) 51.3/48.7/6.2 sample is calculated as 306 K. In Figure 64, it is clear that the temperature range where DHL is observed (critical field) lies around the transition from the non-ergodic to the ergodic relaxor state. All other compositions have a comparatively low freezing temperature compared to the 51.3/48.7/6.2 sample.

As already mentioned, the relaxor behavior in P(VDF-TrFE-CFE) is promoted by the incorporation of bulky CFE monomers. An analogy can be established between the CFE monomers having their own dipole moment serving as dipole defect pinning centers, and dipole defects built by oxygen vacancies and acceptor impurities in perovskite ferroelectrics. [171] When the magnitude of the applied electric field is large enough, the dipoles of CFE may rotate which favors the switching of the surrounding dipoles and the formation of a ferroelectric state with large domains. [166] These FE domains transform back to the relaxor phase with decreasing electric field (Figure 63). The PNR movements in the ergodic relaxor state are unimpeded, and they are relatively free to rotate and can be easily aligned. But with increasing temperature, the thermal agitation interrupts this alignment and therefore the critical field, E_1, increases upon heating. In the non-ergodic relaxor state, the PNRs are frozen, and it is relatively difficult to reorient them. The PNRs become more dynamic on approaching the freezing temperature, therefore the critical field decreases upon heating for P(VDF-TrFE-CFE) 51.3/48.7/6.2. The DHL vanishes with temperature (Figure 63), since the polymer chains become mobile with temperature, and the pinning effect due to the presence of the CFE monomers in the polymer chain becomes less prominent. But this process is also obscured by the broadening of the hysteresis loops due to the increasing leakage current.

Another distinct feature of the polarization hysteresis loops in all studied samples is the broadening of the hysteresis loops with temperature, which results in an increase in the measured values of the remnant polarization as well as the coercive field. This broadening is caused by the leakage current which becomes pronounced with temperature, as evident in the dielectric loss curves at low

frequency (1 kHz) in Figure 61. In the case of polymers, the field induced transport of electronic and ionic charges is the main reason of the leakage current. [172] This increase of the extrinsic polarization has been considered as a signature of a negative electrocaloric effect (ECE) calculated through the indirect method in a few published reports. [17–19] Whereas, the direct electrocaloric measurements of similar compositions show a positive electrocaloric effect. [13, 112] Hence, the extrinsic contribution to the polarization due to the leakage current may lead to an inaccurate evaluation of the electrocaloric effect in ferroelectric and relaxor polymers.

4.2.6 Electromechanical Properties

The electromechanical properties of P(VDF-TrFE-CFE) are studied in all compositions. The voltage dependent displacement curves are measured using a bipolar triangular wave function at 10 Hz. The amplitude of the applied voltage is 1500 V. The electrostrictive strain given in Table 14 is calculated by dividing the maximum displacement by the total thickness of the free-standing film, which is 20 µm. The negative strain values in Figure 65 show that the sample contracts parallel to the direction of the applied electric field. Among all studied compositions, P(VDF-TrFE-CFE) 51.3/48.7/6.2 shows a significant hysteresis, whereas 70/30/8.1 shows a minimum hysteresis. P(VDF-TrFE-CFE) 63.8/36.2/7.2 and 68/32/8.5 show unsaturated curves, but they still exhibit 0.5 % strain. The maximum strain of 1 % is observed in P(VDF-TrFE-CFE) 59.8/40.2/7.3 and 64.8/35.2/7.8. [167, 173]

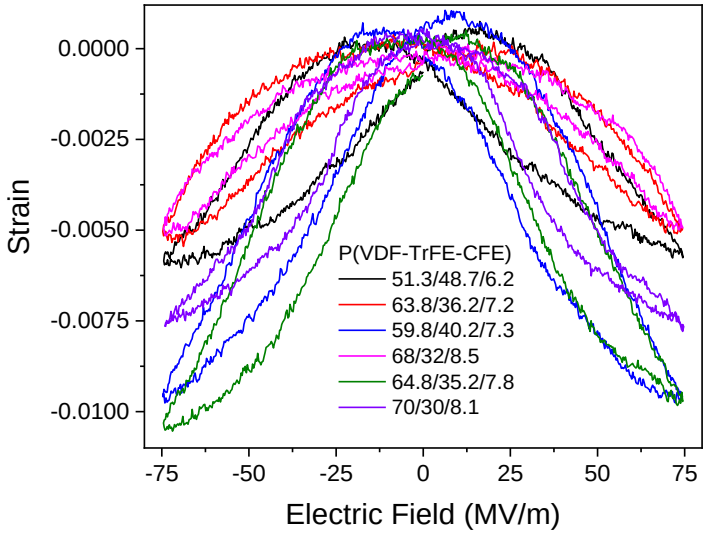

Figure 65 Strain–electric field loops of the studied terpolymer compositions.

Table 14 Comparison of electromechanical properties of the different P(VDF-TrFE-CFE) compositions.

$P(VDF_x\text{-}TrFE_{1-x}\text{-}CFE_y)$ (mol. %)	Maximum Displacement (nm)	Maximum Electrostrictive Strain (%)
51.3/48.7/6.2	112 ± 5	0.60
63.8/36.2/7.2	99 ± 5	0.50
59.8/40.2/7.3	194 ± 10	1.0
70/30/8.1	153 ± 7	0.80
68/32/8.5	100 ± 5	0.50
64.8/35.2/7.8	196 ± 10	1.0

4.2.7 Energy Storage Properties

The energy storage properties of all compositions are investigated using the polarization-based method. The hysteresis loops are recorded using a triangular unipolar wave function at a frequency of 10 Hz. In Figure 66, the unipolar $P - E$ loops of all studied compositions are shown. These loops are then analyzed using the method already described in Section 2.3.3.1.

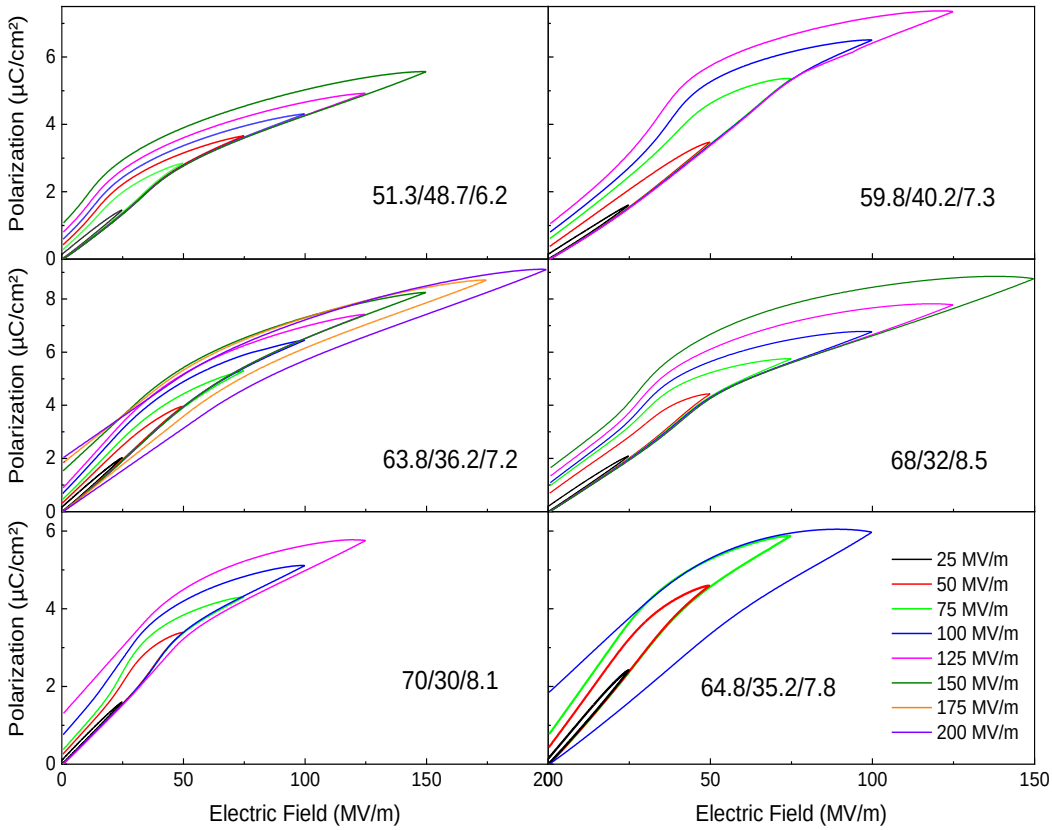

Figure 66 Unipolar polarization hysteresis curves measured as a function of voltage at room temperature.

Figure 67 shows the discharged energy density and the charge-discharge efficiency estimated through Equations 24 & 26. It can be seen in Figure 67 that there is a linear increase in the discharged-energy density of all compositions with the electric field. Conversely, the energy storage efficiency drops as the amplitude of the electric field is increased. Hence, it is obvious that there is a tradeoff between the discharged energy density and the energy storage efficiency. This tradeoff is due to the hysteresis and conduction losses, which become more prominent at a higher electric field. In Figure 67, it is evident that the P(VDF-TrFE-CFE) = 59.8/40.2/7.3 sample shows the highest discharged energy density and the highest energy storage efficiency among all compositions. Since the P(VDF-TrFE-CFE) 59.8/40.2/7.3 sample does not exhibit a double hysteresis loop, the losses remain very low. The discharged energy density of P(VDF-TrFE-CFE) 59.8/40.2/7.3 reaches ~ 5 J/cm^3 and maintains a charge-discharge efficiency of 63%, when the applied electric field is 200 MV/m.

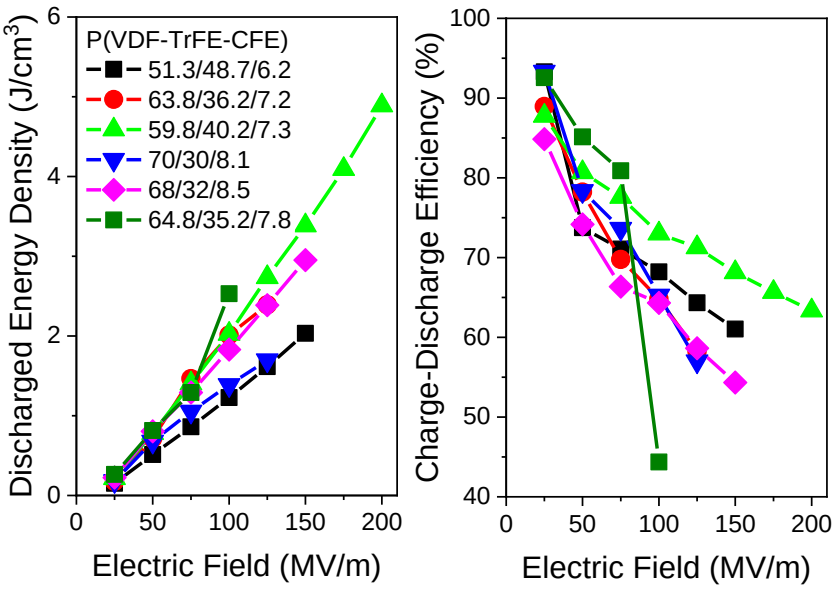

Figure 67 The discharge energy densities (left) and charge-discharge efficiencies (right) plotted against maximum applied electric field.

Table 15 shows the stored energy density, discharged density and charge-discharge efficiency of all compositions at 100 MV/m. The stored energy density comprises of the discharged energy density and the losses. It can be noticed that P(VDF-TrFE-CFE) 64.8/35.2/7.8 has the highest stored energy density, but the charge-discharge efficiency is very low due to a large hysteresis and conduction losses. The discharged energy densities of all the studied compositions at 100 MV/m remain between 1.23 –2.53 J/cm^3, which is in good agreement with similar compositions as previously reported in the literature. [149, 150]

Table 15 Comparison of electrical energy storage properties of all studied compositions at 100 MV/m.

$P(VDF_x\text{-}TrFE_{1-x}\text{-}CFE_y)$ (mol. %)	Stored Energy Density (U_{stored}) (J/cm^3)	Discharged Energy Density ($U_{discharged}$) (J/cm^3)	Charge-Discharge Efficiency (η) (%)
	At 100 MV/m		
51.3/48.7/6.2	1.80	1.23	68.2
63.8/36.2/7.2	3.10	2.01	64.8
59.8/40.2/7.3	2.87	2.02	73.0
70/30/8.1	2.12	1.39	65.2

68/32/8.5	2.84	1.83	64.3
64.8/35.2/7.8	5.72	2.53	44.37

4.2.8 Conclusion

The crystal structure, thermophysical properties, dielectric, polarization and electromechanical properties of six different compositions of P(VDF-TrFE-CFE) polymers are compared. All compositions show a peak in XRD at 17.8°, which corresponds to the α non–polar crystal structure. The thermophysical properties of the studied compositions of P(VDF–TrFE–CFE) are almost the same. All compositions show a similar degree of relaxor behavior. The freezing temperature is decreased with increasing CFE content, and the ergodic relaxor state is stabilized at room temperature. The freezing temperature of all compositions is far below room temperature, except for P(VDF-TrFE-CFE) 51.3/48.7/6.2. The ergodic relaxor state at room temperature allows to use the Maxwell relations for the indirect estimation of the electrocaloric effect in these compositions, however the leakage current is a problem in getting reliable values.

At a critical applied electric field, transition into a ferroelectric state is induced, which is manifested in double hysteresis loops in all compositions, except for P(VDF-TrFE-CFE) 59.8/40.2/7.3. The value of the critical electric field depends on the proximity to the freezing temperature.

The characteristics of the polymer films for energy storage and piezoelectric applications are examined. A maximum energy density of 5 J/cm^3 at 63% charge–discharge efficiency and a field of 200 MV/m is observed for the new composition P(VDF-TrFE-CFE) 59.8/40.2/7.3 owing to a slim single hysteresis loop. P(VDF-TrFE-CFE) 59.8/40.2/7.3 and 64.8/35.2/7.8 show the highest electrostrictive strain values among all compositions i.e. ~ 1% at 75 MV/m.

4.3 Electrocaloric Effect in P(VDF-TrFE-CFE)

In this section, the electrocaloric temperature change in three different P(VDF-TrFE-CFE) compositions, namely, 64.8/35.2/7.8, 59.8/40.2/7.3 and 68/32/8.5 is directly measured using the quasi-adiabatic calorimeter. The magnitudes of the electric field are 50 MV/m and 75 MV/m, which is either below or above the critical electric field for the corresponding compositions. The pulse of the applied voltage is also analyzed to address the issue of the Joule heating in films, and to discern Joule heating from the electrocaloric effect.

Another issue that is discussed in this section is the specious negative or inverse electrocaloric effect, observed through the indirect measurements in the P(VDF) based systems. A negative electrocaloric effect in P(VDF) based systems through direct measurements has not been observed yet. Therefore, a systematic analysis of the indirect method of the electrocaloric measurement in P(VDF-TrFE-CFE) 64.8/35.2/7.8 is performed. The $P - E$ hysteresis loops are measured as a function of temperature with and without compensating the leakage current in the sample. The electrocaloric effect is studied using both, bipolar and unipolar field cycling. The effect of frequency on the indirect electrocaloric temperature change is analyzed. Finally, the direct and indirect electrocaloric methods are compared.

4.3.1 Pulse Shape for Direct Electrocaloric Measurement

For the direct electrocaloric measurement, different forms of electric pulses can be used, such as rectangular, slanted step, saw, and short pulse, which are depicted in Figure 68. The shape of the electric pulse is dependent on the slew rate, which is the rate of change of applied or removed voltage and the duration of the applied voltage.

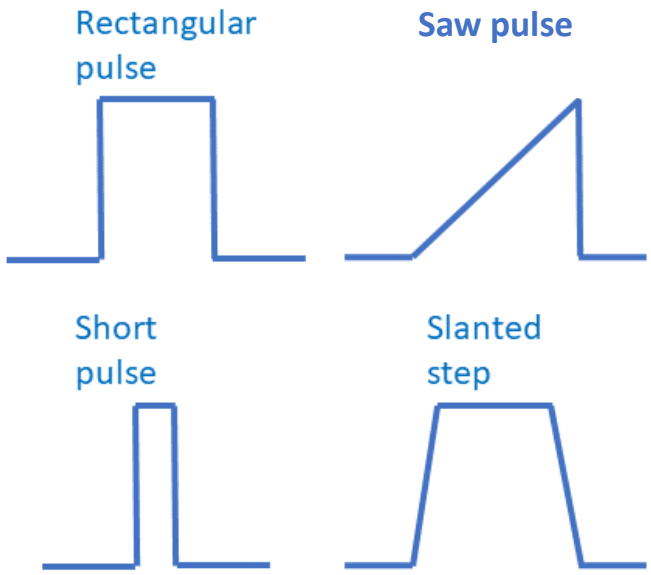

Figure 68 Various voltage-time profiles of electric pulses.

The most widely used electric pulse signal for the direct *EC* measurements is the rectangular pulse, where the field-on and field-off ramps are symmetric. [10] Electrocaloric measurements using a quasi-adiabatic calorimeter in literature were performed under a rectangular step *DC* pulse, where the slew rate for field on (E_{on}) and field off (E_{off}) was 50 kV/s, while the pulse duration was 100 s. [83] Under a rectangular pulse, the *EC* temperature change is determined from the *EC* heating as well as cooling i.e. when the field is applied and removed, respectively. [83] The rectangular pulse shape is advantageous to determine, whether the *EC* effect is symmetric or not reversible due to the Joule heating. [10, 102] Direct *EC* measurements performed using a rectangular pulse in the free-standing films of P(VDF-TrFE) have been reported, where the duration of the pulse was chosen to be long enough to allow the samples to get into a thermal equilibrium with the surrounding bath. [85, 112, 114] However, in the case of soft polymer films and their nanocomposites, the large amplitude of

applied electric field for a long duration causes significant Joule heating, and increases the probability of a dielectric breakdown. [10]

For the P(VDF–TrFE) 55/45 copolymer film, which was 20 µm in thickness and 6 mm in diameter, a measured leakage current of $2.5 \times 10^{-10} A$ at 50 MV/m at room temperature is reported, and the Joule heat was calculated to be $4.3 \times 10^{-7} J$. [114] Guo et al. studied P(VDF-TrFE-CFE) 62.6/29.4/8 and observed a leakage current in the range of 10 nA – 30 nA under a maximum applied electric field of 67 MV/m. [85] In this work, the leakage current in the 20 µm thick P(VDF-TrFE-CFE) 64.8/35.2/7.8 sample having 4 mm (silver) electrode diameter at room temperature and 75 MV/m is measured to be $3.2 \times 10^{-6} A$, and the calculated Joule heat is 72 mJ.

The large amplitude of the applied voltage (V) on the polymer films may lead to significant Joule heating, which is linearly dependent on time (t) and current (I), according to the relation $Q = VIt$, and can even surpass the EC temperature change. To obtain a reliable EC response in P(VDF-TrFE-CFE) free-standing thick films, it is deemed imperative to analyze the effect of the shape of the electric pulse. As to discern between the two competing temperature changes (EC and Joule heating) under an electric field, it has been proposed to apply saw shaped electric pulses with a slow slew rate for E_{on} and the fast slew rate for E_{off}, so that the rapid EC cooling can be distinguished from the gradual temperature decay arising from the slower release of the Joule heat (produced under the applied electric field) into the bath. [10] Following this concept, a saw shaped electric pulse is used for the direct EC measurement in the terpolymer film sample. In Figure 69, a saw shaped electric pulse with a slow field-on ramp (E_{on} = 0.1 kV/s) and a fast field-off ramp (E_{off} = 100 kV/s) is shown. The duration of the maximum applied electric field (E_{max}) is set as 0.1 s, which is longer than both, i.e. the response time of the thermocouple, and the polarization switching time which is usually of the order of 10 µs. [10] The rapid EC temperature drop (ΔT) when the field is switched off can be clearly distinguished from the slower release of the Joule heat into the surrounding bath (Figure 69). Here, the external relaxation can be deemed as an exponential heat dissipation having a characteristic relaxation time as given in equation 46. [114]

$$T(t) = T_{bath} + \Delta T e^{-t/\tau} \tag{46}$$

Where τ represents the relaxation time constant and its value in this case is 12.5 s ± 0.3 s. Thus, by calculating and subtracting the long-term relaxation process, the magnitude of the ECE in the sample can be discerned from the Joule heat.

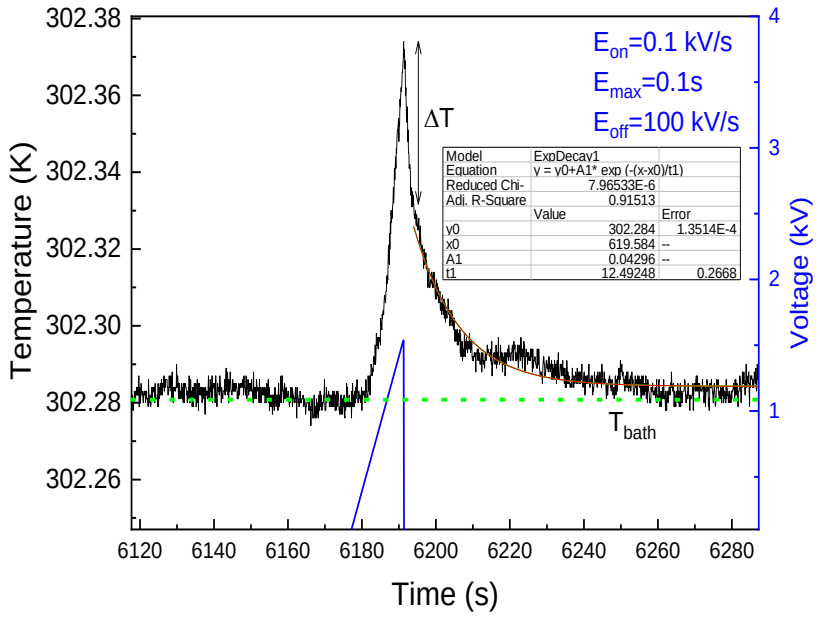

Figure 69 Profile of electric pulse applied during the electrocaloric measurement of the P(VDF–TrFE–CFE) film in the quasi-adiabatic calorimeter (Fitting parameters to Equation 46 are given in the inset).

4.3.2 Direct Electrocaloric Measurement

The electrocaloric effect in three different compositions of neat P(VDF-TrFE-CFE), namely 59.8/40.2/7.3, 68/32/8.5, and 64.8/35.2/7.8 under a moderate electric field (50 V/μm and 75 V/μm) is directly measured, as shown in Figure 70a. For all three compositions, the electrocaloric temperature change increases as the amplitude of the applied voltage increases. The maximum ΔT_{EC} = 1.8 K is observed in P(VDF-TrFE-CFE) 64.8/35.2/7.8 at 301 K, which is in a similar range as previous reports, where the electrocaloric temperature change was measured using an infrared camera. [85, 86] However, when comparing the ΔT_{EC} values of the other two compositions (59.8/40.2/7.3 and 68/32/8.5) with P(VDF-TrFE-CFE) 64.8/35.2/7.8, it is clearly visible that the electrocaloric effect in 59.8/40.2/7.3 and 68/32/8.5 is much lower under the same magnitude of the applied electric field and measuring temperature. This lower electrocaloric effect can be explained in terms of the *P* – *E* loops measured under a bipolar field of 10 Hz and 75 MV/m, shown in Figure 70b. The *P* – *E* loop of the 64.8/35.2/7.8 sample has a double hysteresis loop and 59.8/40.2/7.3 shows a slim hysteresis loop, both are typical for relaxors. While *P* – *E* loop of 68/32/8.5 at 75 MV/m gives a notion of a paraelectric phase, all measured at the same frequency (10 Hz). It is clear from Figure 70b, that the P(VDF–TrFE–CFE) 64.8/35.2/7.8 composition undergoes a field induced phase transition, while 59.8/40.2/7.3 does not show such behavior, as already discussed in detail in Section 4.2.5.

On a microscopic level, the electrocaloric effect is generated due to the orientation of the dipoles in the direction of the electric field. Therefore, it is reasonable to say that the appearance of a paraelectric like loop 68/32/8.5 at 75 MV/m can be attributed to the amplitude of the applied electric field which is not high enough to cause the chain rotation and induce a phase transition, and ultimately results in low values of the electrocaloric temperature change. P(VDF-TrFE-CFE) 64.8/35.2/7.8 shows a field induced phase transition which plausibly results in a higher electrocaloric coefficient value due to the enthalpy of transition. 59.8/40.2/7.3 shows a low electrocaloric effect due to a single hysteresis loop.

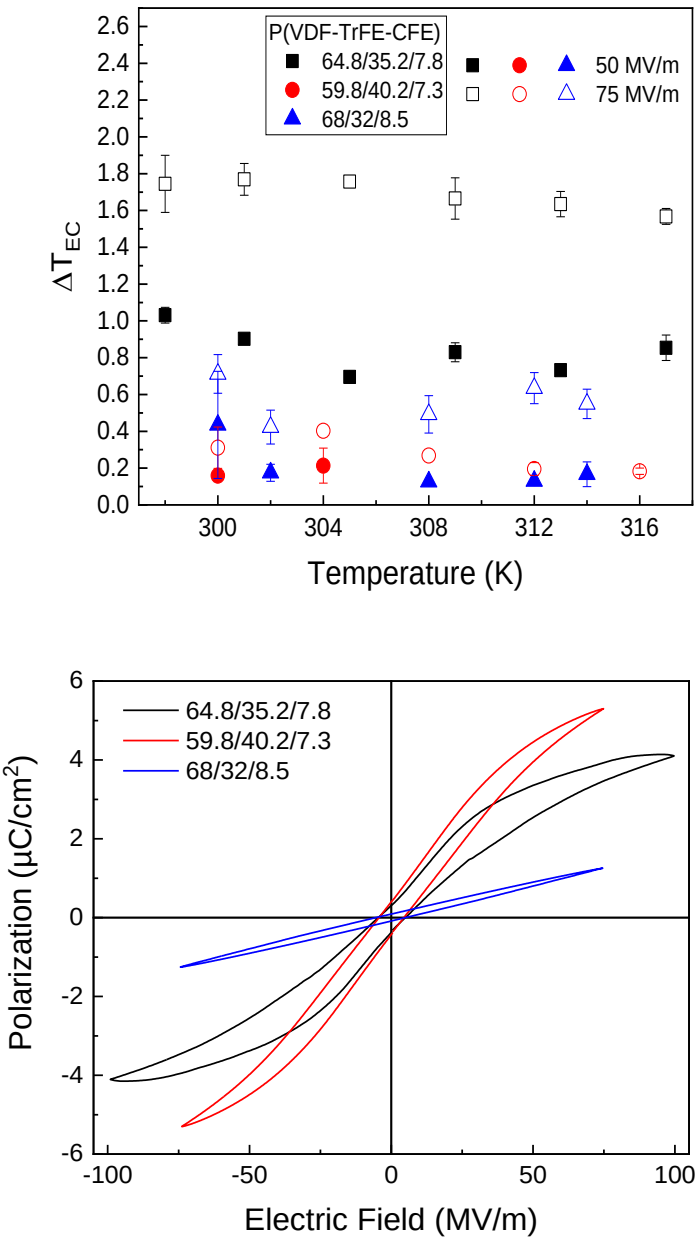

Figure 70 (a) Directly measured electrocaloric temperature change in three different compositions of P(VDF-TrFE-CFE) (64.8/35.2/7.8), 59.8/40.2/7.3 & 68/32/8.5, (b) P – E loops of the same compositions measured at room temperature.

4.3.3 Indirect Electrocaloric Measurement

The indirect method is analyzed in detail to understand the reason behind the specious negative electrocaloric effect, observed through the indirect method, in a few reported works. [17–19] The electrocaloric temperature change is indirectly estimated in P(VDF-TrFE-CFE) 64.8/35.2/7.8 and compared to the directly measured values. The indirect measurement is conducted via the widely used procedure, where the bipolar electric field is used and the polarization values from the discharging branch in the first quadrant of the *P – E* loop at different temperatures and electric fields are analyzed. The electrocaloric temperature change is then deduced by employing the Maxwell relations (Equations 11 and 12).

In Figure 71, the polarization hysteresis loops of P(VDF-TrFE-CFE) 64.8/35.2/7.8 are measured at 10 Hz and used to estimate the indirect electrocaloric temperature change at 50 MV/m and 75 MV/m. In Figure 71, the change of polarization with respect to temperature and electric field is shown. The polarization at 0 MV/m, which is the remnant polarization *(P_r),* increases gradually between 40°C and 50°C, giving a positive slope of $\frac{\partial P}{\partial T}$. While the polarization values between 15 MV/m and 75 MV/m have a negative or zero $\frac{\partial P}{\partial T}$ slope. As already discussed in Section 2.2.2.1, in the indirect method, the $\frac{\partial P}{\partial T}$ slope at a given electric field (isofield) has a key role in determining the sign of the electrocaloric effect, and it is significantly influenced by the leakage contribution which becomes pronounced with increasing temperature. Therefore, the indirect method must be validated using the direct method to obtain reliable results of the electrocaloric temperature change.

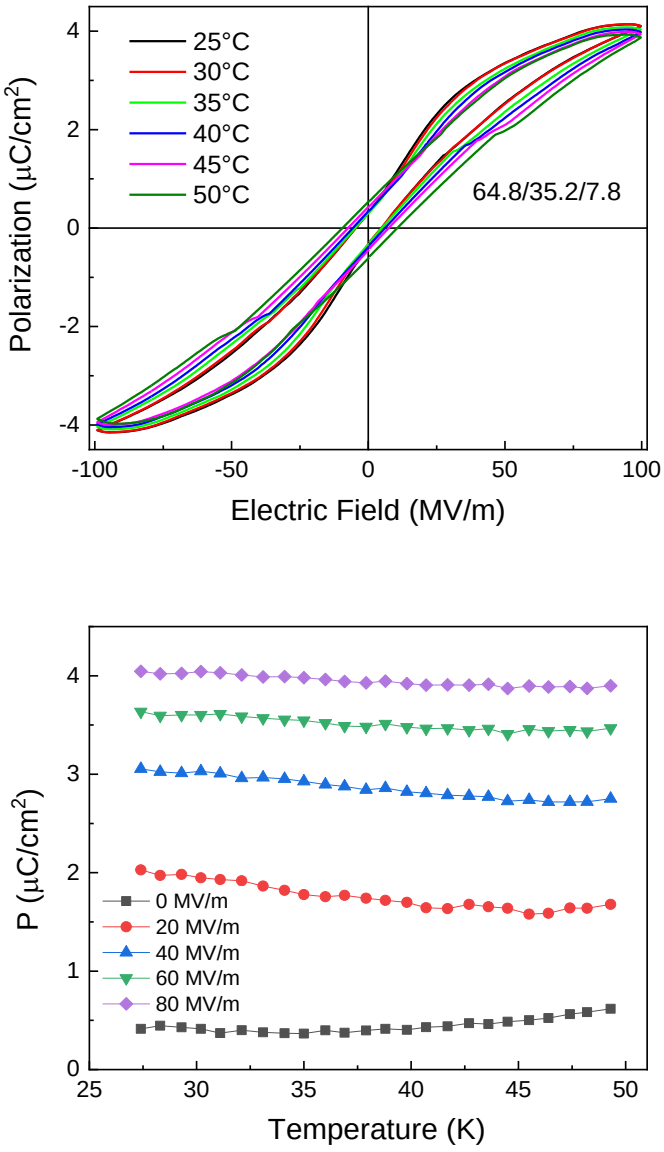

Figure 71 Polarization hysteresis loop of P(VDF–TrFE–CFE) 64.8/35.2/7.8 measured at 10 Hz as a function of temperature (top), polarization values extracted from the discharge loop at different temperatures and electric fields (bottom).

Figure 72 presents a comparison between the indirect and the direct measurement of the electrocaloric temperature change in P(VDF-TrFE-CFE) 64.8/35.2/7.8, at 50 MV/m and 75 MV/m, within a temperature range of 298 K – 323 K. It can be seen that the indirectly deduced values of the electrocaloric temperature change are negative between 298 K and 315 K for both electric fields. At 318 K, the electrocaloric temperature change estimated at 50 MV/m remains negative, while at

75 MV/m the value of the electrocaloric temperature change becomes positive. At 323 K, the indirect electrocaloric temperature change is positive and jumps to a higher value. The directly measured electrocaloric temperature change via the quasi-adiabatic calorimeter is presented in Figure 72 as well. The notable feature is that the directly measured electrocaloric temperature change values are positive in the entire measuring temperature range (298 K – 318 K) at both measuring electric fields (50 MV/m and 75 MV/m). Evaluating the indirect and direct methods (Figure 72), it can be observed that the electrocaloric temperature change values obtained through the two methods are not in agreement. The indirectly estimated electrocaloric temperature change values that are positive at 323 K, and at 318 K and 75 MV/m, have a huge variation and are either too low or too high compared to the directly measured values. As discussed earlier, the plausible reason for the specious "negative" electrocaloric effect through the indirect method can be the extrinsic leakage current contribution. Therefore, the effect of leakage current on the hysteresis loop and ultimately on the electrocaloric effect is studied in detail and will be discussed in the upcoming sections.

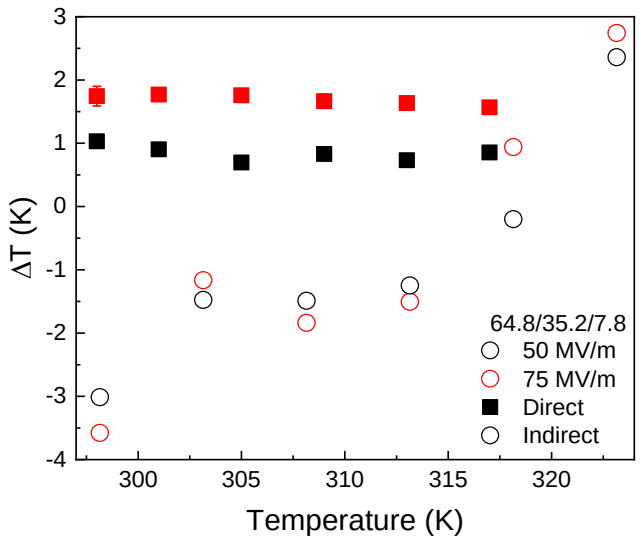

Figure 72 Indirect (circles) of electrocaloric effect calculated using the polarization loops shown in Figure 71 in P(VDF–TrFE–CFE) 64.8/35.2/7.8 & direct measurement (squares).

4.3.3.1 Leakage Current Compensation

As already discussed, the leakage current in the ferroelectric polymers may lead to erroneous results of the electrocaloric temperature change. Therefore, to study the effect of the leakage current on the polarization hysteresis loop, the built-in function of the *Aixacct* device which compensates the leakage current of the sample, is utilized. The leakage current compensation procedure has been explained in detail in Section 3.2.2.1.1.

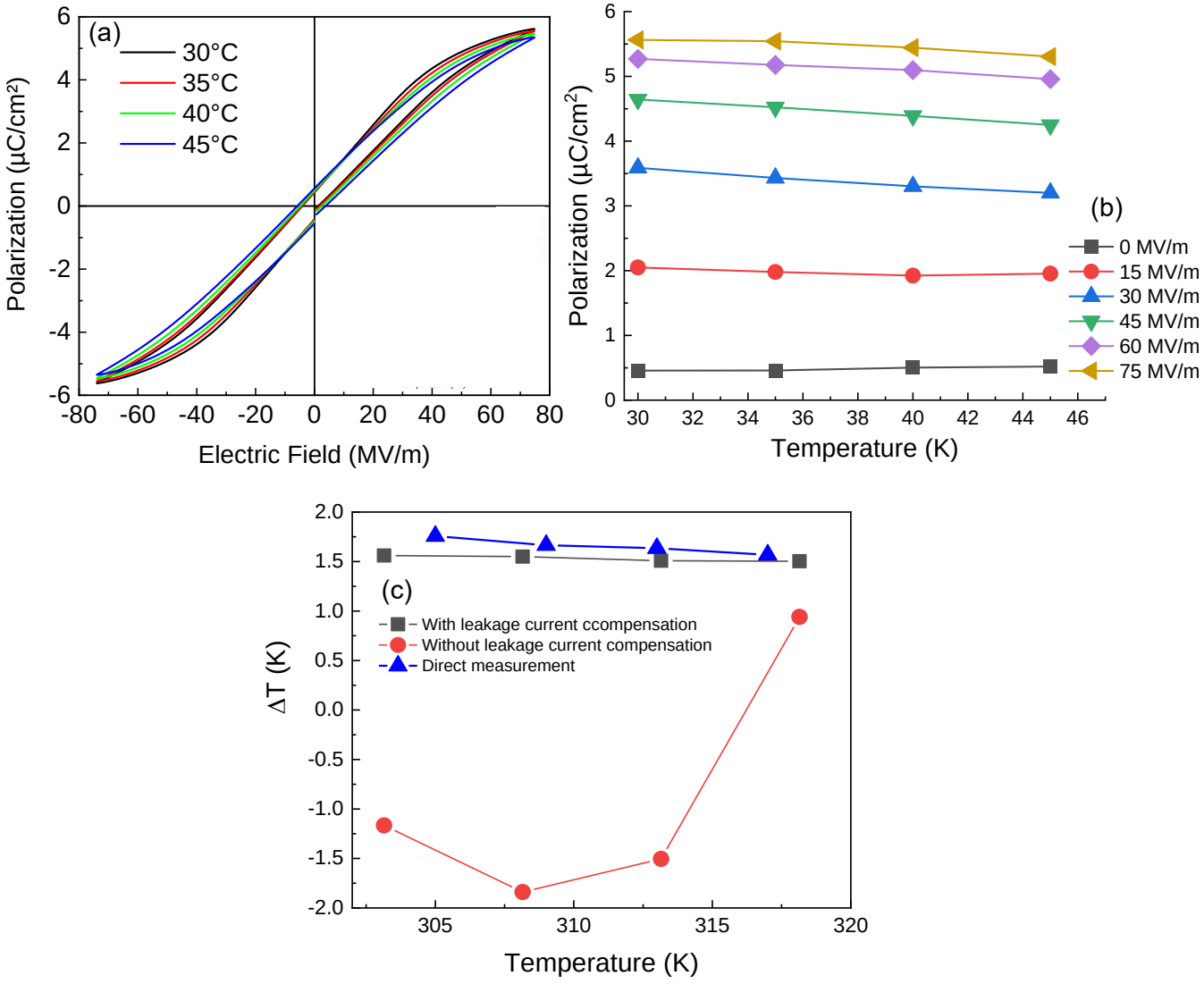

Figure 73 Polarization hysteresis loops measured under bipolar field at 10 Hz with leakage current compensation as a function of temperature of P(VDF–TrFE–CFE) 64.8/35.2/7.8 (a), extracted polarization values from the discharge branch (b), and indirectly calculated electrocaloric effect with & without leakage current compensation (c).

The *P – E* hysteresis loops of P(VDF-TrFE-CFE) shown in Figure 73(a) are measured at 10 Hz under a bipolar electric field to establish a comparison with the measurement performed without the leakage current compensation. As shown in Figure 73(b), the remnant polarization remains almost constant with temperature, while the polarization values at a higher electric field gradually decrease with increasing temperature giving a negative $\frac{\partial P}{\partial T}$ slope under an isofield. Hence, the calculated electrocaloric temperature change according to the Maxwell relation (Equation 11) has a positive sign as shown in Figure 73(c).

In Figure 73(c), the indirect electrocaloric temperature change values at 75 MV/m are presented, which are calculated using the *P – E* loops (10 Hz and bipolar field) with and without compensating the leakage current of the sample, and compared to the directly measured electrocaloric temperature change. It is confirmed that the leakage current is a leading source of error in the indirect electrocaloric measurement. Furthermore, it is clear in Figure 73 that the leakage current compensation drastically improves the reliability of the indirect method. This leads to the conclusion that the reports on a negative electrocaloric effect in P(VDF) and its copolymers measured through the indirect method are fundamentally an outcome of a measurement artifact. Additionally, when the direct and indirect methods are compared, it is evident that the positive ΔT_{EC} values deduced without compensating for the leakage current have a significant variation to the directly measured ΔT_{EC}. While the leakage current compensated *P – E* loops produce more accurate ΔT_{EC} values, which are comparable to the ones obtained through the direct method. Thus, it is inferred that the *P – E* loops measured with the leakage current compensation give a better comparison between the direct and indirect methods.

4.3.3.2 Unipolar Electric Field

The usual procedure to deduce the ΔT_{EC} through the indirect method is using a bipolar field to measure the $P-E$ loops as a function of temperature. However, in a recent report, another variant of the procedure has been introduced. Chen et al. presented an analysis of the indirect method in the context of a unipolar and a bipolar electric field, and its validity in P(VDF-TrFE), and found out that the unipolar field results are comparable to the direct measurements. [22] However, in P(VDF-TrFE-CFE), the effect of unipolar and bipolar field on the indirect method has not been reported yet, to the best of author's knowledge.

The $P-E$ loops are measured under a unipolar field of 10 Hz with and without compensating the leakage current. The $P-E$ loops measured without compensating the leakage current follow the same trend as previously discussed, and significantly broaden as the temperature increases, as shown in Figure 74. Consequently, the positive slope of $\frac{\partial P}{\partial T}$ results in a specious "inverse" or "negative" electrocaloric effect. On the other hand, the electrocaloric temperature is positive, which is deduced from the $P-E$ loops measured with the leakage current compensation.

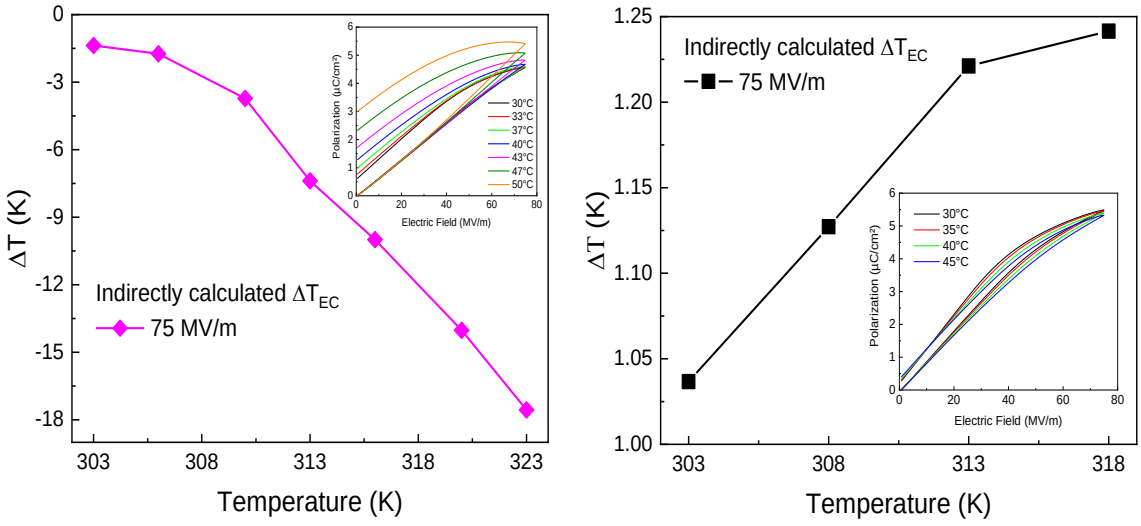

Figure 74 Indirectly calculated electrocaloric effect from the polarization hysteresis loops measured under unipolar field at 10 Hz without (left) and with (right) leakage current compensation in P(VDF–TrFE–CFE) 64.8/35.2/7.8.

4.3.3.3 Frequency of Electric Field

It has been already discussed that the frequency of the applied electric field also influences the ECE. The cooling power of the EC devices increases with the increasing operation frequency, which is the frequency of the applied electric field. [174] Guo et al. studied the effect of frequency on the direct electrocaloric measurement in a frequency range of 0.03 – 0.3 Hz in P(VDF-TrFE-CFE) 62.6/29.4/8. They found that the directly measured electrocaloric effect in P(VDF-TrFE-CFE) using an IR camera is independent of the frequency of the applied voltage. [85] Seblad et al. also used an IR camera to analyze the influence of the electric field frequency on the electrocaloric effect in P(VDF-TrFE-CFE). They chose a testing frequency range of 0.1 – 2 Hz due to the limitations imposed by the thermal time constant (10 s) for the lowest testing frequency, and by the frequency of the camera (10 Hz) for the highest testing frequency. They observed a strong decrement in the EC coefficient with increasing frequency, and explained this observation in terms of an electrocaloric creep effect in P(VDF-TrFE-CFE). [86] In both studies, the influence of the electric field frequency is studied on the direct electrocaloric measurements at very low frequencies ($\leq$ 2 Hz). The effect of a higher frequency on the ECE was analyzed by Cheng et al. (1 Hz and 100 Hz) and by Bradesko et al. (0.6 Hz and 10 Hz), where they both considered the lead zirconate titanate (PZT) system. [20, 174] The impact of the voltage frequency on the indirect electrocaloric measurement in P(VDF-TrFE-CFE) has not been reported yet, to the author's best knowledge.

The *P* – *E* loops under a unipolar and a bipolar field at 100 Hz with the leakage current compensation are shown in Figure 75. The indirectly measured ECE at 100 Hz under a unipolar as well as bipolar electric field are comparable with each other. The results obtained at 10 Hz and 100 Hz under a unipolar and a bipolar electric field are compared with each other and discussed in the upcoming section.

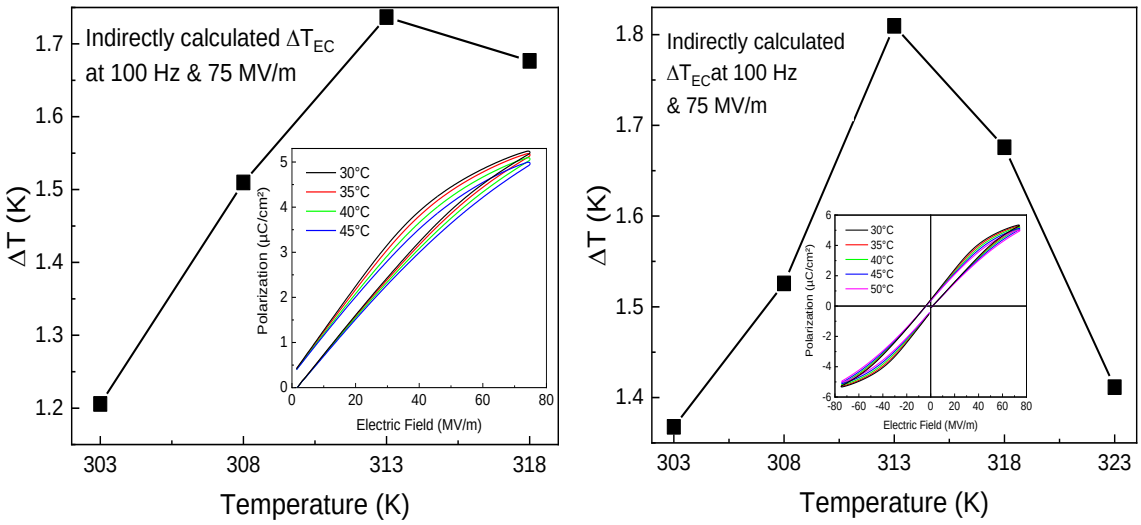

Figure 75 Indirectly calculated electrocaloric effect from the polarization hysteresis loops measured at 100 Hz with leakage current compensation under unipolar field (left) and bipolar field (right) in P(VDF–TrFE–CFE) 64.8/35.2/7.8.

4.3.4 Comparison of Directly & Indirectly Measured Electrocaloric Effect

In the previous sections, the impact of leakage current, unipolar and bipolar fields have been separately discussed. It is found that the leakage current has an adverse effect on the indirect measurement of the electrocaloric temperature change, and leads to the observation of a specious "negative" electrocaloric effect. In this section, the indirect measurement parameters are compared, and discussed relating to the direct measurement.

In Figure 76, the direct measurement performed using a quasi-adiabatic calorimeter under a unipolar field is compared to the indirect measurement done with a unipolar and a bipolar electric field of 10 Hz and 100 Hz while compensating the leakage current. For the direct measurement, the frequency of the applied unipolar field is estimated to be 10 mHz. The pulse shape of the direct measurement is saw shape, where the electric field is applied with a low slew rate (0.1 kV/s) and a high slew rate (100 kV/s) upon field removal is used, to discern the electrocaloric effect from Joule heating. The indirect measurement is performed under a triangular shaped unipolar or bipolar field, with a uniform slew rate.

The unipolar and the bipolar fields of 100 Hz show a similar trend of ΔT, as shown in Figure 76. Both electric fields exhibit a maximum electrocaloric effect at 313 K, which decreases gradually with temperature. The values of the electrocaloric temperature change due to unipolar and bipolar fields

of 100 Hz coincide at 313 K and 318 K, while the other values have a minor deviation. The remarkable feature in Figure 76 is that the unipolar as well as the bipolar electric fields at a frequency of 10 Hz show a relatively low indirectly calculated electrocaloric temperature change compared to 100 Hz. This is somehow counterintuitive, since it has been reported that the dipoles of the polymeric chains cannot orient themselves in the direction of the electric field very quickly, [13] thus as the frequency of the applied electric field increases, the response of the dipoles to the electric field decreases. It is plausible to say that the energy input through a higher number of repeating cycles of the applied electric field (100 Hz) overcomes the interchain interactions, and causes the dipoles to ultimately flip, thus the electrocaloric effect is higher at 100 Hz for unipolar as well as for bipolar fields. The bipolar field of 10 Hz shows higher electrocaloric values than the unipolar field. The plausible explanation is that the bipolar field can overcome the interchain interactions by 'shaking' the polymer chains in the opposite directions causing the dipoles to flip, while the unipolar field cannot flip many dipoles due to the strong interchain interactions.

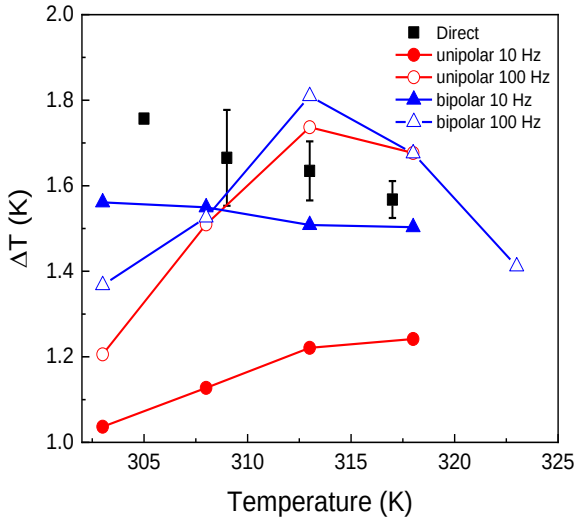

Figure 76 Comparison of direct electrocaloric measurement with indirect method at different frequencies and nature of field.

4.3.5 Conclusion

Direct and the indirect electrocaloric measurements were performed, and the indirect method parameters were analyzed in detail. The electric field induced transition results in an increase in the electrocaloric effect. It is shown that the specious negative electrocaloric effect in P(VDF–TrFE–CFE) obtained through the indirect measurements is due to the leakage current. The indirect method gives comparable values to the direct measurement method, if the leakage current of the sample is compensated during the polarization hysteresis measurements. The magnitude and the frequency of the applied electric field must be strong enough to overcome the interchain and intrachain interactions during the direct and the indirect electrocaloric measurements.

4.4 P(VDF–TrFE–CFE)/BZT Nanocomposites

From the discussion in Section 2.3.2, it is clear that the addition of the inorganic nanofiller improves the polarization characteristics of the polymers. Hence, with the aim of improving the electrocaloric and the energy storage properties of P(VDF-TrFE-CFE), nanoparticles of zirconium doped barium titanate ($BaZr_{0.2}Ti_{0.8}O_3$) (BZT) are introduced into the polymer. BZT is an attractive material for technological applications, such as tunable microwave devices, transducers, and capacitors, owing to its promising dielectric, ferroelectric, and electromechanical properties. [175–178] In zirconium doped barium titanate, the Ti^{4+} ion is substituted by the Zr^{4+} ion. This substitution results in shifting the phase transition temperature. As a result, the two ferroelectric–ferroelectric phase transitions of barium titanate, namely, orthorhombic–rhombohedral and tetragonal–orthorhombic, are shifted towards a higher temperature. While, the paraelectric–ferroelectric (cubic–tetragonal) phase transition temperature is shifted towards a lower temperature regime. The $BaZr_xTi_{1-x}O_3$ system exhibits typical relaxor behavior when $x \geq 0.20$. [179–183] Therefore, in this work, the relative amount of zirconium in BZT is set to 20 mol.%, aiming to achieve relaxor behavior in zirconium doped barium titanate nanoparticles, and to match its transition temperature with P(VDF–TrFE–CFE), which is in the vicinity of room temperature. [179, 184]

This section starts with the characterization of the synthesized $BaZr_{0.2}Ti_{0.8}O_3$ nanoparticles via the hydrothermal route. This is followed by the characterization of the BZT/terpolymer nanocomposite films through the XRD and SEM techniques. The nanocomposite films of three different P(VDF–TrFE–CFE) compositions, namely, 64.8/35.2/7.8, 68/32/8.5, and 70/30/8.1 are prepared. The volume fraction of BZT nanoparticles is varied (1.25 vol.%, 2.5 vol.%, and 5 vol.%). The maximum amount of BZT nanoparticles in the terpolymer matrix is 5 vol.%, as it was difficult to obtain free-standing films with a higher nanoparticle volume. The dielectric, ferroelectric, and energy storage properties of all BZT/P(VDF–TrFE–CFE) nanocomposite systems are investigated. All polarization hysteresis loops are measured without compensating the leakage current. The direct electrocaloric measurement is also performed.[2]

[2] *A major portion of section 4.4 has been published in 2021 IEEE International Symposium on Applications of Ferroelectrics (ISAF), 2021, pp. 1-4, under the title of "Directly Measured Electrocaloric Effect in Relaxor Polymer Nanocomposites" and in Materials, Volume 15, Issue 9, 2022, bearing the title "High Energy Storage Density in Nanocomposites of P(VDF-TrFE-CFE) Terpolymer and $BaZr_{0.2}Ti_{0.8}O_3$ Nanoparticles".*

4.4.1 Characterization of $BaZr_{0.2}Ti_{0.8}O_3$ Nanoparticles

The BZT nanoparticles are synthesized by the hydrothermal method, as explained in detail in Section 3.1.2. The synthesized nanoparticles are characterized using the XRD and SEM to analyze the structure, phase content, morphology, and size distribution of the nanoparticles.

The XRD pattern of the BZT nanoparticles after washing with ethanol and water is shown in Figure 77. The XRD spectrum shows distinct peaks which are characteristic of the cubic crystal structure of perovskite. The XRD spectrum in Figure 77 shows a few other peaks, which are not representative of the BZT cubic crystal structure. Along with the primary perovskite phase, a secondary phase is also present, which is identified as barium carbonate ($BaCO_3$) of about 8%.

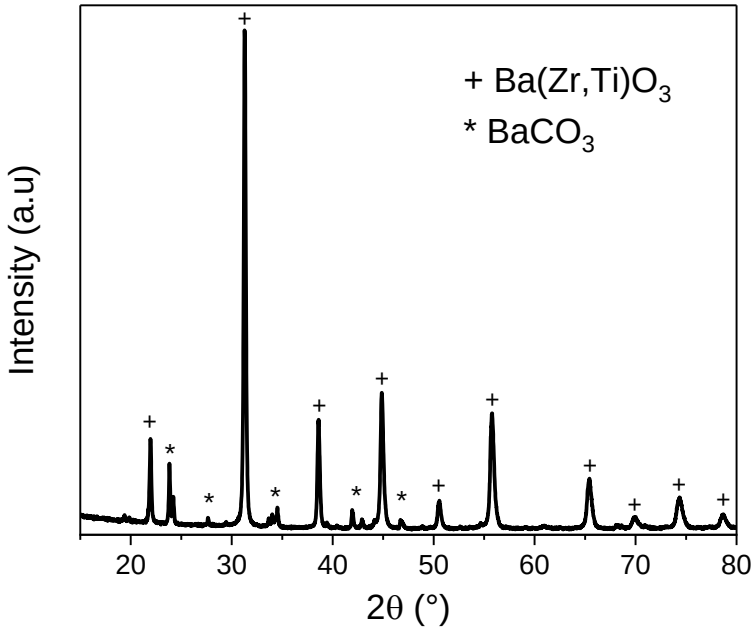

Figure 77 X-ray diffractogram of as-synthesized zirconium doped barium titanate where barium carbonate is present as a secondary phase.

In Figure 78, the SEM image validates the presence of barium carbonate as the secondary phase. The barium carbonate is present in the witherite crystalline form, which is characterized by a rod-like structure (Figure 78). In order to get rid of the barium carbonate, the BZT nanoparticles are washed with 5 vol.% acetic acid (CH_3COOH). The barium carbonate reacts with the acetic acid according to the Equation 47. Upon reacting with the acetic acid, the barium carbonate forms barium acetate

($Ba(CH_3COO)_2$), carbon dioxide and water. The barium acetate is then separated as supernatant via centrifugation at 9000 rpm.

$$BaCO_3 + CH_3COOH \rightarrow Ba(CH_3COO)_2 + CO_2 + H_2O \quad (47)$$

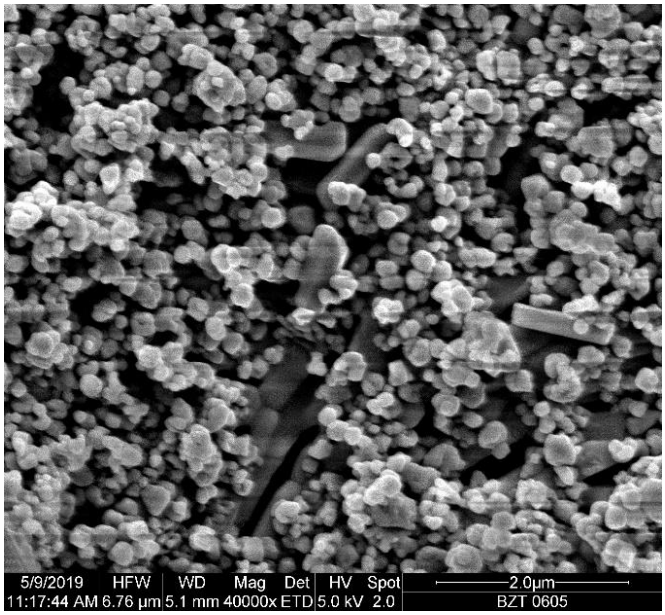

Figure 78 SEM image of as-synthesized zirconium doped barium titanate nanoparticles also containing barium carbonate rod-like structures (secondary phase).

Figure 79 shows the XRD spectrum of the BZT nanoparticles washed with the acetic acid. The XRD pattern do not show the barium carbonate peaks anymore. This indicates that the barium carbonate is effectively washed away with the acetic acid.

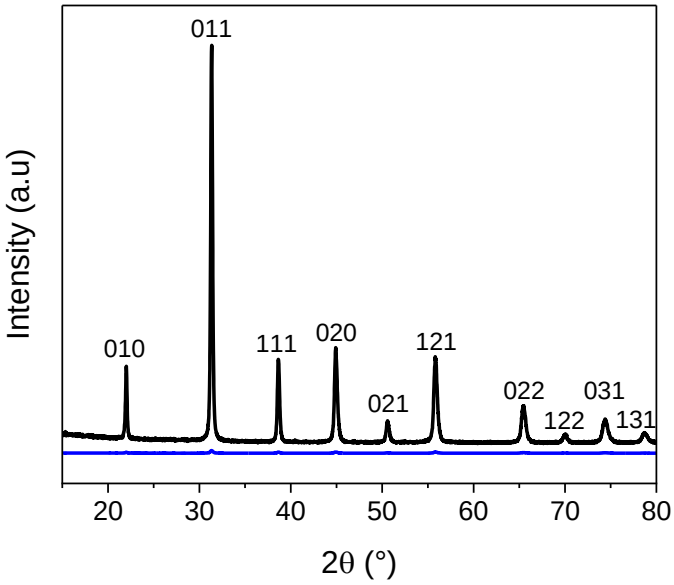

Figure 79 X-ray diffractogram of nanoparticles washed with 5 vol.% acetic acid, here the barium carbonate is washed away.

In Figure 80, the SEM image of the BZT particles washed with acetic acid is shown. The rod structure is not observed in SEM after the washing step. The synthesized BZT nanoparticles are round shaped. From Figure 80, it can be roughly concluded that the synthesized nanoparticles have a homogenous size distribution.

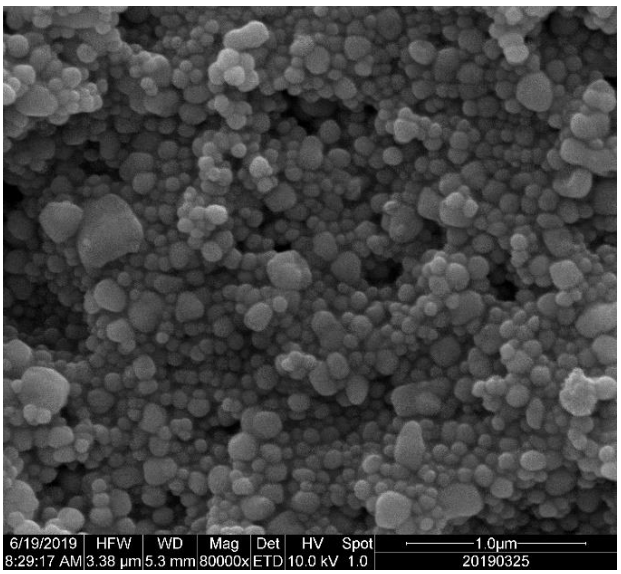

Figure 80 SEM image of washed nanoparticles, rod-like structure is washed away.

The SEM images are further analyzed to calculate the particle size distribution of the synthesized nanoparticles. The cumulative and frequency distributions of the diameter of the BZT nanoparticles are shown in Figure 81. The synthesized BZT nanoparticles show a narrow particle size distribution, which lies between 100 – 300 nm. Particles bigger than 300 nm are rare. The diameter of almost 90% of the analyzed particles is smaller than 250 nm, while the mean particle size (d_{50}) is estimated to be 150 nm.

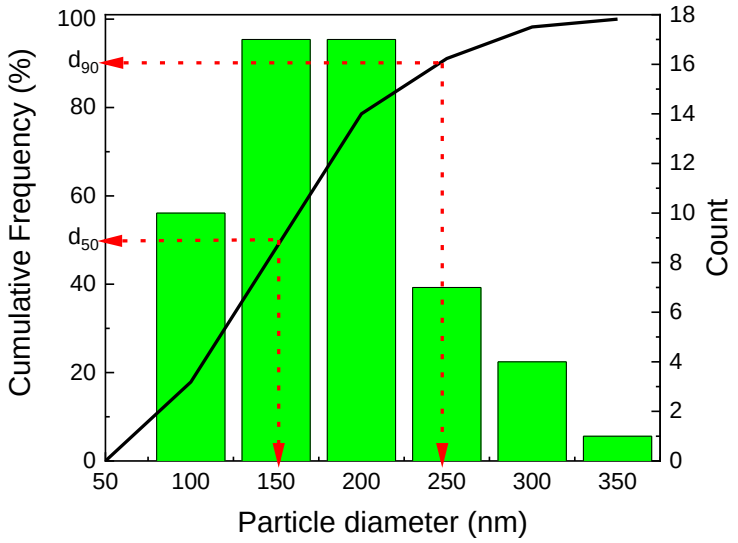

Figure 81 Cumulative and frequency size distribution of synthesized nanoparticles generated by analyzing SEM images.

4.4.2 Characterization of Nanocomposite Films

The XRD pattern of a nanocomposite film with 5 vol.% BZT nanoparticles is shown in Figure 82. A distinct peak at 17.8° is detected, that is characteristic of the α phase which is paraelectric and non-polar, while all other peaks are representative of BZT nanoparticles. The addition of nanoparticles in the terpolymer matrix has no influence on the obtained crystalline phase of the terpolymer.

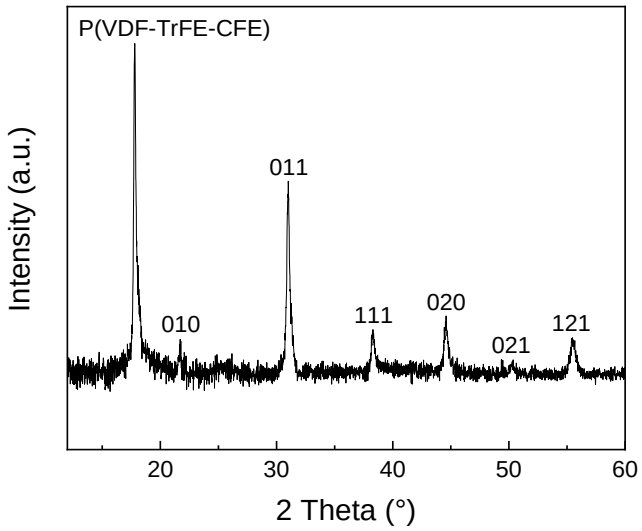

Figure 82 X-ray diffractogram of polymer nanocomposite film.

In Figure 83, SEM images of the nanocomposite films with different nanoparticle volume are shown. The image of the sample containing 1.25 vol.% BZT nanoparticles is taken at a higher magnification (100000 x) to see the distribution of the nanoparticles in the polymer matrix, while the images of the samples with 2.5 vol.% and 5 vol.% BZT nanoparticles are taken at a lower magnification (15000 x). It can be observed in Figure 83, that the BZT nanoparticles, which appear as white spots, are homogenously distributed within the polymer matrix at all loading volumes. The nanoparticles do not form agglomerates during the drying and annealing of the nanocomposite films even at higher loading (5 vol.%).

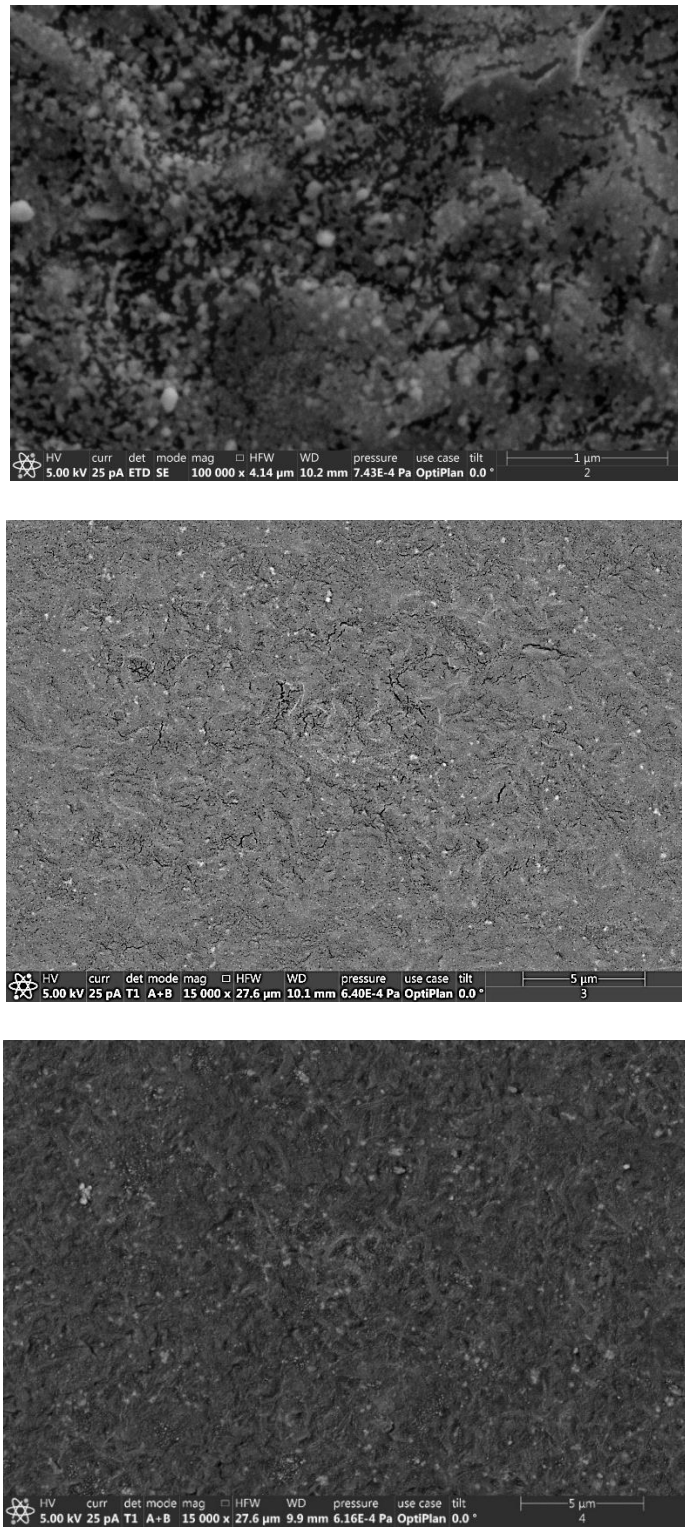

Figure 83 SEM image of polymer nanocomposite films containing 1.25 vol.% BZT (top), 2.5 vol.% BZT (middle), & 5 vol.% BZT (bottom) where nanoparticles appear as white spots with a homogenous distribution in the polymer matrix.

The SEM image in Figure 84 shows a cross-section of the nanocomposite film containing 5 vol.% nanoparticles. The nanocomposite film is immersed in liquid nitrogen, and broken for the cross-sectional view. The nanocomposite film has a uniform distribution of BZT nanoparticles along the thickness at the maximum i.e. 5 vol.% loading. The nanoparticles do not settle down during the processing of the nanocomposite films.

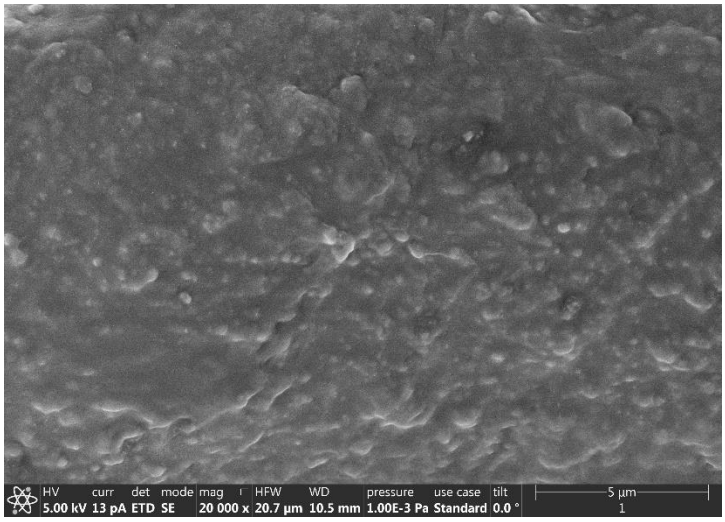

Figure 84 SEM image of cross-sectional view of polymer nanocomposite film with 5 vol.% BZT nanoparticles.

4.4.3 P(VDF-TrFE-CFE) 64.8/35.2/7.8 Nanocomposite

4.4.3.1 Dielectric Properties

The dielectric permittivity curves of nanocomposites are measured using the same experimental parameters and temperature (270 K – 370 K) and frequency ranges (1 kHz to 1 MHz) as for the neat terpolymers. Figure 85 shows the permittivity as well as the loss tangent curves measured upon cooling of nanocomposite films of P(VDF-TrFE-CFE) 64.8/35.2/7.8 having varying volume fractions of nanofiller i.e. BZT nanoparticles, 1.25 vol.%, 2.5 vol.%, and 5 vol.%. The broad peak around room temperature signifies the relaxor behavior of the nanocomposite films. With increasing frequency, the permittivity peaks move towards higher temperatures, the values of the dielectric permittivity decreases, while the dielectric loss tangent increases. There is a gradual increase in dielectric permittivity of nanocomposite films with the relatively increasing amount of nanoparticles, 1.25 vol.% to 5 vol.%.

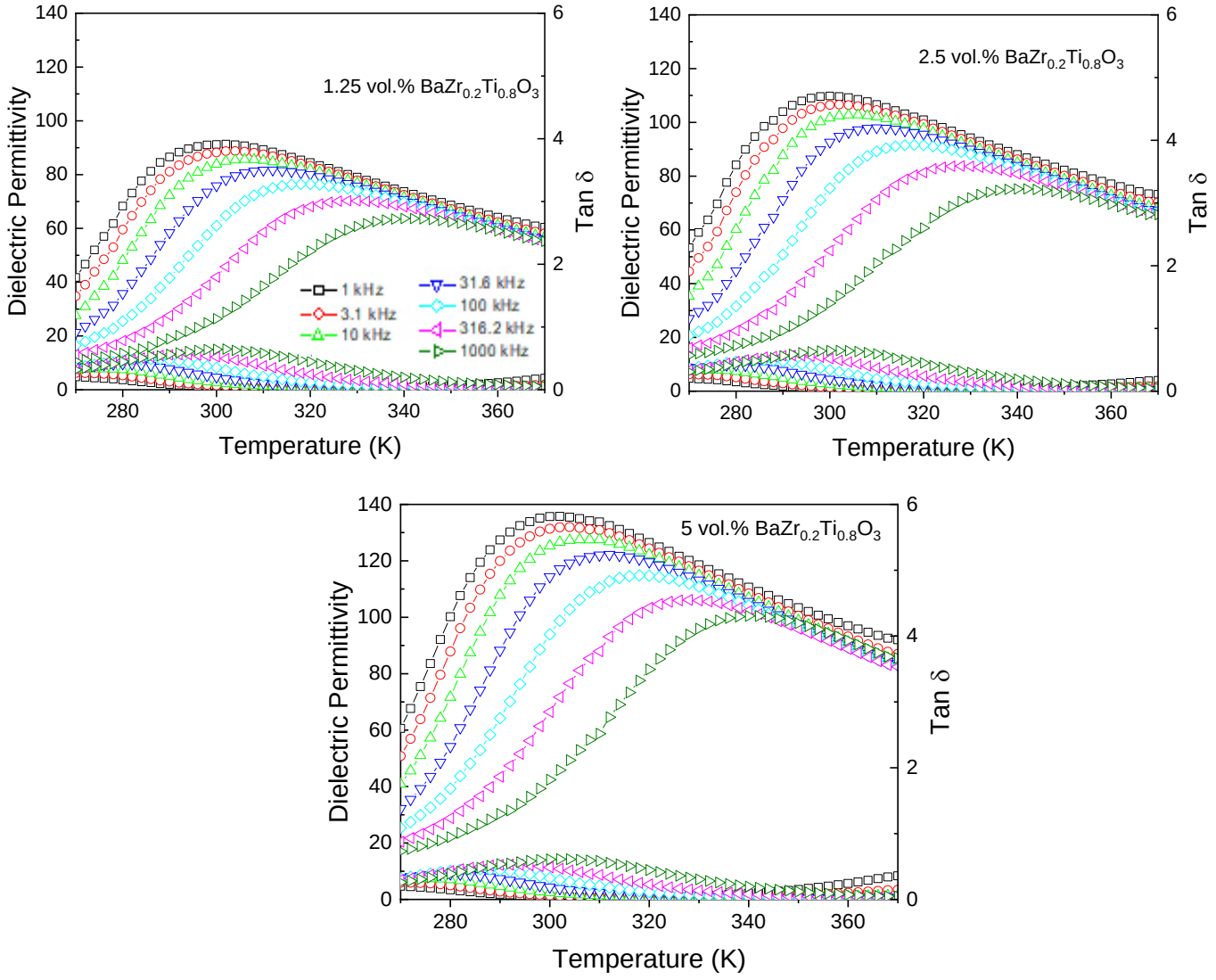

Figure 85 Dielectric permittivity curves of P(VDF-TrFE-CFE) 64.8/35.2/7.8 with varying BZT nanoparticles content, 1.25 vol.%, 2.5 vol.%, and 5 vol.% measured upon cooling.

Figure 86 compares the dielectric permittivity and the tangent loss curves of neat terpolymer and its nanocomposites at 1 kHz. The neat terpolymer film shows a maximum dielectric permittivity ~ 80, which increases significantly when the BZT nanoparticles are introduced in the terpolymer matrix. The sample with 5 vol.% BZT nanoparticles shows a maximum dielectric permittivity ~ 140. The tangent loss values of the nanocomposite samples with 1.25 vol.% and 2.5 vol.% BZT nanoparticles

are almost the same as the neat terpolymer. However, the nanocomposite sample with 5 vol.% BZT nanoparticles shows a higher tangent losses than other samples at temperatures above 320 K due to leakage current. The higher tangent losses in the lower temperature region can be due to the glass transition.

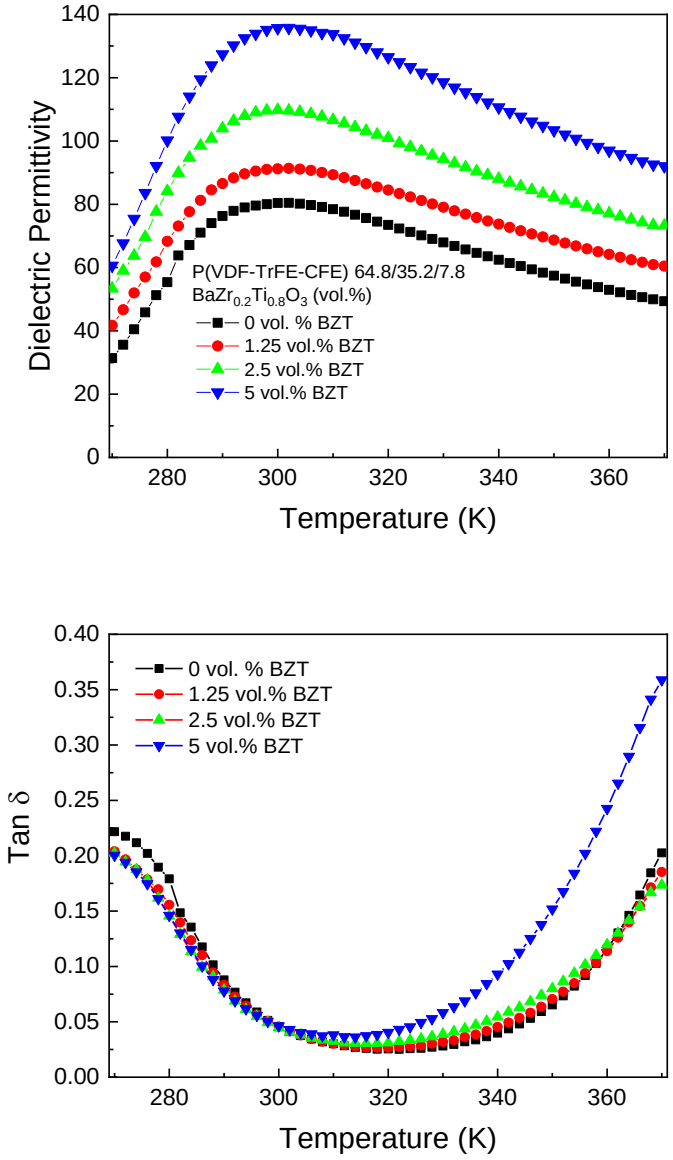

Figure 86 Comparison of the dielectric permittivity and losses curves of P(VDF-TrFE-CFE) 64.8/35.2/7.8 neat polymer and its nanocomposites at 1 kHz as a function of temperature.

4.4.3.2 Polarization Hysteresis Measurement

P – E loops of the neat P(VDF-TrFE-CFE) 64.8/35.2/7.8 sample and its nanocomposites with different BZT nanoparticle contents (1.25 vol.%, 2.5 vol.% and 5 vol. %), shown in Figure 87, are measured under a triangular field of 10 Hz at room temperature. The maximum polarization (P_{max}) gradually increases with the increasing volume fraction of nanoparticles. The maximum polarization (P_{max}) increases from $3.8\,\mu C/cm^2$ to $6.3\,\mu C/cm^2$ when 5 vol.% BZT nanoparticles are added to the terpolymer matrix. The remnant polarization (P_{rem}) of the neat terpolymer $0.3\,\mu C/cm^2$ increases to $0.7\,\mu C/cm^2$ for the polymer nanocomposite sample containing 5 vol.% BZT nanoparticles. The values of P_{max} as well as P_{rem} are in agreement with the previous report. [120] The P_{max}, and P_{rem} values of P(VDF-TrFE-CFE) 64.8/35.2/7.8 and its 1.25 vol.%, 2.5 vol.% and 5 vol. % BZT nanocomposites are enlisted in Table 16.

Table 16 Maximum and remnant polarization values of P(VDF-TrFE-CFE) 64.8/35.2/7.8 neat polymer and its nanocomposites.

BZT Volume Fraction	0 vol.%	1.25 vol.%	2.5 vol.%	5 vol.%
$P_{max}\,(\mu C/cm^2)$	4.1	5.0	6.0	6.7
$P_{rem}\,(\mu C/cm^2)$	0.31	0.73	0.51	0.67

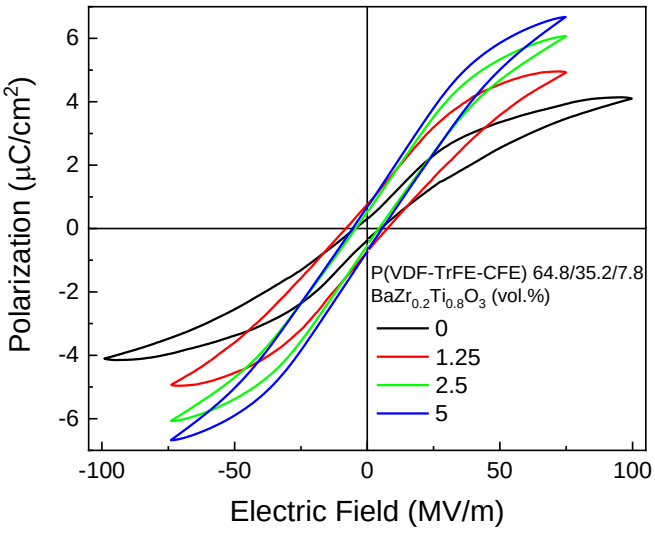

Figure 87 P-E loops of the nanocomposite P(VDF-TrFE-CFE) 64.8/35.2/7.8 nanocomposite films with different particle volume fractions measured at 10 Hz at room temperature

4.4.3.3 Direct Electrocaloric Measurement

The direct electrocaloric effect is measured in the nanocomposite of P(VDF-TrFE-CFE) 64.8/35.2/7.8 having 5 vol. % of BZT nanoparticles. In this nanocomposite film, the electrocaloric temperature change values at room temperature are 0.6 K and 1.8 K at 25 MV/m and 50MV/m, respectively (Figure 88). Comparing the electrocaloric coefficients of the neat polymer and this nanocomposite at 50 MV/m, it is clear that the electrocaloric effect is significantly enhanced upon the addition of BZT nanoparticles. The ΔT_{EC} in the neat polymer is merely 1 K; while in the nanocomposite film with 5 vol. % nanoparticles, ΔT_{EC} is 1.8 K which means that there is an 80% increase in the electrocaloric temperature change already at a low volume fraction (5 vol. %) of nanoparticles. The neat polymer has an electrocaloric coefficient of 1.8 K at 75 MV/m; while in the nanocomposite, the same value of the electrocaloric temperature change is achieved at a much lower electric field i.e. 50 MV/m. This infers that for 1 µm thin film only 50 V is required to achieve a ΔT_{EC} of 1.8 K. Like the dielectric permittivity and the polarization values, the enhancement in the electrocaloric coefficients in P(VDF-TrFE-CFE) nanocomposites can be attributed to the interfacial polarization. The interfacial polarization occurs due to the presence of unbounded charges (remaining chemical species from the processing, impurities, etc.), contributing to the total polarization, under an applied electric field.

However, the details of the mechanism(s), that enhance the electrocaloric effect in such nanocomposite systems, are not clear yet. [117, 118, 120, 185] The polymer nanocomposites can withstand higher electric fields compared to the bulk ceramics due to the high dielectric breakdown strength of the polymers. The electric field distribution in the polymer nanocomposites applied is not uniform, since ceramic fillers have a higher dielectric constant than the polymer matrix. [53]

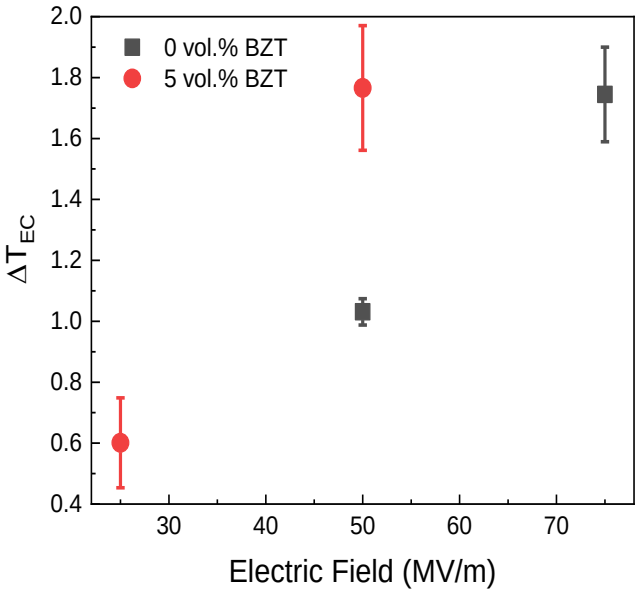

Figure 88 Directly measured electrocaloric effect in P(VDF–TrFE–CFE) 64.8/35.2/7.8 neat polymer and its nanocomposite with 5 vol.% BZT nanoparticles at room temperature.

The electrocaloric coefficients in P(VDF-TrFE-CFE) 64.8/35.2/7.8 and its nanocomposite with BZT nanoparticles are in good agreement with the previous report, where Aziguli et al. measured the electrocaloric effect in P(VDF-TrFE-CFE) 66.8/33.2/8.9 and its nanocomposites with 5 vol. % BZT nanoparticles, compared in Table 17. They used a customized calorimeter under isothermal conditions to measure the electrocaloric generated heat (ΔQ_{EC}), and the electrocaloric temperature change was estimated through the relation $\Delta T_{EC} = \Delta Q_{EC}/c_p$. [122] In this work, ΔT_{EC} in the polymer nanocomposites is directly measured under quasi-adiabatic conditions. Both results are comparable with each other.

Table 17 Electrocaloric coefficients in P(VDF-TrFE-CFE)/BZT nanocomposites at room temperature.

$BaZr_{0.20}Ti_{0.80}O_3$ – $P(VDF_x\text{-}TrFE_{1\text{-}x}\text{-}CFE_y)$	ΔT_{EC}	Electric Field (MV/m)	Reference
5 vol. % $BaZr_{0.20}Ti_{0.80}O_3$ – 64.8/35.2/7.8	0.6	25	This work
	1.8	50	This work
5 vol. % $BaZr_{0.20}Ti_{0.80}O_3$ – 66.8/33.2/8.9	0.7	30	[122]
	2.2	50	[122]

4.4.4 P(VDF-TrFE-CFE) 68/32/8.5 Nanocomposite

4.4.4.1 Dielectric Properties

In Figure 89, the dielectric permittivity and the dielectric loss tangent of the nanocomposites with different filler contents (1.25, 2.5 and 5 vol. %), measured within a frequency range of 1 kHz to 1 MHz upon cooling, are shown as a function of temperature from 270 K to 370 K. The broad dielectric peaks and their frequency dispersion validate the relaxor behavior in the P(VDF-TrFE-CFE) 68/32/8.5 nanocomposite films. Furthermore, Figure 89 compares the dielectric permittivity and the dielectric tangent loss curves of the neat polymer and its nanocomposites at 1 kHz. At 1 kHz, the neat polymer exhibits a maximum dielectric permittivity of about 55, which is enhanced upon the addition of BZT nanofiller. The dielectric permittivity of the nanocomposite films progressively increases, as the relative amount of BZT nanoparticles is increased. [123, 153] The dielectric permittivity of the nanocomposite film having 5 vol. % BZT nanofiller is almost double to that of the neat polymer, and shows a maximum dielectric permittivity ~ 100. The permittivity values of the nanocomposite films at 1 kHz show a slight increase at higher temperatures. The slight increment of the dielectric permittivity of the P(VDF-TrFE-CFE) nanocomposites at low frequencies (≤ 1 kHz) and at a higher measuring temperatures has been previously observed as well. [119] This increment can be attributed to the presence of charges (residual chemical species from the processing, impurities) on the surface of BZT nanoparticles and at the polymer/nanoparticle interface, which becomes significant with rising temperature.

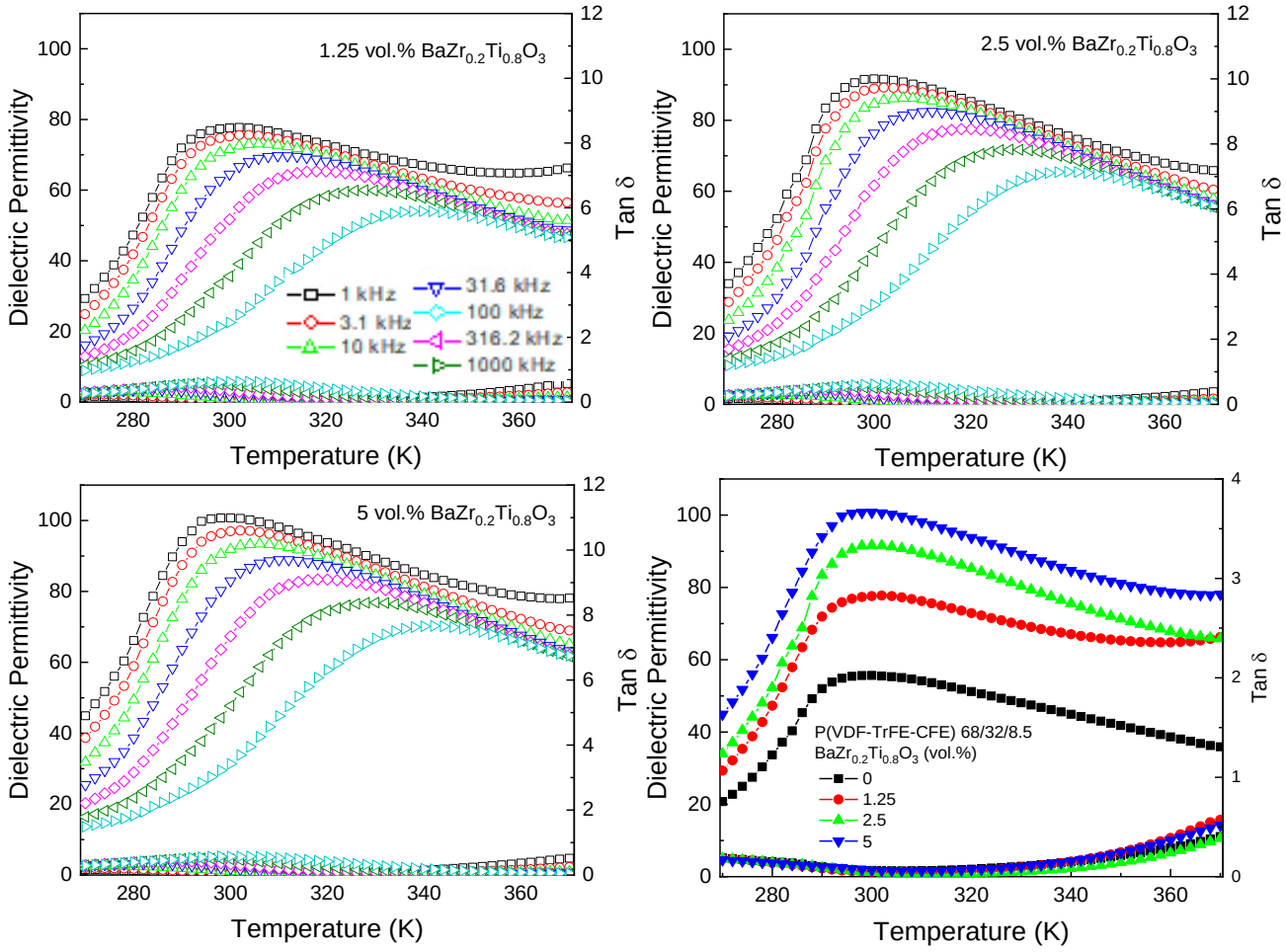

Figure 89 The dielectric permittivity curves of P(VDF-TrFE-CFE) 68/32/8.5 with varying BZT nanoparticles content, 1.25 vol.%, 2.5 vol.% and 5 vol.%, and comparison of dielectric permittivity and losses curves of P(VDF-TrFE-CFE) 68/32/8.5 neat polymer and its nanocomposites at 1 kHz as a function of temperature.

4.4.4.2 Polarization Hysteresis Measurement

The polarization hysteresis loops of the neat terpolymer sample and its nanocomposites with the different filler contents (1.25, 2.5 and 5 vol. %) are measured under a triangular field of 10 Hz, shown in Figure 90. The $P - E$ loop of the neat terpolymer shows a paraelectric like loop at 75 MV/m, while the nanocomposite samples have typical relaxor loops. The maximum applied electric field on the nanocomposite films is 75 MV/m due to their low dielectric breakdown strength. The saturation polarization (P_s) values of the nanocomposite films remain higher ($5 - 6$ μC/cm^2) at a moderate electric field i.e. 75 MV/m, while for the neat terpolymer, P_s = 4 μC/cm^2 is achieved at a much higher electric field, namely 150 MV/m. The presence of BZT nanoparticles in the terpolymer causes the

maximum polarization to be achieved at a much lower magnitude of electric fields. This observation also verifies the dielectric data, where the dielectric permittivity values of the nanocomposites (Figure 89) are significantly higher than that of the neat terpolymer.

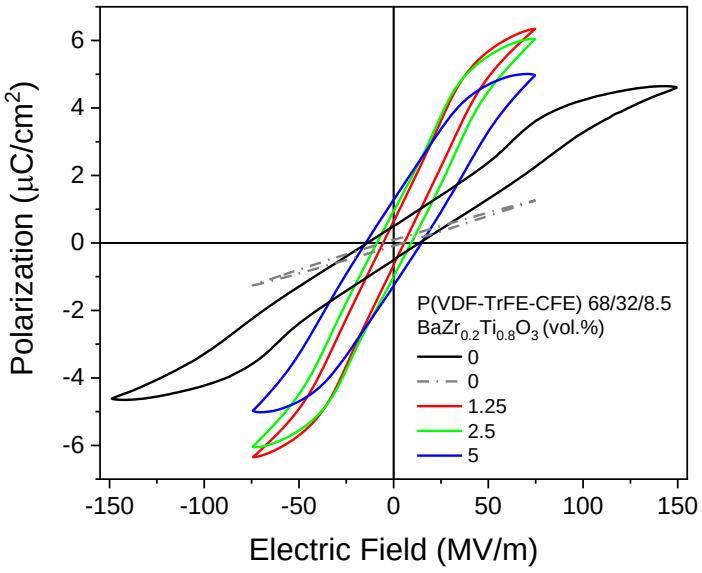

Figure 90 Comparing the *P–E* loops of 68/32/8.5 terpolymer at 75 MV/m & 150 MV/m with its nanocomposites (75 MV/m) having different filler contents (1.25, 2.5 and 5 vol. %).

4.4.5 P(VDF-TrFE-CFE) 70/30/8.1 Nanocomposite

4.4.5.1 Dielectric Properties

Similar to the P(VDF-TrFE-CFE) 64.8/35.2/7.8 and 68/32/8.5 nanocomposite samples, the nanocomposite of P(VDF-TrFE-CFE) 70/30/8.1 containing 5 vol.% BZT nanoparticles also shows a broad permittivity peak moving towards higher temperature, and the tangent losses are increasing with frequency, as shown in Figure 91. Such a trend confirms the relaxor properties of the 5 vol.% BZT/ P(VDF-TrFE-CFE) 70/30/8.1 nanocomposite film. The permittivity values of 5 vol.% BZT/ P(VDF-TrFE-CFE) 70/30/8.1 are significantly higher than the neat terpolymer, which is in agreement with the nanocomposites of the other two compositions of P(VDF-TrFE-CFE) i.e. 64.8/35.2/7.8 and 68/32/8.5, and to previous reports. [122, 153]

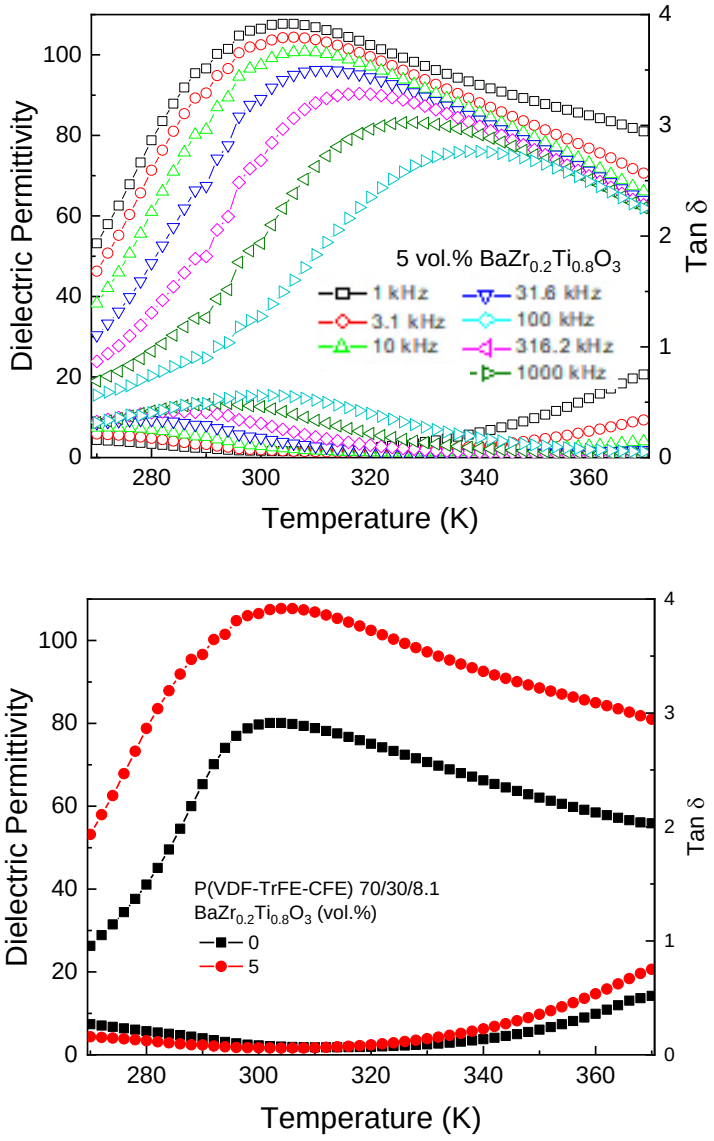

Figure 91 The dielectric permittivity curves of P(VDF-TrFE-CFE) 70/30/8.1 with 5 vol.% BZT nanoparticles and comparison of dielectric permittivity and losses curves of P(VDF-TrFE-CFE) 70/30/8.1 neat polymer with its nanocomposite.

4.4.5.2 Polarization Hysteresis Measurement

The *P* – *E* loop of the nanocomposite film of P(VDF–TrFE–CFE) 70/30/8.1 having 5 vol.% BZT nanoparticles shows a different trend compared to the other two terpolymer nanocomposite systems (Figure 92). The maximum polarization of 5 vol.% BZT/ P(VDF-TrFE-CFE) 70/30/8.1 does not increase at all compared to the neat polymer. However, the remnant polarization of the nanocomposite film is significantly higher than the neat polymer, which can be due to conductivity losses.

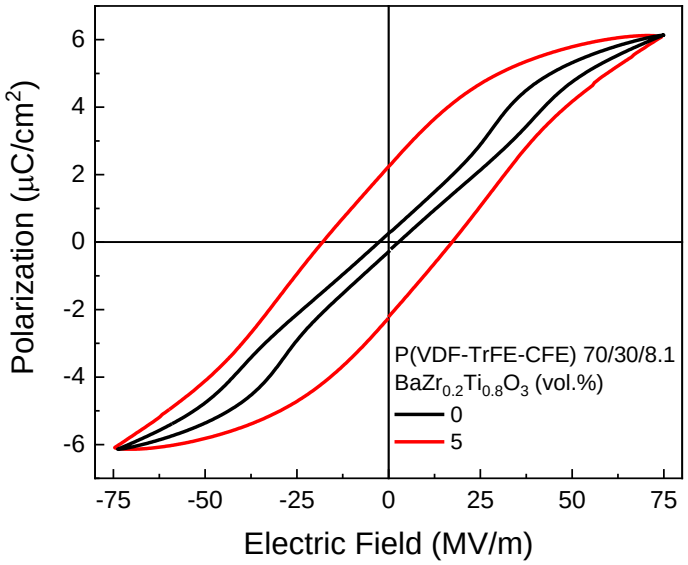

Figure 92 Comparing the P–E loops of 70/30/8.1 terpolymer at 75 MV/m with its nanocomposite having 5 vol. % BZT nanoparticles.

4.4.6 Energy Storage Properties of Polymer Nanocomposites

In the previous discussion, it has been shown that the dielectric permittivity of the terpolymers enhances upon the addition of nanoparticles. The increase in dielectric permittivity signifies that the maximum polarization in the nanocomposites will be achieved faster than in the neat polymer. [59, 186, 187] The unipolar loops are measured under a triangular field of 10 Hz at room temperature under varying electric field without leakage current compensation. The discharge energy density (Equation 24) and the charge-discharge efficiency (Equation 26) are calculated using unipolar loops according to the polarization based method, described in Section 2.3.3.1.

4.4.6.1 64.8/35.2/7.8 System

Figure 93 shows the unipolar loops of P(VDF-TrFE-CFE) 64.8/35.2/7.8 neat polymer and its nanocomposites containing 1.25 vol.%, 2.5 vol.%, and 5 vol.% BZT nanoparticles as a function of maximum applied electric field measured at room temperature. The maximum polarization is increasing with the increasing amount of nanofiller, but the losses due to hysteresis and leakage current are also increasing with the nanofiller content, such as in the 2.5 vol.% BZT/ P(VDF-TrFE-CFE) 64.8/35.2/7.8 sample where the remnant polarization and the losses are significantly higher than in other nanocomposite samples even at low electric field.

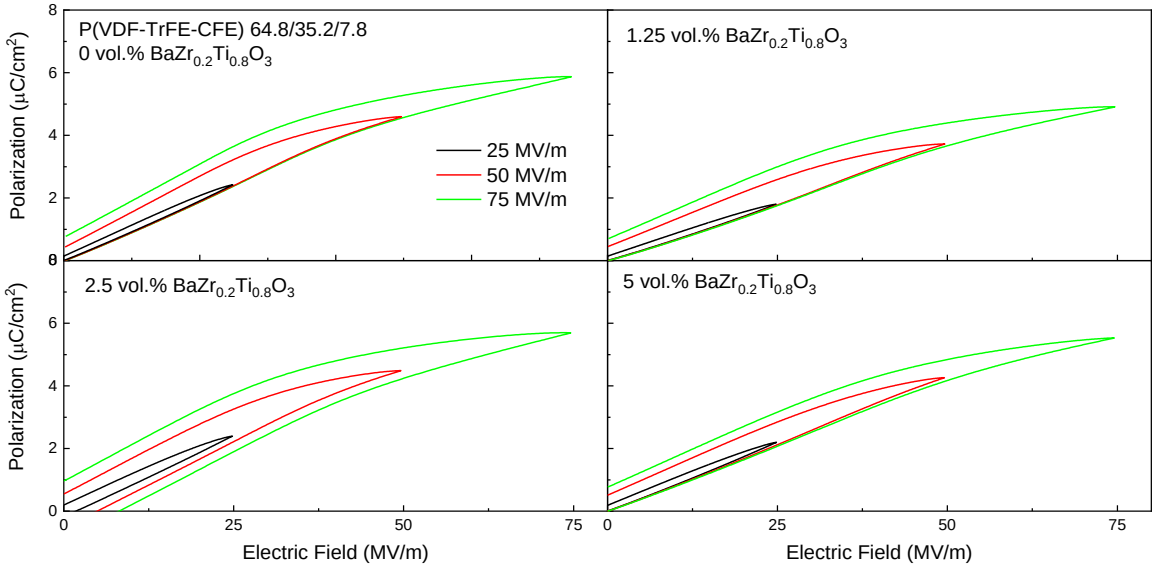

Figure 93 The unipolar curves of neat P(VDF-TrFE-CFE) 64.8/35.2/7.8 and its nanocomposites (1.25 vol.%, 2.5 vol.%, and 5 vol.% BZT nanoparticles) measured under triangular field of 10 Hz at room temperature.

In Figure 94, the discharged energy density and the charge-discharge energy efficiency of P(VDF-TrFE-CFE) 64.8/35.2/7.8 and its nanocomposites are plotted against the maximum applied electric field at room temperature. An increase in the discharged energy density is clearly observed in Figure 94, when the BZT nanoparticles are introduced in the P(VDF-TrFE-CFE) polymer matrix. The discharged energy densities of 2.5 vol.% BZT/P(VDF-TrFE-CFE) and 5 vol.% BZT/P(VDF-TrFE-CFE) nanocomposites at 75 MV/m are ~ 2.5 J/cm^3 , while the neat terpolymer has merely 1.2 J/cm^3.

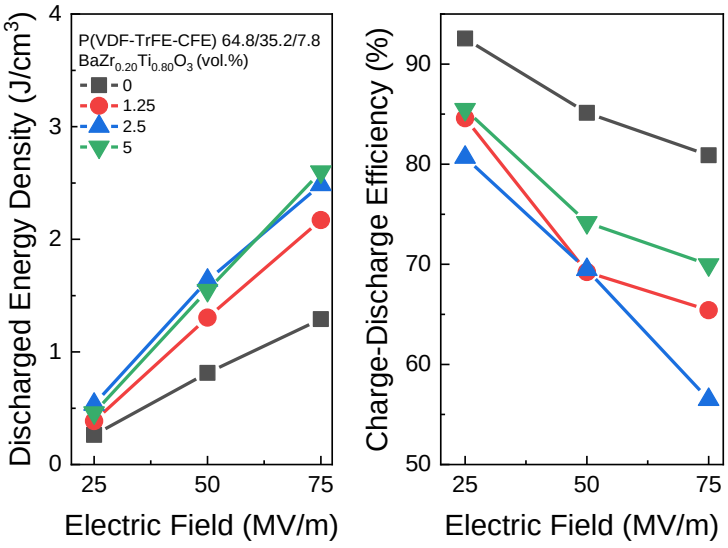

Figure 94 Discharge energy density and charge-discharge efficiency of P(VDF–TrFE–CFE) 64.8/35.2/7.8 and nanocomposites estimated from the unipolar curves shown in Figure 93.

4.4.6.2 68/32/8.5 System

The unipolar loops of the P(VDF-TrFE-CFE) 68/32/8.5 neat polymer are compared with its nanocomposites with 1.25 vol.%, 2.5 vol.% and 5 vol.% BZT nanoparticles in Figure 95. All samples show a double hysteresis loop except for the 5 vol.% BZT/ P(VDF-TrFE-CFE) 68/32/8.5 sample.

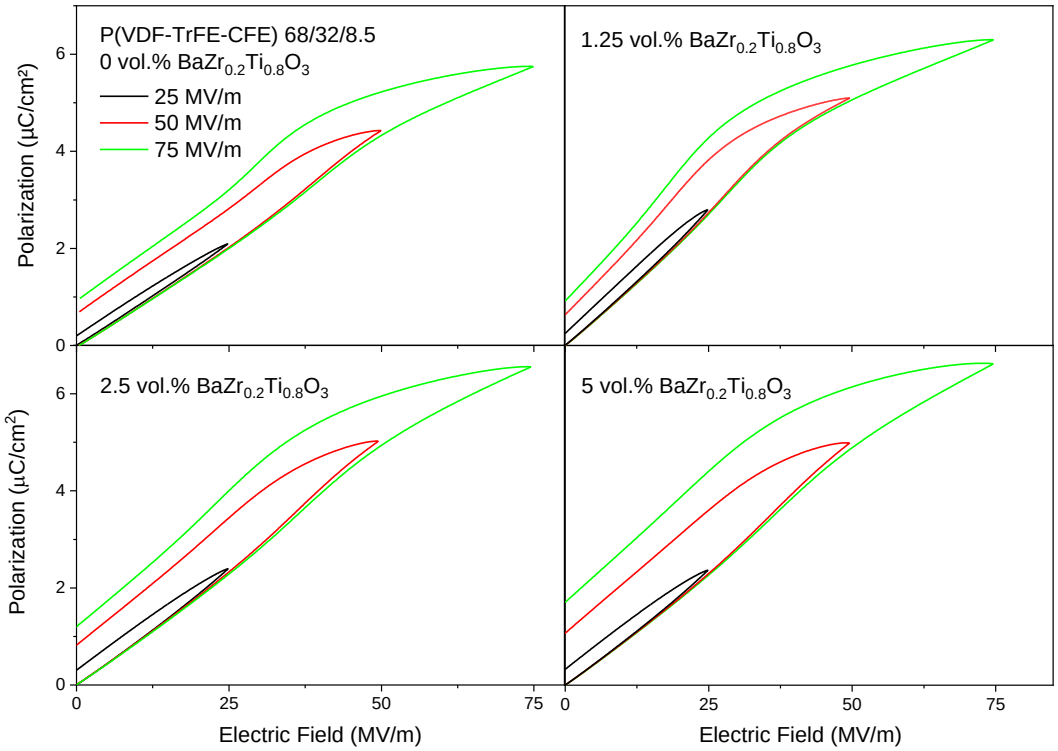

Figure 95 The unipolar curves of neat P(VDF-TrFE-CFE) 68/32/8.5 and its nanocomposites (1.25 vol.%, 2.5 vol.%, and 5 vol.% BZT nanoparticles) measured under triangular field of 10 Hz at room temperature.

The same trend is observed for the P(VDF-TrFE-CFE) 68/32/8.5 nanocomposites, where the discharge energy density of the neat polymer increases as the BZT nanoparticles are introduced in to the polymer matrix (Figure 96), while the charge-discharge efficiency decreases as the relative amount of BZT nanoparticles increases. Comparing the energy storage characteristics of nanocomposites of P(VDF-TrFE-CFE) 64.8/35.2/7.8 and 68/32/8.5 at 75 MV/m, it is evident that the discharged energy density of both compositions is almost similar. However, the charge-discharge efficiency of the 68/32/8.5 nanocomposites is lower compared to the 64.8/35.2/7.8 nanocomposites due to the double hysteresis loop (DHL), which additionally increases the area enclosed between the charge and discharge loops, hence decreasing the efficiency.

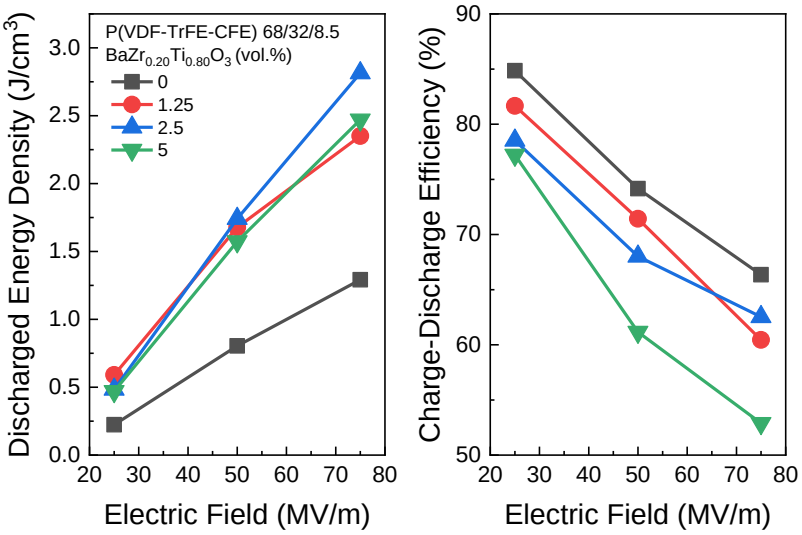

Figure 96 Discharge energy density and charge-discharge efficiency of P(VDF–TrFE–CFE) 68/32/8.5 and nanocomposites estimated from the unipolar curves shown in Figure 95.

4.4.6.3 70/30/8.1 System

In Figure 97, the unipolar loops of the P(VDF-TrFE-CFE) 70/30/8.1 neat sample and its nanocomposite with 5 vol.% BZT nanoparticles are presented. The 5 vol.% BZT/ P(VDF-TrFE-CFE) 70/30/8.1 shows enormous losses (area enclosed between charge and discharge loop) as shown in the unipolar loops.

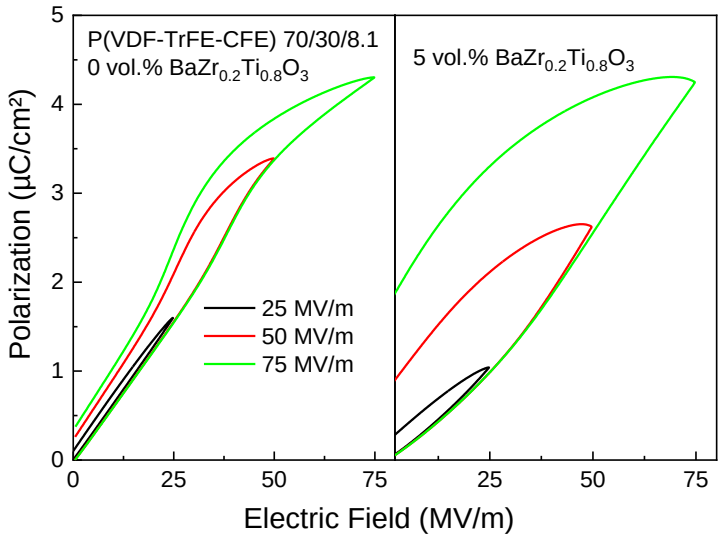

Figure 97 The unipolar curves of neat P(VDF-TrFE-CFE) 70/30/8.1 and its nanocomposites with 5 vol.% BZT nanoparticles measured under triangular field of 10 Hz at room temperature.

In Figure 98, the discharged energy of 5 vol.% BZT/P(VDF-TrFE-CFE) 70/30/8.1 only slightly improves at 75 MV/m, while at lower electric field (<75 MV/m), it remains the same as that of the neat terpolymer. The charge-discharge efficiency of the P(VDF-TrFE-CFE) 70/30/8.1 nanocomposite shows a similar trend as the nanocomposites of the other two compositions and drops drastically with increasing electric field due to huge losses exposed in the unipolar loops.

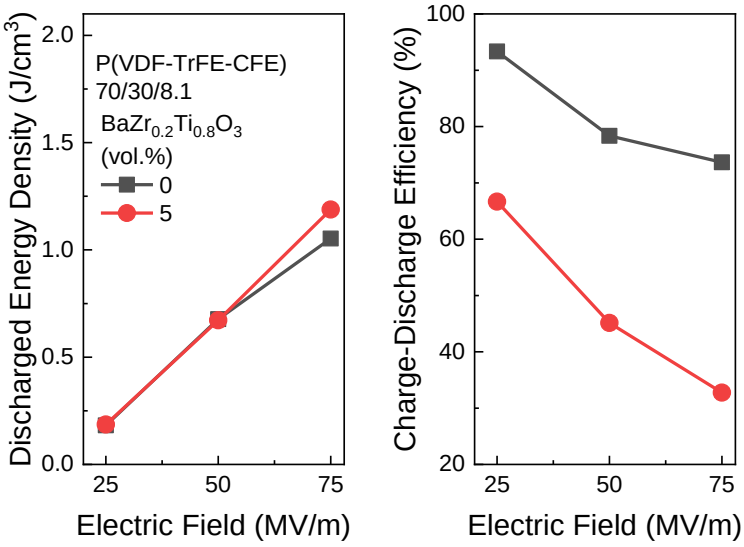

Figure 98 Discharge energy density and charge-discharge efficiency of P(VDF–TrFE–CFE) 70/30/8.1 and its nanocomposites estimated from the unipolar curves shown in Figure 97.

4.4.7 Conclusion

Zirconium doped barium titanate nanoparticles are produced via the hydrothermal route. The obtained secondary phase is detected as barium carbonate, and washed away with 5 vol.% acetic acid.

The free-standing nanocomposite films show a homogenous distribution of BZT nanoparticles in the terpolymer matrix as well as along the film thickness.

The results obtained through the direct electrocaloric measurements validate the previous results of the electrocaloric temperature coefficient in P(VDF-TrFE-CFE)/BZT nanocomposite free-standing films, under a moderate electric field and at room temperature.

The energy storage properties of P(VDF–TrFE–CFE) are improved by the addition of zirconium doped barium titanate nanoparticles. The discharge energy density values obtained in this work (2.5 J/cm^3) at merely 5 vol.% BZT loading has surpassed the ones reported in the literature where 17.5 vol.% barium titanate nanowires were used as nanofiller for P(VDF–TrFE–CFE) matrix. [143]

5 Summary & Outlook

5.1 Comparison of Ferroelectric & Relaxor Properties

The ferroelectric copolymer P(VDF-TrFE) 70/30 has been intensively studied, but its relaxor composition, namely P(VDF-TrFE-CFE) 70/30/8.1 has not been reported so far. The effect of incorporation of CFE monomer into the copolymer 70/30 composition on the structure and properties has not been discussed before.

To explain the difference between the ferroelectric and relaxor characteristics, an analysis of the ferroelectric copolymer P(VDF–TrFE) 70/30 and the relaxor terpolymer P(VDF–TrFE–CFE) 70/30/8.1 compositions is performed. The XRD analysis confirms that the P(VDF–TrFE) 70/30 crystallizes into the **β** phase, which is polar and ferroelectric. Moreover, the crystal structure of P(VDF–TrFE) 70/30 is changed from ferroelectric **β** to paraelectric **α** phase when 8.1 mol.% CFE is introduced into the copolymer. The change in the crystal structure and departure from ferroelectricity in P(VDF–TrFE–CFE) 70/30/8.1 happens due to the breakage of the long range ordering of the all-trans confirmation. From the DSC analysis, it is observed that the incorporation of the CFE monomer shifts the phase transition as well as the melting and recrystallization temperatures towards lower values.

The dielectric measurements show that P(VDF–TrFE) 70/30 has a sharp transition peak (at 378 K), which becomes broad and shifted towards room temperature with a frequency dispersion in P(VDF–TrFE–CFE) 70/30/8.1, confirming its relaxor behavior. From the polarization hysteresis measurements, it is shown that P(VDF–TrFE) 70/30 shows a high remnant polarization, which is another evidence for its ferroelectric behavior. Whereas, P(VDF–TrFE–CFE) 70/30/8.1 shows a slim hysteresis loop, indicating the relaxor character in the terpolymer, and undergoes a field induced phase transition. The electrostrictive strain in P(VDF–TrFE–CFE) 70/30/8.1 is almost twice that in the copolymer composition.

5.2 Effect of Composition on Polarization Hysteresis & Relaxor Properties of P(VDF-TrFE-CFE)

The relaxor characteristics of P(VDF-TrFE-CFE) have been known for a while. However, out of many possible compositions, only a few compositions have been analyzed so far. The study of the dielectric and ferroelectric properties of terpolymers in a broader concentration range is necessary to

comprehend the mechanism of the formation of the relaxor state, and the relationship between the properties and composition.

In order to develop a better understanding, six different compositions of P(VDF-TrFE-CFE) were examined in terms of their crystal structure, thermophysical, dielectric, polarization and electromechanical properties. Among them, the three compositions, 51.3/48.7/6.2, 59.8/40.2/7.3, and 70/30/8.1, are characterized for the first time. The dielectric measurements indicate a similar degree of relaxor behavior in the studied compositions. It is observed that with increasing CFE content, the freezing temperature is decreased, and the ergodic relaxor state is stabilized at room temperature. The freezing temperature of all compositions is far below room temperature, except for P(VDF-TrFE-CFE) 51.3/48.7/6.2, which has the lowest CFE content. The ergodic relaxor state at room temperature makes it possible to use the indirect method (Maxwell relation) for the electrocaloric measurement.

A higher magnitude of the applied electric field induces a transition into a ferroelectric state, at a critical electric field, which is revealed in the double hysteresis loops. The field induced phase transition is observed in five out of six studied compositions of P(VDF–TrFE–CFE). The presence of a double hysteresis loop due to the field induced phase transition deteriorates the electrical energy storage properties. The effect of the double hysteresis loop on the electrocaloric properties was to be analyzed.

5.3 Study of Electrocaloric Effect in P(VDF-TrFE-CFE)

Double hysteresis loops are observed in different P(VDF) based systems, but their effect on the electrocaloric effect has not been analyzed so far in literature. Many publications on the electrocaloric effect use the indirect method (Maxwell relations) to calculate the electrocaloric temperature and entropy changes. One issue that is encountered very often in literature is the presence of a specious “negative” electrocaloric effect in P(VDF) based systems, which is not observed through the direct measurements.

Aiming to explain the above-mentioned questions, direct and indirect electrocaloric measurements are performed. The direct electrocaloric measurements in different compositions of P(VDF-TrFE-CFE) (64.8/35.2/7.8, 59.8/40.2/7.3, 68/32/8.5) show that the electric field induced transition (exhibited

through the double hysteresis loop) results in an increase in the electrocaloric effect. Furthermore, the direct method only gives the positive values of the electrocaloric temperature change.

The polarization hysteresis measurements for the indirect method are performed with and without leakage current compensation in P(VDF-TrFE-CFE) 64.8/35.2/7.8. The polarization hysteresis loops measured without leakage current compensation give a “negative” electrocaloric effect. On the other hand, the indirect method gives comparable values to the direct measurement method, when the leakage current of the sample is compensated during the polarization hysteresis measurement. Hence, it is shown that the main reason behind the specious “negative” electrocaloric effect observed through the indirect measurement in P(VDF–TrFE–CFE) is the leakage current.

5.4 Study of P(VDF–TrFE–CFE)/BZT Nanocomposites

The existing reports on the electrical energy storage properties of P(VDF-TrFE-CFE) deal either with the neat terpolymer, or with their composites with conductive and 1 D nanofillers. The study of P(VDF-TrFE-CFE) composites with an inorganic 0 D nanofiller (nanoparticles) for electrical energy storage has not been discussed yet. Furthermore, the electrocaloric effect in P(VDF-TrFE-CFE) nanocomposites is studied by measuring the electrocaloric heat, and the electrocaloric effect is estimated. The direct measurement of the electrocaloric temperature change in P(VDF-TrFE-CFE) nanocomposites has not been reported so far.

In order to address these topics, terpolymer nanocomposites with zirconium doped barium titanate nanoparticles are studied. The hydrothermal route is adopted to produce zirconium doped barium titanate nanoparticles. The final product has a secondary phase, which is detected as barium carbonate and washed away with 5 vol.% acetic acid.

The electrocaloric temperature change in P(VDF-TrFE-CFE)/BZT nanocomposite free-standing films is directly measured under a moderate electric field at room temperature. The direct electrocaloric temperature change values measured in this work are in good agreement with the previous report, where the electrocaloric heat is measured, and the electrocaloric temperature change is calculated. Furthermore, the electrocaloric effect is improved in the terpolymer nanocomposite compared to the neat terpolymer.

The energy storage properties of P(VDF–TrFE–CFE) nanocomposites are evaluated by dielectric and polarization measurements. It is observed that the electrical energy storage properties (stored and

discharged energy densities) are improved by the addition of zirconium doped barium titanate nanoparticles. However, the charge-discharge efficiency of the nanocomposites drops down significantly due to the leakage current.

5.5 Outlook

The crystal structure analysis under an electric field would reveal more details of the phase formed due to the field induced transition. The mechanisms behind the single and double hysteresis loops can be investigated in detail. The data presented in this work and the existing data from the literature on different compositions of P(VDF-TrFE-CFE) can be used in the material designing and tailoring the terpolymer composition for the electrocaloric and energy storage applications.

The comparison of the direct and the indirect electrocaloric measurements in P(VDF-TrFE-CFE) 51.3/48.7/6.2 will be helpful to show the deviation between the direct measurement and the Maxwell relation in the non-ergodic relaxor state. Besides the electrocaloric effect, P(VDF-TrFE–CFE) can be studied for the elastocaloric effect owing to its flexibility. Both effects (electrocaloric and elastocaloric) can be coupled to achieve an enhanced temperature change. The new class of the dielectric elastomeric polymers would be interesting for caloric cooling. [165]

6 References

[1] H. Hu *et al.,* "Electrocaloric effect in relaxor ferroelectric polymer nanocomposites for solid-state cooling," J. Mater. Chem. A, vol. 8, no. 33, pp. 16814–16830, 2020.

[2] S. Fähler, "Caloric Effects in Ferroic Materials: New Concepts for Cooling," Energy Technol., vol. 6, no. 8, pp. 1394–1396, 2018.

[3] M. Valant, "Electrocaloric materials for future solid-state refrigeration technologies," Prog. Mater Sci. , vol. 57, no. 6, pp. 980–1009, 2012.

[4] A. Kumar *et al.,* "Prospects and challenges of the electrocaloric phenomenon in ferroelectric ceramics," J. Mater. Chem. C, vol. 7, no. 23, pp. 6836–6859, 2019.

[5] X. Moya, S. Kar-Narayan, and N. D. Mathur, "Caloric materials near ferroic phase transitions," Nat. Mater., vol. 13, no. 5, pp. 439–450, 2014.

[6] X. Moya and N. D. Mathur, "Caloric materials for cooling and heating," Science (New York, N.Y.), vol. 370, no. 6518, pp. 797–803, 2020.

[7] J. Shi *et al.,* "Electrocaloric Cooling Materials and Devices for Zero-Global-Warming-Potential, High-Efficiency Refrigeration," Joule, vol. 3, no. 5, pp. 1200–1225, 2019.

[8] C. Aprea *et al.,* "Electrocaloric refrigeration: An innovative, emerging, eco-friendly refrigeration technique," J. Phys.: Conf. Ser., vol. 796, p. 12019, 2017.

[9] M. Ismail, M. Yebiyo, and I. Chaer, "A Review of Recent Advances in Emerging Alternative Heating and Cooling Technologies," Energies, vol. 14, no. 2, p. 502, 2021.

[10] Q. Z. T. Correia, Ed., *Electrocaloric Materials New Generation of Coolers*, Springer, Heidelberg New York Dordrecht London, 2014.

[11] R. Pirc *et al.,* "Electrocaloric Effect and Dipolar Entropy Change in Ferroelectric Polymers," Ferroelectrics, vol. 426, no. 1, pp. 38–44, 2012.

[12] S. G. Lu *et al.,* "Enhanced electrocaloric effect in ferroelectric poly(vinylidene-fluoride/trifluoroethylene) 55/45 mol % copolymer at ferroelectric-paraelectric transition," Appl. Phys. Lett., vol. 98, no. 12, p. 122906, 2011.

[13] B. Neese *et al.,* "Large Electrocaloric Effect in Ferroelectric Polymers Near Room Temperature," Science, vol. 321, no. 5890, pp. 821–823, 2008.

[14] X. Li *et al.,* "Tunable temperature dependence of electrocaloric effect in ferroelectric relaxor poly(vinylidene fluoride-trifluoroethylene-chlorofluoroethylene terpolymer," Appl. Phys. Lett., vol. 99, no. 5, p. 52907, 2011.

[15] B. Rožič *et al.,* "Direct Measurements of the Giant Electrocaloric Effect in Soft and Solid Ferroelectric Materials," Ferroelectrics, vol. 405, no. 1, pp. 26–31, 2010.

[16] X. Li *et al.,* "Giant electrocaloric effect in ferroelectric poly(vinylidenefluoride-trifluoroethylene) copolymers near a first-order ferroelectric transition," Appl. Phys. Lett., vol. 101, no. 13, p. 132903, 2012.

[17] Z.-Y. Jiang *et al.,* "Exceptionally High Negative Electro-Caloric Effects of Poly(VDF$^-$co$^-$TrFE) Based Nanocomposites Tuned by the Geometries of Barium Titanate Nanofillers," Polymers, vol. 9, no. 12, p. 315, 2017.

[18] S. Ullah *et al.,* "The effects of additions of two-dimensional graphitic-C_3N_4 on the negative electro-caloric effects in P(VDF-TrFE) copolymers," RSC Adv., vol. 9, no. 28, pp. 15917–15925, 2019.

[19] A. Salea *et al.,* "The microstructure of negative electrocaloric Polyvinylidene fluoride-hexafluoropropylene copolymer on graphene loading for eco-friendly cooling technology," J. Cleaner Prod., vol. 251, p. 119730, 2020.
[20] X. Cheng *et al.,* "Indirect Electrocaloric Evaluation: Influence of Polarization Hysteresis Measurement Frequency," Phys. Status Solidi A, vol. 216, no. 24, p. 1900684, 2019.
[21] Y. Liu, J. F. Scott, and B. Dkhil, "Direct and indirect measurements on electrocaloric effect: Recent developments and perspectives," Appl. Phys. Rev., vol. 3, no. 3, p. 31102, 2016.
[22] X. Chen *et al.,* "Maxwell relation, giant (negative) electrocaloric effect, and polarization hysteresis," Appl. Phys. Lett., vol. 118, no. 12, p. 122904, 2021.
[23] G. H. Haertling, "Ferroelectric Ceramics: History and Technology," J. Am. Ceram. Soc., vol. 82, no.4, pp. 797–818, 1999.
[24] C. Bréchignac, P. Houdy, and M. Lahmani, *Nanomaterials and nanochemistry*, Springer, Berlin, Heidelberg, 2007.
[25] R. Dittmer *et al.,* "Ergodicity reflected in macroscopic and microscopic field-dependent behavior of BNT-based relaxors," J. Appl. Phys., vol. 115, no. 8, p. 84111, 2014.
[26] A. Pramanick and S. Nayak, "Perspective on emerging views on microscopic origin of relaxor behavior," J. Mater. Res., vol. 36, no. 5, pp. 1015–1036, 2021.
[27] D. Viehland *et al.,* "Freezing of the polarization fluctuations in lead magnesium niobate relaxors," J. Appl. Phys., vol. 68, no. 6, p. 2916, 1990.
[28] R. Pirc and R. Blinc, "Vogel-Fulcher freezing in relaxor ferroelectrics," Phys. Rev. B, vol. 76, no. 2, p. 241, 2007.
[29] Hari Singh Nalwa, Ed., *Ferroelectric Polymers,* CRC Press, Taylor & Francis Group, Boca Raton, Florida, 1995.
[30] Z. Zhang, M. H. Litt, and L. Zhu, "Achieving Relaxor Ferroelectric-like Behavior in Nylon Random Copolymers and Terpolymers," Macromolecules, vol. 50, no. 23, pp. 9360–9372, 2017.
[31] B. Stadlober, M. Zirkl, and M. Irimia-Vladu, "Route towards sustainable smart sensors: ferroelectric polyvinylidene fluoride-based materials and their integration in flexible electronics," Chem. Soc. Rev., vol. 48, no. 6, pp. 1787–1825, 2019.
[32] X. Chen, X. Han, and Q.-D. Shen, "PVDF-Based Ferroelectric Polymers in Modern Flexible Electronics," Adv. Electron. Mater., vol. 3, no. 5, p. 1600460, 2017.
[33] F. Bauer, H. Moulard, and G. Samara, "Advances in piezoelectric PVDF shock compression sensors," AIP Conf. Proc., vol. 429, no. 1, pp. 647–650, 1998.
[34] T. D. Binnie *et al.,* "An integrated 16/spl times/16 PVDF pyroelectric sensor array," IEEE Trans. Ultrason., Ferroelectr., Freq. Control, vol. 47, no. 6, pp. 1413–1420, 2000.
[35] V. F. Cardoso *et al.,* "Fluorinated Polymers as Smart Materials for Advanced Biomedical Applications," Polymers, vol. 10, no. 2, p. 161, 2018.
[36] Q. Li *et al.,* "Solution processable poly(vinylidene fluoride)-based ferroelectric polymers for flexible electronics," APL Mater., vol. 9, no. 1, p. 10902, 2021.
[37] P. Saxena and P. Shukla, "A comprehensive review on fundamental properties and applications of poly(vinylidene fluoride) (PVDF)," Adv. Compos. Hybrid Mater., vol. 4, no. 1, pp. 8–26, 2021.
[38] T. Furukawa, "Ferroelectric properties of vinylidene fluoride copolymers," Phase Transitions, vol. 18, 3-4, pp. 143–211, 1989.

[39] T. Furukawa, “Recent advances in ferroelectric polymers,” Ferroelectrics, vol. 104, no. 1, pp. 229–240, 1990.
[40] T. Soulestin *et al.,* “Vinylidene fluoride- and trifluoroethylene-containing fluorinated electroactive copolymers. How does chemistry impact properties?,” Prog. Polym. Sci., vol. 72, pp. 16–60, 2017.
[41] V. I. Sultanov *et al.,* “Microscopic Mechanism of the Large Electrocaloric Effect in Vinylidene Difluoride-Based Polymers,” Macromolecules, vol. 54, no. 8, pp. 3744–3754, 2021.
[42] A. J. Lovinger, “Ferroelectric Polymers,” Science, vol. 220, pp. 1115-1121, 1983.
[43] N. Spampinato *et al.,* “Enhancing the ferroelectric performance of P(VDF-co-TrFE) through modulation of crystallinity and polymorphism,” Polymer, vol. 149, pp. 66–72, 2018.
[44] P. Martins, A. C. Lopes, and S. Lanceros-Mendez, “Electroactive phases of poly(vinylidene fluoride): Determination, processing and applications,” Prog. Polym. Sci., vol. 39, no. 4, pp. 683–706, 2014.
[45] F. Oliveira *et al.,* “Process influences on the structure, piezoelectric, and gas-barrier properties of PVDF-TrFE copolymer,” J. Polym. Sci. Part B: Polym. Phys., vol. 52, no. 7, pp. 496–506, 2014.
[46] J. Seo, J. Y. Son, and W.-H. Kim, “Structural and ferroelectric properties of P(VDF-TrFE) thin films depending on the annealing temperature,” Mater. Lett., vol. 238, pp. 294–297, 2019.
[47] T. Nishiyama *et al.,* “Effect of solvents on the crystal formation of poly(vinylidene fluoride) film prepared by a spin-coating process,” Polym. J., vol. 49, no. 3, pp. 319–325, 2017.
[48] C. Teyssedre, A. Bernes, and C. Lacabanne, “Cooperative relaxations/transitions in ferroelectric polymers,” J. Therm. Anal., vol. 40, pp. 711–719, 1993.
[49] Prateek, V. K. Thakur, and R. K. Gupta, “Recent Progress on Ferroelectric Polymer-Based Nanocomposites for High Energy Density Capacitors: Synthesis, Dielectric Properties, and Future Aspects,” Chem. Rev., vol. 116, no. 7, pp. 4260–4317, 2016.
[50] Y. Huang *et al.,* “Can Relaxor Ferroelectric Behavior Be Realized for Poly(vinylidene fluoride- co -chlorotrifluoroethylene) [P(VDF–CTFE)] Random Copolymers by Inclusion of CTFE Units in PVDF Crystals?,” Macromolecules, vol. 51, no. 14, pp. 5460–5472, 2018.
[51] W. Xu *et al.,* “Composition Dependence of Microstructures and Ferroelectric Properties in Poly(vinylidene fluoride- ter -trifluoroethylene- ter -chlorodifluoroethylene) Terpolymers,” Macromolecules, vol. 53, no. 8, pp. 3139–3147, 2020.
[52] R. J. Klein *et al.,* “Influence of composition on relaxor ferroelectric and electromechanical properties of poly(vinylidene fluoride-trifluoroethylene- chlorofluoroethylene),” J. Appl. Phys., vol. 97, no. 9, p. 94105, 2005.
[53] Q. Li and Q. Wang, “Ferroelectric Polymers and Their Energy-Related Applications,” Macromol. Chem. Phys., vol. 217, no. 11, pp. 1228–1244, 2016.
[54] L. Yang *et al.,* “Novel polymer ferroelectric behavior via crystal isomorphism and the nanoconfinement effect,” Polymer, vol. 54, no. 7, pp. 1709–1728, 2013.
[55] M. R. Gadinski *et al.,* “Understanding of Relaxor Ferroelectric Behavior of Poly(vinylidene fluoride–trifluoroethylene–chlorotrifluoroethylene) Terpolymers,” Macromolecules, vol. 48, no. 8, pp. 2731–2739, 2015.
[56] A. Pramanick *et al.,* “Origin of dielectric relaxor behavior in PVDF-based copolymer and terpolymer films,” AIP Adv., vol. 8, no. 4, p. 45204, 2018.

[57] Y. Li *et al.,* "Stretching-Induced Relaxor Ferroelectric Behavior in a Poly(vinylidene fluoride- co -trifluoroethylene- co -hexafluoropropylene) Random Terpolymer," Macromolecules, vol. 50, no. 19, pp. 7646–7656, 2017.
[58] Q. Chen *et al.,* "Relaxor Ferroelectric Polymers–Fundamentals and Applications," Ferroelectrics, vol. 354, no. 1, pp. 178–191, 2007.
[59] X. Hu *et al.,* "High Energy Density Dielectrics Based on PVDF-Based Polymers," Energy Technol., vol. 6, no. 5, pp. 849–864, 2018.
[60] Y. Liu *et al.,* "Observation of a Negative Thermal Hysteresis in Relaxor Ferroelectric Polymers," Adv. Funct. Mater., vol. 30, no. 25, p. 2000648, 2020.
[61] J.-W. Wang *et al.,* "Microstructure and Dielectric Properties of P(VDF−TrFE−CFE) with Partially Grafted Copper Phthalocyanine Oligomer," Macromolecules, vol. 38, no. 6, pp. 2247–2252, 2005.
[62] J. Qian, J. Jiang, and Y. Shen, "Enhanced electrocaloric strength in P(VDF-TrFE-CFE) by decreasing the crystalline size," J. Materiomics, vol. 5, no. 3, pp. 357–362, 2019.
[63] X.-Z. Chen *et al.,* "Enhanced electrocaloric effect in poly(vinylidene fluoride-trifluoroethylene)-based terpolymer/copolymer blends," Appl. Phys. Lett., vol. 100, no. 22, p. 222902, 2012.
[64] J. Qian *et al.,* "Enhanced electrocaloric strength of P(VDF-TrFE-CFE) induced by edge-on lamellae," J. Mater. Chem. C, vol. 7, no. 11, pp. 3212–3217, 2019.
[65] L. Qi, L. Petersson, and T. Liu, "Review of Recent Activities on Dielectric Films for Capacitor Applications," J. Int. Counc. Electr. Eng., vol. 4, no. 1, pp. 1–6, 2014.
[66] A. Grünebohm *et al.,* "Origins of the Inverse Electrocaloric Effect," Energy Technol., vol. 6, no. 8, pp. 1491–1511, 2018.
[67] R. Pirc *et al.,* "Upper bounds on the electrocaloric effect in polar solids," Appl. Phys. Lett., vol. 98, no. 2, p. 021909, 2011.
[68] R. Pirc *et al.,* "Negative electrocaloric effect in antiferroelectric $PbZrO_3$," Europhys. Lett., vol. 107, no. 1, p. 17002, 2014.
[69] M. Marathe *et al.,* "Electrocaloric effect in BaTiO3 at all three ferroelectric transitions: Anisotropy and inverse caloric effects," Phys. Rev. B, vol. 96, no. 1, 2017.
[70] J. F. Scott, "Electrocaloric Materials," Annu. Rev. Mater. Res., vol. 41, no. 1, pp. 229–240, 2011.
[71] P. Blumenthal and A. Raatz, "Classification of electrocaloric cooling device types," Europhys. Lett., vol. 115, no. 1, p. 17004, 2016.
[72] M. Sanlialp *et al.,* "Modified Differential Scanning Calorimeter for Direct Electrocaloric Measurements," IEEE Trans. Ultrason., Ferroelectr., Freq. Control, vol. 63, no. 10, pp. 1690–1696, 2016.
[73] Y. Bai *et al.,* "The giant electrocaloric effect and high effective cooling power near room temperature for $BaTiO_3$ thick film," J. Appl. Phys., vol. 110, no. 9, p. 94103, 2011.
[74] Y. Bai, G.-P. Zheng, and S.-Q. Shi, "Kinetic electrocaloric effect and giant net cooling of lead-free ferroelectric refrigerants," J. Appl. Phys., vol. 108, no. 10, p. 104102, 2010.
[75] M. Sanlialp *et al.,* "Strong electrocaloric effect in lead-free $0.65Ba(Zr_{0.2}Ti_{0.8})O_3$ - $0.35(Ba_{0.7}Ca_{0.3})TiO_3$ ceramics obtained by direct measurements," Appl. Phys. Lett., vol. 106, no. 6, p. 62901, 2015.
[76] M. Sanlialp *et al.,* "Electrocaloric Effect in $Ba(Zr,Ti)O_3$ -$(Ba,Ca)TiO_3$ Ceramics Measured Directly," J. Am. Ceram. Soc., vol. 99, no. 12, pp. 4022–4030, 2016.

[77] M. Sanlialp *et al.,* "Direct electrocaloric measurements using a differential scanning calorimeter," 2015 Joint IEEE International Symposium on the Applications of Ferroelectric (ISAF), International Symposium on Integrated Functionalities (ISIF), and Piezoelectric Force Microscopy Workshop (PFM), 2015, pp. 159-162.
[78] M. Sanlialp *et al.,* "Direct measurement of electrocaloric effect in lead-free $Ba(Sn_xTi_{1-x})O_3$ ceramics," Appl. Phys. Lett., vol. 111, no. 17, p. 173903, 2017.
[79] Y. Chen *et al.,* "An All-Scale Hierarchical Architecture Induces Colossal Room-Temperature Electrocaloric Effect at Ultralow Electric Field in Polymer Nanocomposites," Adv. Mater., vol. 32, no. 30, 1907927, 2020.
[80] X. Chen *et al.,* "Towards electrocaloric heat pump—A relaxor ferroelectric polymer exhibiting large electrocaloric response at low electric field," Appl. Phys. Lett., vol. 113, no. 11, p. 113902, 2018.
[81] A. Kholkin, A. A. Semenov, and O. V. Pakhomov, *The Electrocaloric Effect: Materials and Applications*, William Andrew Publishing, 2023.
[82] M. Sanlialp, "Elektrokalorischer Effekt in bleifreien Relaxorkeramiken," Dissertation, Universität Duisburg-Essen, Germany, 2017. (online) nbn-resolving.org/urn:nbn:de:hbz:464-20171027-124048-5
[83] M. Sanlialp *et al.,* "Quasi-adiabatic calorimeter for direct electrocaloric measurements," Rev. Sci. Instrum., vol. 89, no. 3, p. 34903, 2018.
[84] E. Bsaibess *et al.,* "Investigation of the electrocaloric effect in $BaTiO_3$ multilayers by pASC calorimetry," J. Therm. Anal. Calorim., 2021.
[85] D. Guo *et al.,* "Electrocaloric characterization of a poly(vinylidene fluoride-trifluoroethylene-chlorofluoroethylene) terpolymer by infrared imaging," Appl. Phys. Lett., vol. 105, no. 3, p. 31906, 2014.
[86] G. Sebald *et al.,* "Differential scanning calorimeter and infrared imaging for electrocaloric characterization of poly(vinylidene fluoride-trifluoroethylene-chlorofluoroethylene) terpolymer," Appl. Phys. Lett., vol. 101, no. 2, p. 22907, 2012.
[87] G. Y. Sotnikova *et al.,* "Mid-infrared radiation technique for direct pyroelectric and electrocaloric measurements," Rev. Sci. Instrum., vol. 91, no. 1, p. 15119, 2020.
[88] T. Tong *et al.,* "Reduction of the electrocaloric entropy change of ferroelectric PbZr1−xTixO3 epitaxial layers due to an elastocaloric effect," Phys. Rev. B, vol. 90, no. 9, p. 094116, 2014.
[89] F. Le Goupil *et al.,* "Direct and indirect electrocaloric measurements on 〈001〉-$PbMg_{1/3}Nb_{2/3}O_3$ - $30PbTiO_3$ single crystals," J. Appl. Phys., vol. 111, no. 12, p. 124109, 2012.
[90] E. Birks *et al.,* "Direct and indirect determination of electrocaloric effect in $Na_{0.5}Bi_{0.5}TiO_3$," J. Appl. Phys., vol. 121, no. 22, p. 224102, 2017.
[91] R. Pirc *et al.,* "Electrocaloric effect in relaxor ferroelectrics," J. Appl. Phys., vol. 110, no. 7, p. 74113, 2011.
[92] S. Merselmiz *et al.,* "High energy storage efficiency and large electrocaloric effect in lead-free $BaTi_{0.89}Sn_{0.11}O_3$ ceramic," Ceram. Int., vol. 46, no. 15, pp. 23867–23876, 2020.
[93] N. Novak, Z. Kutnjak, and R. Pirc, "High-resolution electrocaloric and heat capacity measurements in barium titanate," Europhys. Lett., vol. 103, no. 4, p. 47001, 2013.
[94] N. Novak, R. Pirc, and Z. Kutnjak, "Impact of critical point on piezoelectric and electrocaloric response in barium titanate," Phys. Rev. B, vol. 87, no. 10, p. 1040, 2013.

[95] A. Kukreti, A. Kumar, and U. C. Naithani, "Electric field dependence of specific heat in $Ba_xSr_{1-x}TiO_3$ ferroelectric perovskites," Indian J. Pure Appl. Phys., vol. 47, pp. 43–48, 2009.
[96] M. Marathe *et al.,* "First-principles-based calculation of the electrocaloric effect in $BaTiO_3$: A comparison of direct and indirect methods," Phys. Rev. B, vol. 93, no. 5, p. 054110, 2016.
[97] C. Molin *et al.,* "Comparison of direct electrocaloric characterization methods exemplified by 0.92 $Pb(Mg_{1/3}Nb_{2/3})O_3$ - 0.08 $PbTiO_3$ multilayer ceramics," J. Am. Ceram. Soc., vol. 100, no. 7, pp. 2885–2892, 2017.
[98] S. G. Lu *et al.,* "Organic and inorganic relaxor ferroelectrics with giant electrocaloric effect," Appl. Phys. Lett., vol. 97, no. 16, p. 162904, 2010.
[99] Z. Jiang *et al.,* "Electrocaloric effects in the lead-free $Ba(Zr,Ti)O_3$ relaxor ferroelectric from atomistic simulations," Phys. Rev. B, vol. 96, no. 1, p. 645, 2017.
[100] A. S. Starkov, O. V. Pakhomov, and I. A. Starkov, "Taking into account conductivity in describing the electrocaloric effect in ferroelectrics," Ferroelectrics, vol. 539, no. 1, pp. 141–145, 2019.
[101] S. Lu *et al.,* "Joule heating - A significant factor in electrocaloric effect," Ceram. Int., vol. 45, no. 14, pp. 16992–16998, 2019.
[102] D. Shan *et al.,* "High fidelity direct measurement of local electrocaloric effect by scanning thermal microscopy," Nano Energy, vol. 67, p. 104203, 2020.
[103] M. Quintero *et al.,* "Decoupling electrocaloric effect from Joule heating in a solid state cooling device," Appl. Phys. Lett., vol. 99, no. 23, p. 232908, 2011.
[104] U. Plaznik *et al.,* "Erratum: Electrocaloric cooling: The importance of electric-energy recovery and heat regeneration," Europhys. Lett., vol. 112, no. 1, p. 19901, 2015.
[105] M. Marathe and C. Ederer, "Electrocaloric effect in $BaTiO_3$: A first-principles-based study on the effect of misfit strain," Appl. Phys. Lett., vol. 104, no. 21, p. 212902, 2014.
[106] X. Moya *et al.,* "Giant electrocaloric strength in single-crystal $BaTiO_3$," Adv. Mater., vol. 25, no. 9, pp. 1360–1365, 2013.
[107] Y. Liu, J. F. Scott, and B. Dkhil, "Some strategies for improving caloric responses with ferroelectrics," APL Mater., vol. 4, no. 6, p. 64109, 2016.
[108] S.-G. Lu and Q. Zhang, "Electrocaloric Materials for Solid-State Refrigeration," Adv. Mater., vol. 21, no. 19, pp. 1983–1987, 2009.
[109] X. Li *et al.,* "Pyroelectric and electrocaloric materials," J. Mater. Chem. C, vol. 1, no. 1, pp. 23–37, 2013.
[110] Y. Liu *et al.,* "High cyclic stability of electrocaloric effect in relaxor poly(vinylidene fluoride-trifluoroethylene-chlorofluoroethylene) terpolymers in the absence of ferroelectric phase transition," J. Appl. Phys., vol. 126, no. 23, p. 234102, 2019.
[111] P. F. Liu *et al.,* "Huge electrocaloric effect in Langmuir–Blodgett ferroelectric polymer thin films," New J. Phys., vol. 12, no. 2, p. 23035, 2010.
[112] G. Shanshan, M. Escobar Castillo, V.V. Shvartsman, M. Karabasov and D.C. Lupascu, "Electrocaloric effect in P(VDF-TrFE)/ barium zirconium titanate composites," 2019 IEEE International Symposium on Applications of Ferroelectrics (ISAF), 2019, pp. 1-3.
[113] Y. Matsushita *et al.,* "Investigation of the electrocaloric effect in ferroelectric polymer film through direct measurement under alternating electric field," Appl. Phys. Express, vol. 13, no. 4, p. 41007, 2020.

[114] S. G. Lu *et al.,* "Electrocaloric effect in ferroelectric polymers," Appl. Phys. A, vol. 107, no. 3, pp. 559–566, 2012.
[115] S. G. Lu *et al.,* "Comparison of directly and indirectly measured electrocaloric effect in relaxor ferroelectric polymers," Appl. Phys. Lett., vol. 97, no. 20, p. 202901, 2010.
[116] B. Neese *et al.,* "Electrocaloric effect of the relaxor ferroelectric poly(vinylidene fluoride-trifluoroethylene-chlorofluoroethylene) terpolymer," Appl. Phys. Lett., vol. 94, no. 4, p. 42910, 2009.
[117] Q. Li *et al.,* "Relaxor ferroelectric-based electrocaloric polymer nanocomposites with a broad operating temperature range and high cooling energy," Adv. Mater., vol. 27, no. 13, pp. 2236–2241, 2015.
[118] G. Zhang *et al.,* "Ferroelectric polymer nanocomposites for room-temperature electrocaloric refrigeration," Adv. Mater., vol. 27, no. 8, pp. 1450–1454, 2015.
[119] X.-Z. Chen *et al.,* "A nanocomposite approach to tailor electrocaloric effect in ferroelectric polymer," Polymer, vol. 54, no. 20, pp. 5299–5302, 2013.
[120] G. Zhang *et al.,* "Colossal Room-Temperature Electrocaloric Effect in Ferroelectric Polymer Nanocomposites Using Nanostructured Barium Strontium Titanates," ACS Nano, vol. 9, no. 7, pp. 7164–7174, 2015.
[121] B. Lu *et al.,* "Enhancing the electrocaloric effect in a relaxor polymer by including minor normal ferroelectric phase," Appl. Phys. Lett., vol. 113, no. 15, p. 153903, 2018.
[122] H. Aziguli *et al.,* "Enhanced electrocaloric effect in lead-free organic and inorganic relaxor ferroelectric composites near room temperature," Appl. Phys. Lett., vol. 112, no. 19, p. 193902, 2018.
[123] H. Aziguli *et al.,* "Tuning the electrocaloric reversibility in ferroelectric copolymers by a blend approach," Europhys. Lett., vol. 125, no. 5, p. 57001, 2019.
[124] Y.-C. Lu *et al.,* "Enhanced electrocaloric effect for refrigeration in lead-free polymer composite films with an optimal filler loading," Appl. Phys. Lett., vol. 114, no. 23, p. 233901, 2019.
[125] B. Rožič *et al.,* "Electrocaloric effect in the relaxor ferroelectric polymer composition P(VDF–TrFE–CFE) 0.90 –P(VDF–CTFE) 0.10," Phase Transitions, vol. 83, 10-11, pp. 819–823, 2010.
[126] X.-Z. Chen *et al.,* "A polymer blend approach to tailor the ferroelectric responses in P(VDF–TrFE) based copolymers," Polymer, vol. 54, no. 9, pp. 2373–2381, 2013.
[127] F. Le Goupil et al., "Electrocaloric Enhancement Induced by Cocrystallization of Vinylidene Difluoride-Based Polymer Blends," ACS Macro Lett., pp. 1555–1562, 2021..
[128] X. Qian *et al.,* "Internal Biasing in Relaxor Ferroelectric Polymer to Enhance the Electrocaloric Effect," Adv. Funct. Mater., vol. 25, no. 32, pp. 5134–5139, 2015.
[129] D. Q. Tan, "Review of Polymer-Based Nanodielectric Exploration and Film Scale-Up for Advanced Capacitors," Adv. Funct. Mater., vol. 30, no. 18, p. 1808567, 2020.
[130] H. Huang and J. F. Scott, *Ferroelectric materials for energy applications*, Weinheim, Wiley-VCH, 2018.
[131] M. Peddigari *et al.,* "Linear and Nonlinear Dielectric Ceramics for High-Power Energy Storage Capacitor Applications," J. Korean Ceram. Soc., vol. 56, no. 1, pp. 1–23, 2019.

[132] M. Streibl, R. Karmazin, and R. Moos, “Materials and applications of polymer films for power capacitors with special respect to nanocomposites,” IEEE Trans. Dielectr. Electr. Insul., vol. 25, no. 6, pp. 2429–2442, 2018.
[133] S. Nasreen *et al., Eds., Kirk-Othmer Encyclopedia of Chemical Technology.* Polymer Dielectrics for Capacitor Application.
[134] X. Hao, “A review on the dielectric materials for high energy-storage application,” J. Adv. Dielect., vol. 03, no. 01, p. 1330001, 2013.
[135] J. Luo *et al.,* “Research Progress of All Organic Polymer Dielectrics for Energy Storage from the Classification of Organic Structures,” Macromol. Chem. Phys., vol. 222, no. 11, p. 2100049, 2021.
[136] Y. Liu *et al.,* “Relaxor Ferroelectric Polymers: Insight into High Electrical Energy Storage Properties from a Molecular Perspective,” Small Sci., vol. 1, no. 3, p. 2000061, 2021.
[137] W. Xia and Z. Zhang, “PVDF-based dielectric polymers and their applications in electronic materials,” IET Nanodielectr., vol. 1, no. 1, pp. 17–31, 2018.
[138] O. L. Smith *et al.,* “Enhanced permittivity and energy density in neat poly(vinylidene fluoride-trifluoroethylene-chlorotrifluoroethylene) terpolymer films through control of morphology,” ACS Appl. Mater. Interfaces, vol. 6, no. 12, pp. 9584–9589, 2014.
[139] S. Zhang *et al.,* “Microstructure and Electromechanical Properties of Carbon Nanotube/ Poly(vinylidene fluoride—trifluoroethylene—chlorofluoroethylene) Composites,” Adv. Mater., vol. 17, no. 15, pp. 1897–1901, 2005.
[140] X. Yin, J.-F. Capsal, and D. Guyomar, “A comprehensive investigation of poly(vinylidene fluoride-trifluoroethylene-chlorofluoroethylene) terpolymer nanocomposites with carbon black for electrostrictive applications,” Appl. Phys. Lett., vol. 104, no. 5, p. 52913, 2014.
[141] M. N. Almadhoun *et al.,* “Influence of Stacking Morphology and Edge Nitrogen Doping on the Dielectric Performance of Graphene–Polymer Nanocomposites,” Chem. Mater., vol. 26, no. 9, pp. 2856–2861, 2014.
[142] A. Javadi *et al.,* “Chemically modified graphene/P(VDF-TrFE-CFE) electroactive polymer nanocomposites with superior electromechanical performance,” J. Mater. Chem., vol. 22, no. 3, pp. 830–834, 2012.
[143] H. Tang, Y. Lin, and H. A. Sodano, “Ultra high energy density nanocomposite capacitors using surface-functionalized BaTiO 3 nanowires and PVDF-TrFE-CFE,” Proc. SPIE 8342, Behavior and Mechanics of Multifunctional Materials and Composites 2012, p. 834206, 2012.
[144] S. Zhang *et al.,* “Microstructure and Electromechanical Properties of Carbon Nanotube/ Poly(vinylidene fluoride—trifluoroethylene—chlorofluoroethylene) Composites,” Adv. Mater., vol. 17, no. 15, pp. 1897–1901, 2005.
[145] X. Xiong *et al.,* “Facile preparation and enhanced dielectric performance of rod-like TiO2/P(VDF-TrFE-CFE) composites,” J. Mater. Sci.: Mater. Electron., vol. 29, no. 16, pp. 14161–14169, 2018.
[146] M.-X. Zhu *et al.,* “Rational Design of High-Energy-Density Polymer Composites by Machine Learning Approach,” ACS Appl. Energy Mater., vol. 4, no. 2, pp. 1449–1458, 2021.
[147] Y. Zhang *et al.,* “Energy Storage and Electrocaloric Cooling Performance of Advanced Dielectrics,” Molecules, vol. 26, no. 2, 2021.

[148] Y. Jiang *et al.,* "Ferroelectric polymers and their nanocomposites for dielectric energy storage applications," APL Mater., vol. 9, no. 2, p. 20905, 2021.
[149] X. Zhou *et al.,* "Polyvinylidene Fluoride based polymeric dielectrics for high energy density capacitor application," 2009 IEEE 9th International Conference on the Properties and Applications of Dielectric Materials, 2009, pp. 15–19, 2009.
[150] B. Chu *et al.,* "A Dielectric Polymer with High Electric Energy Density and Fast Discharge Speed," Science, vol. 313, no. 5785, pp. 332–334, 2006.
[151] Y. Hambal *et al.,* "Effect of Composition on Polarization Hysteresis and Energy Storage Ability of P(VDF-TrFE-CFE) Relaxor Terpolymers," Polymers, vol. 13, no. 8, p. 1343, 2021.
[152] C. Chen *et al.,* "Designing of Ferroelectric/Linear Dielectric Bilayer Films: An Effective Way to Improve the Energy Storage Performances of Polymer-Based Capacitors," J. Phys. Chem. C, vol. 124, no. 11, pp. 5920–5927, 2020.
[153] Y. Hambal *et al.,* "Directly Measured Electrocaloric Effect in Relaxor Polymer Nanocomposites," 2021 IEEE International Symposium on Applications of Ferroelectrics (ISAF), 2021, pp. 1-4.
[154] C. Baek *et al.,* "Facile hydrothermal synthesis of $BaZr_xTi_{1-x}O_3$ nanoparticles and their application to a lead-free nanocomposite generator," RSC Adv., vol. 7, no. 5, pp. 2851–2856, 2017.
[155] *Manual aixPlorer TFA3000-FE*. Manual.
[156] R. Meyer *et al.,* "Dynamic leakage current compensation in ferroelectric thin-film capacitor structures," Appl. Phys. Lett., vol. 86, no. 14, p. 142907, 2005.
[157] R. Pirc *et al.,* "Spherical model of relaxor polymers," Phys. Rev. B, vol. 72, no. 1, p. 241, 2005.
[158] H.-M. Bao *et al.,* "Phase Transitions and Ferroelectric Relaxor Behavior in P(VDF−TrFE−CFE) Terpolymers," Macromolecules, vol. 40, no. 7, pp. 2371–2379, 2007.
[159] C. Teyssedre, A. Bernes, and C. Lacabanne, "Cooperative movements associated with the Curie transition in P(VDF-TrFE) copolymers," J. Polym. Sci. B: Polym. Phys., vol. 33, pp. 879–890, 1995.
[160] T. R. Venkatesan *et al.,* "Relaxation processes and structural transitions in Poly(vinylidene fluoride-trifluoroethylene-chlorofluoroethylene) relaxor-ferroelectric terpolymers as seen in dielectric spectroscopy," IEEE Trans. Dielectr. Electr. Insul., vol. 25, no. 6, pp. 2229–2235, 2018.
[161] A. A. Bokov and Z.-G. Ye, "Recent progress in relaxor ferroelectrics with perovskite structure," J. Mater. Sci., vol. 41, no. 1, pp. 31–52, 2006.
[162] K. Uchino and S. Nomura, "Critical exponents of the dielectric constants in diffused-phase-transition crystals," Ferroelectrics, vol. 44, no. 1, pp. 55–61, 1982.
[163] I. A. Santos and J. A. Eiras, "Phenomenological description of the diffuse phase transition in ferroelectrics," J. Phys.: Condens. Matter, vol. 13, no. 50, pp. 11733–11740, 2001.
[164] J.-Y. Kim, S. H. Park, and S. Yu, "Effect of chlorine-containing polymer additive on dielectric performance of polymer dielectric films," Electron. Lett., vol. 50, no. 5, pp. 357–358, 2014.
[165] Y. Sheima *et al.,* "Polysiloxanes Modified with Different Types and Contents of Polar Groups: Synthesis, Structure, and Thermal and Dielectric Properties," Macromolecules, vol. 54, no. 12, pp. 5737–5749, 2021.
[166] L. Zhu, "Exploring Strategies for High Dielectric Constant and Low Loss Polymer Dielectrics," J. Phys. Chem. Lett., vol. 5, no. 21, pp. 3677–3687, 2014.

[167] X. L. Zhao *et al.,* "Enhanced piezoelectric response in the artificial ferroelectric polymer multilayers," Appl. Phys. Lett., vol. 105, no. 22, p. 222907, 2014.
[168] S. Zhang *et al.,* "Direct spectroscopic evidence of field-induced solid-state chain conformation transformation in a ferroelectric relaxor polymer," J. Appl. Phys., vol. 99, no. 4, p. 44107, 2006.
[169] V. Bobnar *et al.,* "Relaxor freezing and electric-¯eld{induced ferroelectric transition in a lanthanum lead zirconate titanate ceramics," Phys. Rev. B, vol. 60, no. 9, pp. 326–331, 1999.
[170] E. Sapper *et al.,* "Electric-field–temperature phase diagram of the ferroelectric relaxor system $(1 - x)Bi_{1/2}Na_{1/2}TiO_3 - xBaTiO_3$ doped with manganese," J. Appl. Phys., vol. 115, no. 19, p. 194104, 2014.
[171] X. Ren, "Large electric-field-induced strain in ferroelectric crystals by point-defect-mediated reversible domain switching," Nat. Mater., vol. 3, no. 2, pp. 91–94, 2004.
[172] J. F. Scott, "Ferroelectrics go bananas," J. Phys.: Condens. Matter, vol. 20, no. 2, p. 21001, 2008.
[173] X. Chen *et al.,* "P(VDF-TrFE-CFE) terpolymer thin-film for high performance nonvolatile memory," Appl. Phys. Lett., vol. 102, no. 6, p. 63103, 2013.
[174] A. Bradeško *et al.,* "Self-heating of relaxor and ferroelectric ceramics during electrocaloric field cycling," APL Mater., vol. 7, no. 7, p. 71111, 2019.
[175] T. Badapanda *et al.,* "Electric field induced strain, switching and energy storage behaviour of lead free Barium Zirconium Titanate ceramic," Physica B, vol. 521, pp. 264–269, 2017.
[176] Hernandes et al, "$BaTi_{1-x}Zr_xO_3$ nanopowders prepared by the modified Pechini method," J. Therm. Anal. Calorim., vol. 87, no. 3, pp. 725–730, 2007.
[177] A. Ianculescu *et al.,* "Properties of $Ba_{1-x}Sr_xTiO_3$ Ceramics Prepared by the Modified-Pechini Method," Ferroelectrics, vol. 369, no. 1, pp. 22–34, 2010.
[178] S. Halder *et al.,* "Fabrication and electrical characterisation of Zr-substituted BaTiO3 thin films," Appl. Phys. A, vol. 81, no. 1, pp. 25–29, 2005.
[179] V. V. Shvartsman and D. C. Lupascu, "Lead-Free Relaxor Ferroelectrics," J. Am. Ceram. Soc., vol. 95, no. 1, pp. 1–26, 2012.
[180] M. Acosta *et al.,* "$BaTiO_3$ -based piezoelectrics: Fundamentals, current status, and perspectives," Appl. Phys. Rev., vol. 4, no. 4, p. 41305, 2017.
[181] J. Peng *et al.,* "A thermodynamic potential for barium zirconate titanate solid solutions," npj Comput. Mater., vol. 4, no. 1, p. 349, 2018.
[182] P. S. Dobal *et al.,* "Micro-Raman scattering and dielectric investigations of phase transition behavior in the $BaTiO_3$–$BaZrO_3$ system," J. Appl. Phys., vol. 89, no. 12, pp. 8085–8091, 2001.
[183] P. S. Dobal and R. S. Katiyar, "Studies on ferroelectric perovskites and Bi-layered compounds using micro-Raman spectroscopy," J. Raman Spectrosc., vol. 33, no. 6, pp. 405–423, 2002.
[184] V. V. Shvartsman, J. Zhai, and W. Kleemann, "The Dielectric Relaxation in Solid Solutions $BaTi_{1-x}Zr_xO_3$," Ferroelectrics, vol. 379, no. 1, pp. 77–85, 2009.
[185] J. Qian *et al.,* "Interfacial Coupling Boosts Giant Electrocaloric Effects in Relaxor Polymer Nanocomposites: In Situ Characterization and Phase-Field Simulation," Adv. Mater., vol. 31, no. 5, 1801949, 2019.
[186] Y. Jiang *et al.,* "Ferroelectric polymers and their nanocomposites for dielectric energy storage applications," APL Mater., vol. 9, no. 2, p. 20905, 2021.

[187] Y. Hambal *et al.,* "High Energy Storage Density in Nanocomposites of P(VDF-TrFE-CFE) Terpolymer and $BaZr_{0.2}Ti_{0.8}O_3$ Nanoparticles," Materials, vol. 15, no. 9, p. 3151, 2022.

List of Figures

List of Tables

Declaration

Hereby, I, Yusra Hambal, born on June 16th, 1991 in Karachi (Pakistan), declare that this work is originally performed by me, and all the resources used within this work are duly referred and acknowledged.

Haag in Oberbayern, October 7th, 2022

_____

Yusra Hambal